UNIVERSITY OF CALIFORNIA
RIVERSIDE

Nanoengineering of ZnO Electrical and Optical Characteristics by Controlling Its Morphology and Defects via Reaction Kinetics, Fluid Dynamics, and Stoichiometry in Low-Pressure CVD Synthesis

A Dissertation submitted in partial satisfaction
of the requirements for the degree of

Doctor of Philosophy

in

Materials Science and Engineering

by

Taehoon Lim

December 2016

Dissertation Committee:
Dr. Alfredo A. Martinez-Morales, Co-Chairperson
Dr. Lorenzo Mangolini, Co-Chairperson
Dr. Krassimir N. Bozhilov

The Dissertation of Taehoon Lim is approved:

_____

_____

Committee Co-Chairperson

_____

Committee Co-Chairperson

University of California, Riverside

Acknowledgement

Firstly, I would like to express my most sincere gratitude towards my advisor Dr. Alfredo A. Martinez-Morales for his continuous support towards my Ph.D study and research; especially for his patience, guidance, and motivation. With his support I was able to complete this dissertation.

In addition to my advisor, I would like to show my gratitude towards my dissertation committee members: Dr. Lorenzo Mangolini and Dr. Krassimir N. Bozhilov. Their well thought out comments and guided questions were immensely appreciated.

I would like to show my gratitude for Dr. Jianlin Liu and Dr. Valentine Vullev for allowing me the use of their lab equipment. Without access to these instruments, conducting research would be near impossible. I want to thank my lab mates Ian Miller, Darren Kwee, Rany Tith, Kichang Jung, and Eric Pichinte for their support and providing me with memories that I can cherish forever.

The SEM characterization was conducted at the Central Facility for Advanced Microscopy and Microanalysis (CFAMM). This research was partially funded by the American Public Power Association (APPA) Demonstration of Energy & Efficiency Developments (DEED) Program, the Riverside Public Utilities (RPU) Energy Innovations Grant Program, the UC MEXUS-CONACYT Program, and the University of California Advanced Solar Technologies Institute (UC Solar).

This dissertation is dedicated to my family.

ABSTRACT OF THE DISSERTATION

Nanoengineering of ZnO Electrical and Optical Characteristics by Controlling Its Morphology and Defects via Reaction Kinetics, Fluid Dynamics, and Stoichiometry in Low-Pressure CVD Synthesis

by

Taehoon Lim

Doctor of Philosophy, Graduate Program in Materials Science and Engineering
University of California, Riverside, December 2016
Dr. Alfredo A. Martinez-Morales, Co-Chairperson
Dr. Lorenzo Mangolini, Co-Chairperson

LPCVD synthesis and characterization of ZnO with diverse morphology for semiconducting applications are studied and discussed in this dissertation. Because nanoscale ZnO shows variant characteristics depending on its physical dimensions, morphology, and impurity concentration, the focus of this work is to control the structure and composition of ZnO by adjusting synthesis parameters and methods. In Chapter 2, the synthesis of ZnO with optimized concentration of oxygen vacancies and physical dimensions are discussed. Opaqueness of ZnO is derived from scattering due to its physical dimensions, but visible transparency for the photocatalytic application of ZnO for solar cell devices is required. By controlling the concentration of oxygen vacancies and physical dimensions, fluorescent and transparent ZnO is successfully synthesized. In Chapter 3, a

method to stabilize precursor supply and to lower the reaction temperature is discussed. In CVD synthesis, the stable and continuous growth of ZnO is inhibited by the premature oxidation of Zn, and the formation of a zinc oxide layer that blocks the evaporation of Zn precursor. By controlling the fluid dynamics of precursor vapors, a low temperature synthesis method with higher product uniformity is developed. Using this method, a stable synthesis technique for producing high quality ZnO under low temperature is successfully achieved. In Chapter 4, the synthesis of ZnO under relatively low temperature is discussed. During LPCVD synthesis it is observed that as the distance from the source increases, the partial vapor pressure of Zn near the surface of the deposition substrate is drastically decreased (along the axis of gas flow), forming a dimensional gradient on a single substrate. The changing reactant ratio near the surface drives the non-uniformity of product in terms of morphology, physical dimensions, and impurity concentration. In Chapter 5, a novel template-free self-catalyzed synthesis technique for achieving ultra-thin ZnO nanowires is discussed. From the tip of synthesized hexagonal cone ZnO, ultra-thin ZnO nanowires are grown by self-catalysis.

Table of Contents

List of Figures

List of Tables

Chapter 1.

Introduction

1.1. Characteristics of ZnO

Zinc oxide (ZnO) is environmentally harmless and a stable material, which is used in a wide-variety of applications such as in building materials [1], medicine [2], accoustic filters [3], and pigments [4]. ZnO is a II-VI semiconducting material with wide bandgap (3.3 eV) and large exciton binding energy (60 meV) [5]. It is widely used for optical applications such as photoelectric devices [6], light emitting devices [7], photoelectrodes [8], and photocatalysts [9], as well as in electrical applications such as transistors [10], and sensors [11]. Additionally, because ZnO has physical characteristics that are antibacterial [12], deodorizing [13], and light scattering [14], it is widely used for cosmetics [15]. The crystal structure of ZnO is found as cubic zinc blende, hexagonal wurtzite, and rocksalt as illustrated in Figure 1.1 [16].

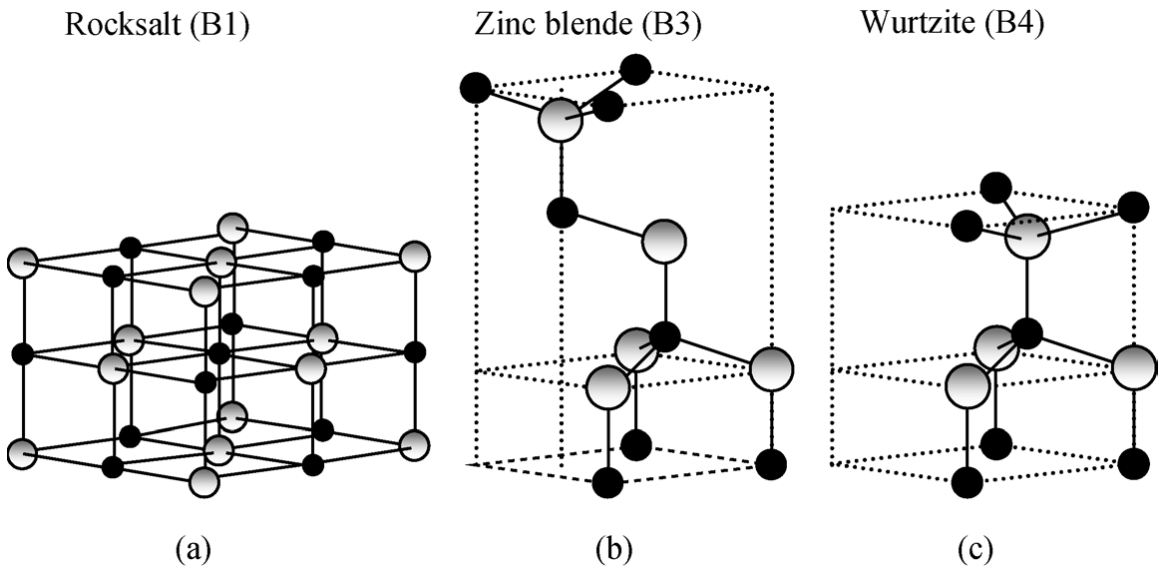

Figure 1.1. Stick-and-ball representation of ZnO crystal structures

Among the possible crystal structures of ZnO, wurtzite is the most stable and widely used. Particularly zinc blende requires epitaxial growth on a cubic substrate, and rocksalt is only stable under high pressure environments (higher than 10 GPa [17]).

Wurtzite ZnO is stable in ambient conditions and its innate physical and optoelectrical characteristics (due to its crystal structure) makes it attractive for applications on micro devices. Hexagonal wurtzite belongs to 6mm or C_{6v} point group and the space group of $P6_3mc$ in the Hermann-Mauguin notation, and its lattice parameters are a=0.325 nm, c=0.520 nm [18]. ZnO shows piezoelectric characteristics due to the lack of inversion symmetry and the dislocation of oxygen layer in the lattice along c-axis, as shown in Figure 1.2 [16]. Moreover, ZnO has good heat-resisting properties due to its high melting point and low thermal expansion coefficient, as well as a high heat conductivity and heat capacity, making it useful for pyroelectric devices. This dissertation is focused on wurtzite ZnO due to the characteristics and stability discussed above.

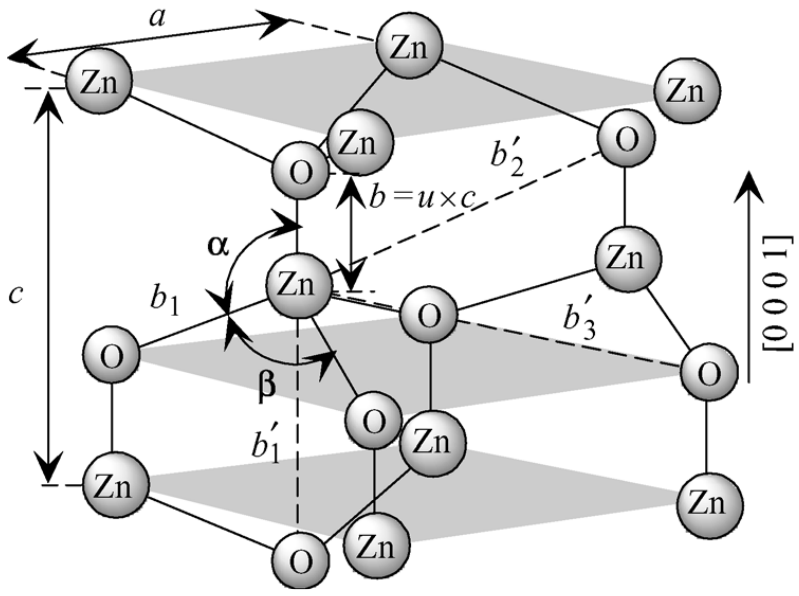

Figure 1.2. Schematic representation of wurtzite ZnO

Most ZnO naturally shows n-type semiconducting characteristics, and its electron mobility is relatively higher than hole mobility [19]. The origin of this unintentional, naturally occurring n-type characteristics, has been extensively investigated in the literature. Nonstoichiometric crystal formation, native point defects, and impurities such as hydrogen are suggested as the possible reasons, but it is not clearly identified yet [20]. Point defects are made intrinsically by donor states such as oxygen vacancy (V_o), zinc interstitial (Zn_i) and anti-site zinc (Zn_o), and by acceptor states such as zinc vacancy (V_{Zn}), oxygen interstitial (O_i) and anti-site oxygen (O_{Zn}). The electron conductivity and n-type characteristics are driven by the donor states among the aforementioned point defects. The energy level of each point defect are shown in Figure 1.3 [21].

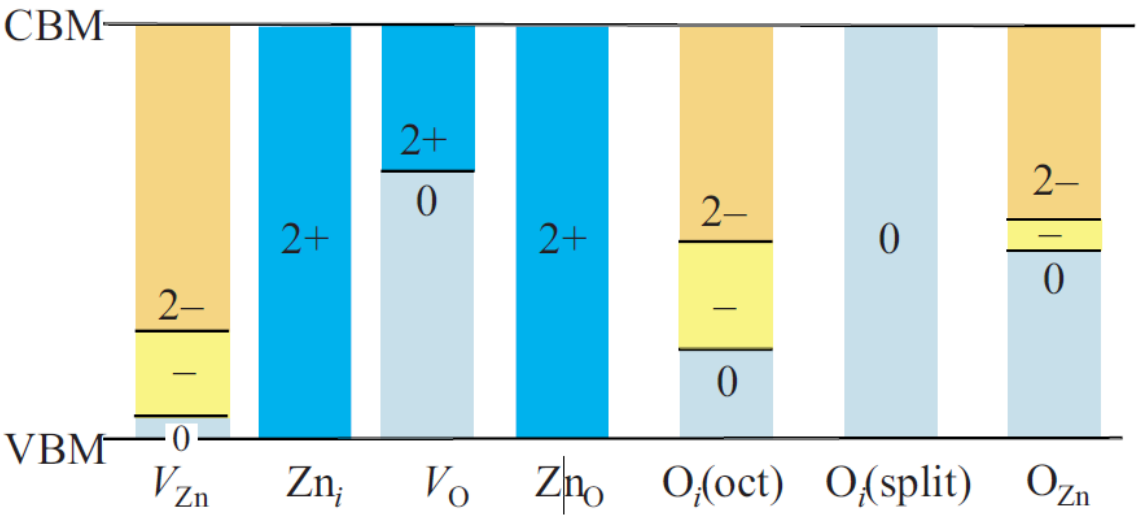

Figure 1.3. Thermodynamic transition levels of intrinsic point defects in ZnO

It is known that the most abundant native point defect is oxygen vacancy because its formation energy is the lowest, but is proven to be a deep level donor. Zinc interstitial defect also can provide free electrons, and its level is in the conduction band. However, its

formation energy is too high, so its impurity concentration is low. Similarly, the energy level of anti-site zinc is placed in the conduction band, and it can provide free electrons, but its impurity concentration is low due to the high formation energy.

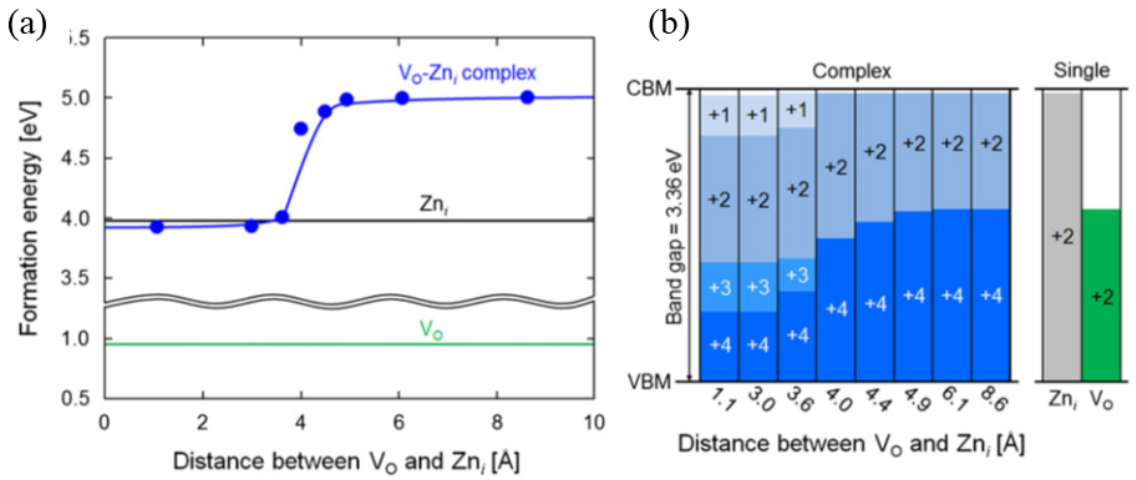

Figure 1.4. (a) Formation energy and (b) position of transition level of V_o-Zn_i complex

As reported by D. H. Kim et al, the n-type characteristics of ZnO is driven by +1 charge state V_o-Zn_i complex as a shallow donor (Figure 1.4) [22]. Hydrogen impurities have also been suggested as the origin, and experimental results have been presented [23]. When hydrogen is placed at the center of the oxygen vacancy, it interacts strongly with dangling bonds and creates fully symmetric states located deep inside the valence band and its anti-bonding states are located in the conduction band, as shown in Figure 1.5. An electron occupied in the anti-bonding state is transferred to the conduction band, making the substitutional hydrogen impurity a shallow donor.

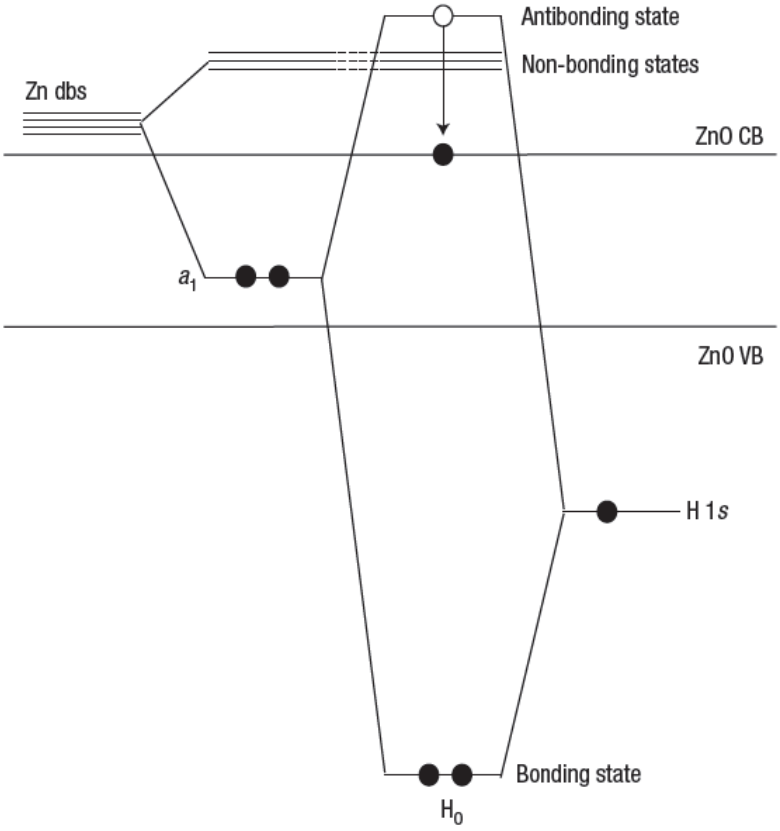

Figure 1.5. Energy diagram of substitutional hydrogen impurity.

In other works, optically activated metastable V_o shallow donor and Zn_i:N complex impurity have been suggested as responsible for the n-type conductivity of ZnO [24]. Synthesis of p-type ZnO has been researched actively for its applications on transistors [25], diodes [26], and light emitting devices [27]. Native p-type ZnO can be synthesized by acceptor-like defects, intentionally generated under oxygen-rich environment. The p-type ZnO can be synthesized by doping with group V elements such as nitrogen, phosphorus, arsenic and antimony but it still needs more research, as the stability of as-synthesized products is not good enough.

1.2. Optical/electrical applications of ZnO

The optical characteristics of ZnO are related to both intrinsic and extrinsic effects as generic semiconductors are. Intrinsic effects are generated by coulomb interaction between electrons in the conduction band, and holes in the valence band or excitons. Even in the ideal crystalline ZnO, intrinsic effects can be generated by the thermal vibration and influenced by its crystal structure. They can affect the electron excitation between the conduction band and the valence band by intrinsic or electrical/optical stimulation, as well as emission properties (e.g. band-edge emission near 376 nm). In contrast to the intrinsic effects, extrinsic effects are generated by crystal imperfections due to the existence of defects or dopants. These dopants or defects create a metastable energy level in the gap between the conduction band and the valence band, and the photon absorption-emission occurs among the defects, the conduction band and the valence band. Optical interactions such as green light photoluminescence, which is known to be caused mainly by oxygen vacancies is caused by extrinsic effects. In any case, whether by intrinsic or extrinsic effects, it provides ZnO a proper energy level difference to interact with visible light (380-750 nm) and long wave ultraviolet A (UVA) (315-400 nm), as shown in Figure 1.6 [28].

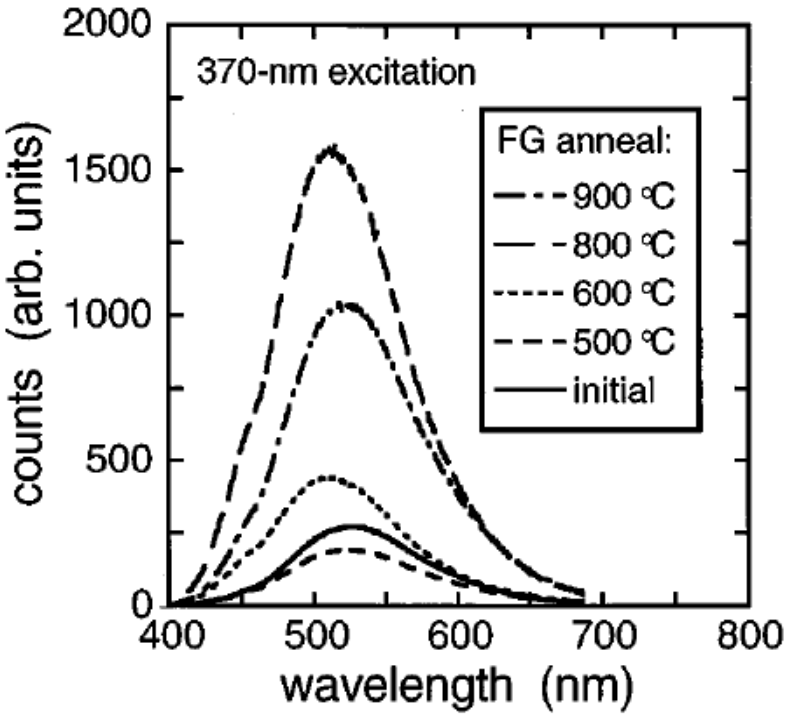

Figure 1.6. Green fluorescence of ZnO annealed in forming gas at various temperature.

The electric applications of ZnO, utilize the inherent n-type characteristics, or the p-type and n-type characteristics of ZnO doped material. Many works that fabricate thin film transistors (TFT) (Figure 1.7) [29], or p-n junction diodes (Figure 1.8) [30] with ZnO have been reported. The semiconducting characteristics of ZnO are widely used but more benefits can be achieved by using both electrical and optical characteristics combined. Light emitting diodes (LED) have been fabricated with ZnO and GaN, as shown in Figure 1.9 [31]. The inherent characteristics of ZnO such as electron carrier concentration, visible transparency, photoluminescence, UV absorption/emission, along with the manipulation of these characteristics through band-gap engineering and doping, make ZnO especially suitable for photovoltaic devices as a transparent window material or an electron transporting material.

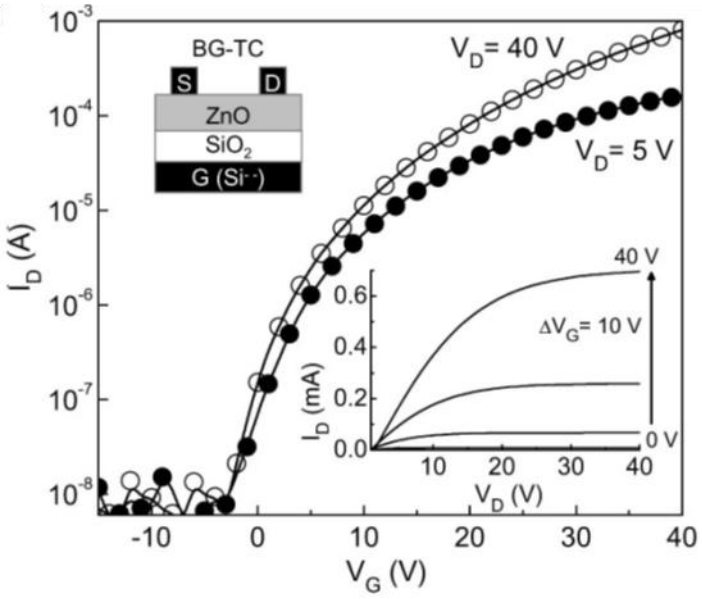

Figure 1.7. I-V transfer and output (inset) characteristics based on ZnO

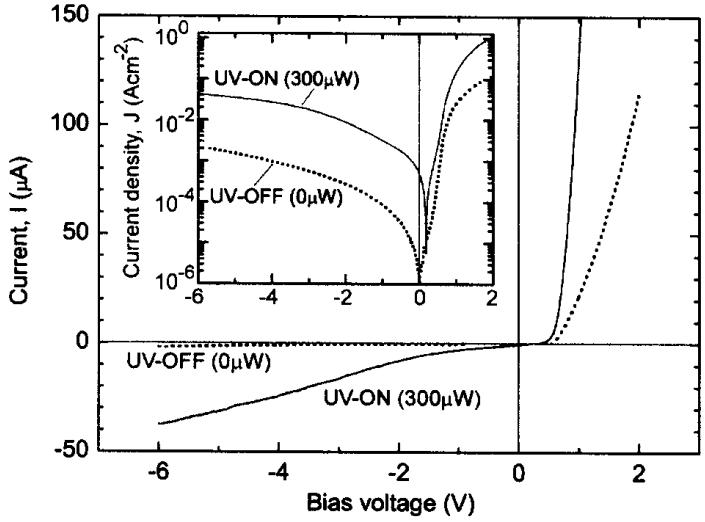

Figure 1.8. P-N heterojunction diode made of ZnO and NiO:Li under dark and illumination state.

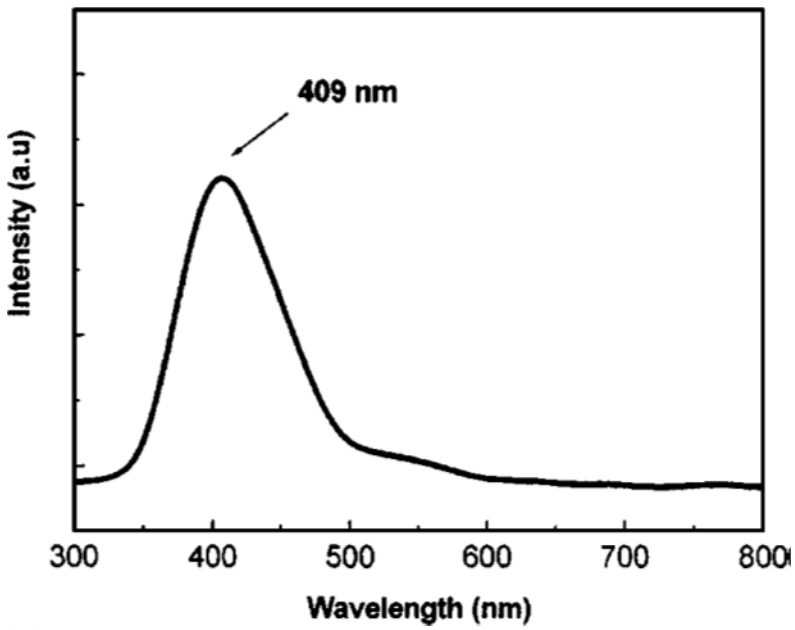

Figure 1.9. Electroluminescence of GaN/ZnO heterostructure.

Indium-doped tin oxide (ITO) and fluorine-doped tin oxide (FTO) have been widely used as transparent conductors but ZnO thin film has also been researched as a viable alternative (Figure 1.10) [32]. The diverse applications of ZnO are dominated by the variety of achievable nanoscale structures that include 1-dimensional nanowires and nanorods, or 2-dimensional sheets. The properties of nanoscale materials are affected by their physical dimensions and characteristics in terms of shape, diameter, thickness, length, and morphology. Therefore, work to control the physical structures of ZnO have been widely attempted and extensively researched in the literature.

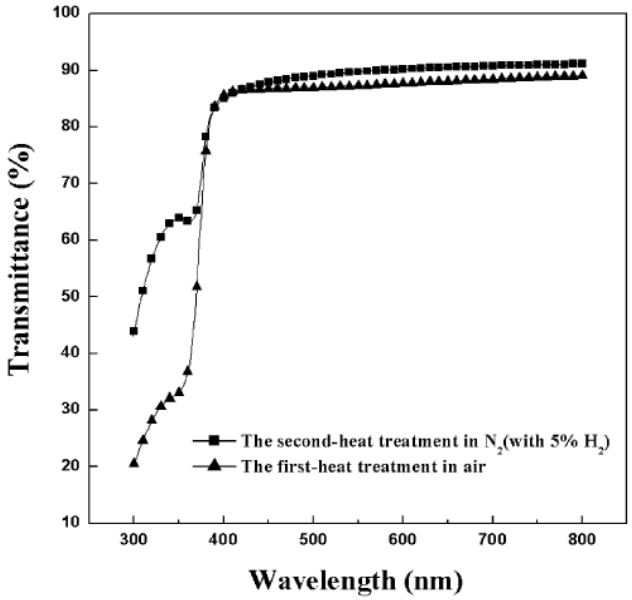

Figure 1.10. Transmittance of ZnO for transparent electrode applications.

1.3. Characteristics and synthesis of 1-D ZnO

In general, wurtzite ZnO is widely used because it is easier to synthesize, and more stable in ambient conditions. The crystal structure of wurtzite ZnO is that Zn cation is filled in the half of the tetrahedral site in the hexagonal closest packed O anions. The ratio of a-axis and c-axis is known as ~1.60 [33], which is slightly smaller than the ratio in the ideal wurtzite structure, 1.633 [34]. This wurtzite ZnO is representatively proper to build 1-dimensional structures easily, so many works have reported the synthesis of 1-dimensional ZnO. In particular, nanoscale 1-dimensional ZnO has been noticed to be appropriate for sub-micro devices due to its semiconducting and light emitting characteristics. Many works applying ZnO nanowires, nanorods and nanoneedles on transistors [35], piezoelectric diodes [36] and light emitting diodes [37] have been reported

Similarly, many diverse synthesis techniques has been developed by wet process including precipitation process [38], sol-gel [39], solvothermal [40], hydrothermal [41] and emulsion [42], and by gas phase process such as physical vapor deposition (PVD) [43] and chemical vapor deposition (CVD) [44]. Among them, template-assisted solution process [45] and CVD are widely used to fabricate 1-dimensional ZnO structures, due to their ease to control conditions during synthesis. In addition, the synthesis of ZnO by molecular beam epitaxy (MBE) [46], pulsed laser deposition (PLD) [47], electrospinning [48], PVD such as sputtering [49], metal-organic CVD (MOCVD) [50] have been reported as well. Because PVD is a technique that forms the product by changing the physical state of the compound, it has the critical disadvantages of requiring high temperature, or the presence of a catalyst. MOCVD and MBE techniques are suitable to grow high quality ZnO but have drawbacks of poor uniformity and limited substrate selection. 1-dimensional ZnO synthesized by electrospinning is in form of polycrystalline structure, so it shows low electrical performance due to its interfacial impedance. Based on the above reasons, template-assisted solution process or CVD process have an advantage in terms of ease of processing, cost-effectiveness, and product quality. The template-assisted solution process has the advantage that controls the morphology of ZnO easily. However, it requires additional steps such as rinsing and drying because it is a wet process, and the potential for contamination or damage of the product is unavoidable. CVD has many advantages as described below in section 1-4, and it becomes a popular method to synthesized high quality 1-dimensional ZnO.

1.4. CVD synthesis

CVD is a technique to synthesize product through the chemical reaction of precursors near the surface of a substrate. It is classified separately from PVD in terms of being accompanied by a chemical reaction, and has advantages in comparison to PVD as follows. First, the reaction temperature can be adjusted according to the chemical species of precursor. In contrast to PVD, the selection of the precursor to provide the gas phase reactant is flexible, and the most suitable precursor for the reaction environment can be selected based on specific criteria. This advantage provides further flexibility for selecting a reaction temperature, and makes possible to synthesize non-volatile materials. Secondly, a competitive advantage is its cost-effectiveness. High vacuum environment is not required for the CVD process, so the process cost is relatively low. Generic low-pressure CVD (LPCVD) is conducted under low vacuum conditions by using a mechanical pump. Atmospheric pressure CVD (APCVD) is processed under atmospheric pressure, and does not require vacuum conditions, making it suitable for continuous processes such as roll-to-roll manufacturing process, potentially reducing the cost of mass-production quite significantly. Thirdly, CVD has the advantage of selectivity of the chemical reaction accompanied by CVD, and high-purity product. Because PVD utilizes heat energy and its interconversion with kinetic energy, purity of product is sensitive to the purity of reactants and the synthesis environment. However, the product in CVD is synthesized through a chemical reaction, and the purity of product is affected by the selectivity of the chemical reaction.

1.4.1. CVD synthesis process

CVD synthesis is characterized by the following process steps:

1) Gasification of reactants: The non-gas phase precursor is heated to generate gas phase reactant.

2) Transport of reactants to substrate surface: Gasified reactant is transferred to the substrate in the reaction chamber.

3) Adsorption of reactants on surface: The transferred reactant is adsorbed on the substrate surface chemically or physically.

4) Reaction: A chemical reaction is processed to produce solid state product. Detailed reaction process is discussed in section 1.4.2.

5) Desorption of by-products: Generated by-product during the reaction is desorbed from the substrate while the solid product is attached on the substrate.

6) Transport of by-products into gas stream: Desorbed by-product is exhausted through the gas stream.

The continuous process of CVD synthesis is illustrated in Figure 1.11 [51].

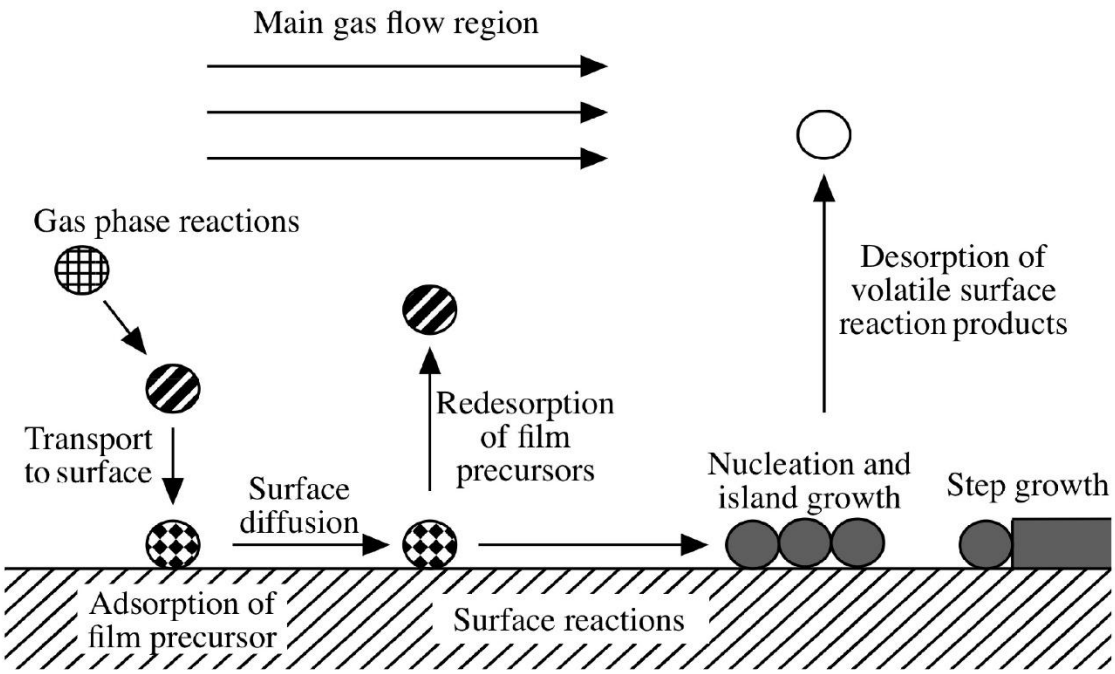

Figure 1.11. Schematic illustration of CVD synthesis process.

1.4.2. CVD synthesis techniques

The following synthesis reactions can be processed by CVD:

1) Pyrolysis: The product is obtained by thermal decomposition of the precursor. Mostly, precursors in the form of hydrates or oxides are decomposed by pyrolysis to obtain metal, metal oxide and metal nitride. It generally requires high reaction temperature because it is the thermal decomposition process. Ex) $AB(g) \rightarrow A(s) + B(g)$

2) Reduction: From the higher oxidation state precursor, product is obtained by reducing the precursor. Hydrogen gas is widely used to derive the reduction reaction. This approach is used to synthesize metal, boride and alloys from oxides or halides precursors. Ex) $AX(g) + H_2(g) \rightarrow A(s) + HX(g)$

3) Oxidation: In contrast to the reduction, the product is obtained from lower oxidation state precursor by oxidization. Various metal oxides are synthesized by reaction of metal and oxygen gas. Ex) $AX(g) + O_2(g) \rightarrow AO(s) + OX(g)$

4) Compound formation: This is generally used to synthesize nitride or oxide compounds. From the reaction of metal halides with ammonia or water vapor, metal nitride and oxide is synthesized (respectively), and halogen acid is produced as a by-product. Ex) $AX(g) + NH_3 \rightarrow AN(s) + HX(g)$, $AX(g) + H_2O(g) \rightarrow AO(s) + HX(g)$

5) Disproportionation: This method is used to produce two asymmetric products from identical compounds. It is used to synthesize metal compounds which can have more than one stable oxidation states. Ex) $2AB(g) \rightarrow A(s) + AB_2(g)$

6) Reversible transfer: In case of reversible transfer, the reaction can be either deposition or etching. The reaction is reversible, which means the direction of the reaction is affected by reaction conditions in the equilibrium state. The direction of reaction depends on the reaction temperature. This reaction is useful as a cleaning process for the reactor.

1.5. CVD synthesis mechanism

One of the most competitive advantages of CVD synthesis is that a wide variety of reaction conditions are acceptable depending on which chemical compound is used as precursor. Any chemical species can be used as precursor, if it can generate gas phase reactant, and it matches the range of parameters conditions. However, one must be careful when selecting the precursor by considering thermodynamics. The reaction derived by

CVD synthesis must be thermodynamically predicted to produce solid state product. It must be an energy advantage for the selected reaction to occur, which can be predicted by considering Gibbs free energy. Gibbs free energy is a thermodynamic potential which is the most useful term to identify theoretically the reaction spontaneity. Detailed thermodynamics analysis is discussed in section 1.5.1. Once the possibility of the reaction is positive, there is additional criteria that the CVD synthesis should meet. First, the precursor should be volatile. In the CVD process, the reactants are transported to the substrate in gas phase, the gasification of precursor should be achievable under the desired temperature. Second, the reaction should produce the solid state product and it should be stable on the substrate in solid form. Third, since the by-product should be removed through the exhaust gas flow, it should be volatile.

1.5.1. Thermodynamics in CVD

As explained in section 1.5, Gibbs free energy is an important factor to estimate the likelihood of the reaction. The Gibbs free energy, G, is defined as $\mathrm{G} = \mathrm{U} + \mathrm{pV} - \mathrm{TS}$ where U is internal energy, p is pressure, V is volume, T is temperature, and S is entropy. From the definition of enthalpy, $\mathrm{H} = \mathrm{U} + \mathrm{pV}$, the Gibbs free energy can also be expressed as $\mathrm{G} = \mathrm{H} - \mathrm{TS}$. In the constant pressure and temperature condition, the spontaneous reaction occurs to the direction of that Gibbs free energy is decreasing ($\Delta \mathrm{G} < 0$). The reaction Gibbs free energy difference (ΔG_r) is calculated as follow [52].

$\Delta G_r = \Sigma \Delta G_f(products) - \Sigma \Delta G_f(reactants)$, where G_f is Gibbs free energy of formation. The ΔG_f can be calculated by following equation [53].

$\Delta G_f(T) = \Delta H_f^0(298) + \int_{298}^{T} C_p\, dT - TS^0(298) - \int_{298}^{T}(C_p/T)dT$, where

$\Delta H_f^0(298)$: Enthalpy of formation

$\Delta S^0(298)$: Standard entropy

$C_p(T)$: Heat capacity at constant pressure

$\Delta G_f(T)$ is a function of temperature and affected by heat capacity at constant pressure

($C_p(T)$) as shown in the equation. $C_p(T)$ is defined as the enthalpy difference followed by temperature and can be expressed as follows[54].

$C_p = a + bT + cT^2 + dT^{-2}$ $(kJ \cdot mol^{-1}K^{-1})$ where a, b, c and d are four different coefficients. Some examples of the coefficients are listed in Table 1.1.

Table 1.1. Coefficients to calculate heat capacity for some gaseous substances.

Substance	**a**	**b×10^3**	**c×10^6**	**d×10^{-6}**
SiH_4	34.39	68.23	−17.79	0.989
SiH_2Cl_2	68.77	36.91	−9.73	−1.546
$SiHCl_3$	86.18	20.77	−5.51	−1.488
$SiCl_4$	103.91	4.80	−1.43	−1.345
$SiCl_2$	56.80	1.68	−0.515	−0.531
H_2	28.00	1.37	0.927	0.0438
HCl	24.43	8.48	−1.445	0.217

After the Gibbs free energy of formation of all chemical species is calculated, spontaneity of the reaction can be determined. In CVD reaction, the thermodynamic precondition is the spontaneous reaction, $\Delta G < 0$.

In the given chemical reaction, the equilibrium constant K_T has a relationship with ΔG_r by the following equation.

$K_T = \exp(-\frac{\Delta G_r}{RT})$, where R is gas constant and T is temperature. A general form of reversible reaction is as follow.

$aA + bB \Leftrightarrow cC + dD$, where lower characters are the mole numbers of each chemical species.

The partial pressure of gaseous chemical species can be calculated from this reaction equation and reaction equilibrium constant. Based on the law of mass action, the relationship between the partial pressure of each chemical species and the equilibrium constant at equilibrium state is determined by the following equation.

$K_T = \frac{p_C^c p_C^d}{p_A^a p_B^b}$, where p_X is the partial pressure of chemical species X.

The ΔG_f of diverse metal oxide to predict the feasibility of reaction can be found in the Ellingham diagram as shown in Figure 1.12 [55].

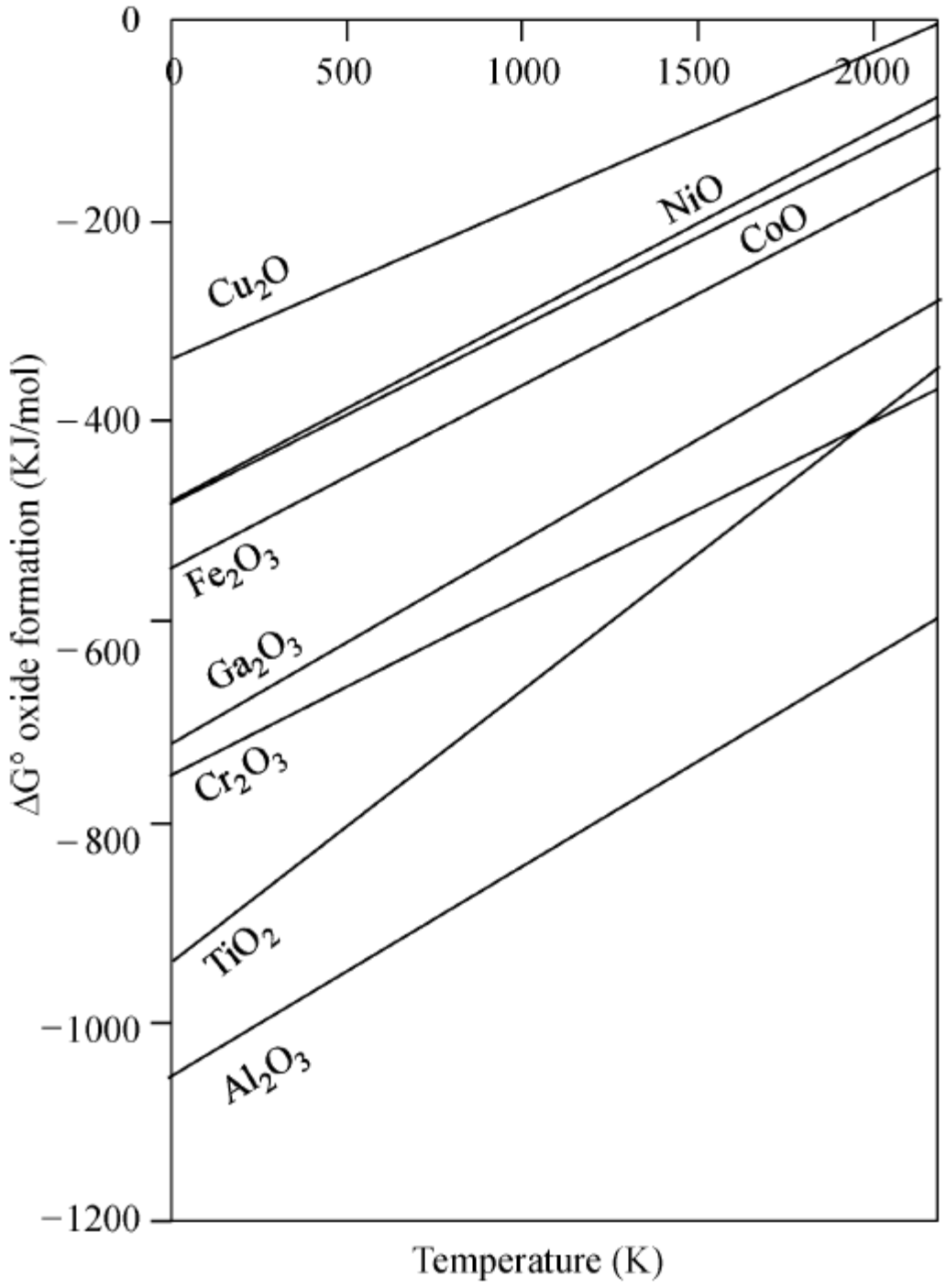

Figure 1.12. Ellingham diagram of oxide formation

1.5.2. Reaction kinetics in CVD

Even if the desired reaction is thermodynamically favored as discussed in session 1.5.1, the reaction rate should be considered in reaction kinetics. In reality, CVD is a non-equivalent process and a complex chemical reaction system, so there are many things to consider. In the CVD reaction kinetics, there are many steps to determine the reaction rate but the three most important steps are as follows.

1) Homogeneous reaction: this type of chemical reaction produces various intermediates before the gas phase reactant reaches the substrate, which affects seed formation and the uniformity of product. Thermodynamic calculations can predict the occurrence of homogeneous reactions and what chemical species can be produced. In the case of hydrocarbons which can form diverse intermediates, the mole fraction of producible chemical species depending on the temperature and pressure is shown in Figure 1.13. The existence of species and its concentration can be predicted thermodynamically.

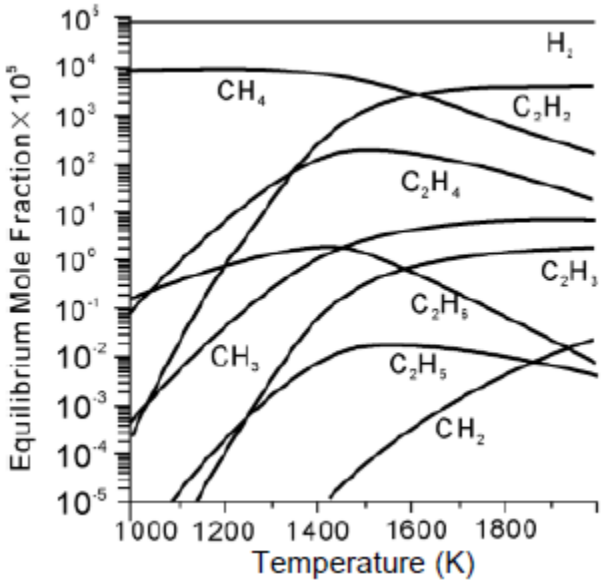

Figure 1.13. Variation of mole fraction of hydrocarbon intermediates at 1 atm.

2) Heterogeneous reaction: this chemical reaction is between the gas phase and the solid phase on the surface of the substrate. After the reactant migrates to a stable location, the heterogeneous reaction occurs to produce solid products.

3) Mass transport: this is a phenomenon where the reactant is transported by the carrier gas. It affects the concentration of reactant near the surface of substrate.

The three reaction steps described above have different rates depending on the given environment, and the slowest step is the rate determination step under the condition. The CVD growth model on the surface of substrate is as follow.

The flux of chemical species which approach to the surface and are adsorbed is determined as $F_1 = h_G \cdot (C_G - C_S)$ where h_G is gas phase mass transport coefficient, C_G is gas phase concentration of chemical species, and C_S is solid phase concentration of chemical species. The flux of chemical species which is consumed during the reaction is determined as $F_2 = k_S \cdot C_S$ where k_S is the rate constant of surface reaction. In the steady state, $F_1 = F_2$, the two equations are combined as $h_G \cdot (C_G - C_S) = k_S \cdot C_S$. Because $C_S = \frac{h_G}{h_G + k_S} C_G$, $F_2 = k_S \cdot C_S = k_S \cdot \frac{h_G}{h_G + k_S} C_G$.

Diffusion rate of gas phase is defined as $\mathrm{D} = D_0 \cdot \frac{T^{3/2}}{P}$ where D_0 is the maximal diffusion coefficient at infinite temperature. The reaction rate constant of the surface reaction is determined as $\mathrm{k} = \mathrm{A}e^{-E_a/RT}$ where A is pre-exponential factor and E_a is activation energy. These two equations show that the diffusion of gas and surface reaction have different rate of change compared to the temperature. Mass transport and surface

reactions are proportional to $T^{3/2}$ and $e^{-E_a/RT}$, respectively. These different rate of change shows how the rate determination step is related to the temperature.

In the low temperature environment, it can be expected that the mass transport is much faster than surface reaction rate. Therefore, it can be approximated that $C_G \approx C_S$ near the surface boundary, so the deposition rate can be expressed as $r \approx k_S C_G$. In contrast, under the high temperature environment, the surface reaction rate increases steeply and the deposition rate can be expressed as $r \approx h_G C_G$. Moreover, in the higher temperature condition, both the mass transport and surface reaction rate are very fast, the deposition rate is limited by the thermodynamic effects. In the case of an endothermic reaction, $\Delta H > 0$, the forward reaction is expedited by increased temperature, so the deposition rate is divergent as temperature increases. However, in an exothermic reaction, $\Delta H < 0$, increasing temperature inhibits the deposition rate, so the rate is decreasing as the temperature increasing. The deposition rate dependence on temperature and change of rate determination step is shown in Figure 1.14.

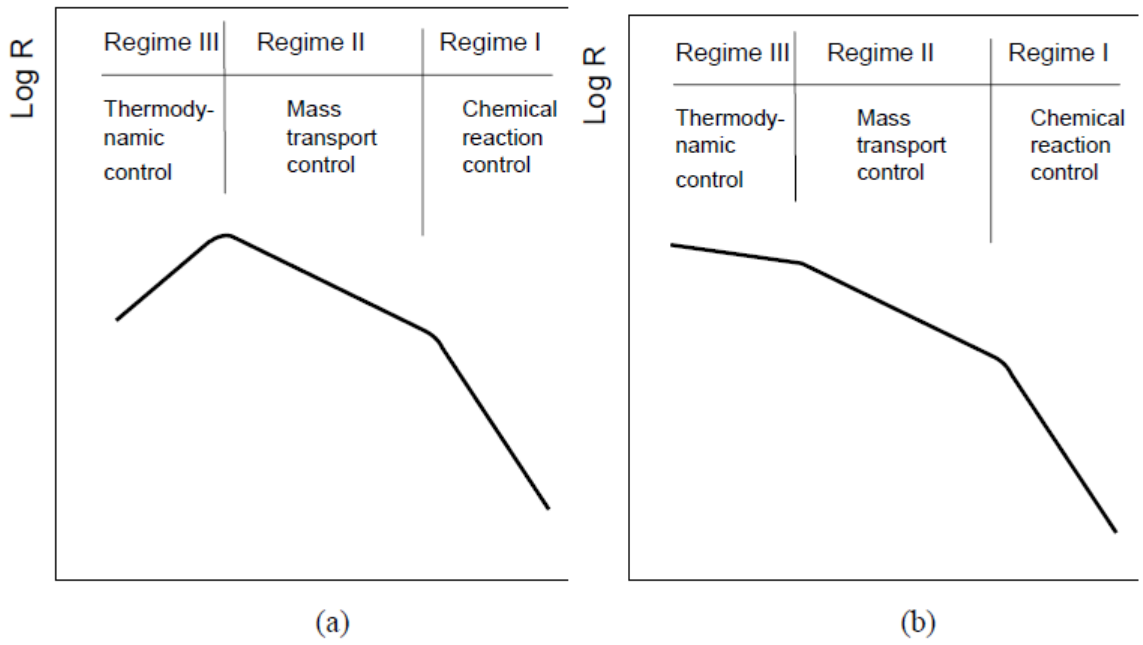

Figure 1.14. Temperature dependence of the deposition rate in (a) exothermic reaction; (b) endothermic reaction.

References

[1] M. Lackoff, X. Prieto, N. Nestle, F. Dehn, and R. Niessner, *Appl. Catal. B-Environ.*, **43**, 205-216 (2003)

[2] C. Hanley, J. Layne, A. Punnoose, K M Reddy, I. Coombs, A. Coombs, K. Feris, and D. Wingett, *Nanotechnology*, **19**, 295103 (2008)

[3] I-T. Tang, H.-J. Chen, W.C. Hwang, Y.C. Wang, M.-P. Houng, and Y.-H. Wang, *J. Cryst. Growth*, **262**, 461-466 (2004)

[4] S. Ekambaram, *J. Alloy. Compd.*, **390**, L4-L6 (2005)

[5] J.-J. Wu, and S.-C. Liu, *Adv. Mater.*, **14**, 215-218 (2002)

[6] J. Pan, Y. Sheng, J. Zhang, P. Haung, X. Zhang, and B. Feng, *ACS Appl. Mater. Interfaces*, **7**, 7878-7883 (2015)

[7] A. Tsukazaki, A. Ohtomo, T. Onuma, M. Ohtani, T. Makino, M. Sumiya, K. Ohtani, S. F. Chichibu, S. Fuke, Y. Segawa, H. Ohno, H. Koinuma, and M. Kawasaki, *Nat. Mater.*, **4**, 42-46 (2005)

[8] W. Zhang, R. Zhu, X. Liu, B. Liu, and S. Ramakrishn, *Appl. Phys. Lett.*, **95**, 043304 (2009)

[9] C. Tian, Q. Zhang, A. Wu, M. Jiang, Z. Liang, B. Jiang, and H. Fu, *Chem. Commun.*, **48**, 2858-2860 (2012)

[10] A. Bashir, P. H. Wobkenberg, J. Smith, J. M. Ball, G. Adamopoulos, D. D. C. Bradley, and T. Anthopoulos, *Adv. Mater.*, **21**, 2226-2231 (2009)

[11] C. M. Ghimeu, J. Schoonman, M. Lumbreras, and M. Siadat, *Appl. Surf, Sci.*, **253**, 7483-7489 (2007)

[12] N. Jones, B. Ray, K. T. Ranjit, and A. C. Manna, *FEMS Microbiol. Lett.*, **279**, 71-76 (2008)

[13] M. Saito, *J. Coated Fabrics*, **23**, 150-164 (1993)

[14] R. Tena-Zaera, J. Elias, and C. Levy-Clement, *Appl. Phys. Lett.*, **93**, 233119 (2008)

[15] Z. A. Lewicka, W. W. Yu, B. L. Olivia, E. Q. Contreras, and V. L. Colvin, *J. Photoch. Photobio. A*, **263**, 24-33 (2013)

[16] H. Morkoc, and U. Ozgur, *Zinc Oxide: Fundamentals, Materials and Device Technology*, (WILEY-VCH Verlag GmbH & Co., 2009)

[17] J. M. Recio, R. Pandey, and V. Luana, *Phys. Rev. B*, **47**, (1993)

[18] R. R. Reeber, *J. Appl. Phys.*, **41**, 5063-5066 (1970)

[19] A. Janotti and C. G Van de Walle, *Rep. Prog. Phys.*, **72**, 126501 (2009)

[20] F. Oba, A. Togo, I. Tanaka, J. Paier and G. Kresse, *Phys. Rev. B*, **77**, 245202 (2008)

[21] A. Janotti, and C. G. Van de Walle, *Phys. Rev. B*, **76**, 165202 (2007)

[22] D.-H. Kim, G.-W. Lee, Y.-C. Kim, *Solid. State Commun.*, **152**, 1711-1714 (2012)

[23] A. Janotti, and C. G. Van De Walle, *Nat. Mater.*, **6**, 44-47 (2007)

[24] D. C. Look, G. C. Farlow, P. Reunchan, S. Limpijumnong, S. B. Zhang, and K. Nordlund, *Phys. Rev. Lett.*, **95**, 225502 (2005)

[25] W. Liu, F. Xiu, K. Sun, Y.-H. Xie, K. L Wang, Y. Wang, J. Zou, Z. Yang, and J. Liu, *J. Am. Chem. Soc.*, **132**, 2498-2499 (2010)

[26] T. Aoki, Y. Hatanaka, and D. C. Look, *Appl. Phys. Lett.*, **76**, 3257-3258 (2000)

[27] A. Tsukazaki, A. Ohtomo, T. Onuma, M. Ohtani, T. Makino, M. Sumiya, K. Ohtani, S. F. Chichibu, S. Fuke, Y. Segawa, H. Ohno, H. Koinuma, and M. Kawasaki, *Nat. Mater.*, **4**, 42-46 (2005)

[28] K. Vanheusden, W. L. Warren, C. H. Seager, D. R. Tallant, J. A. Voigt, and B. E. Gnade, *J. Appl. Phys.*, **79**, 7983-7990 (1996)

[29] A. Bashir, P. H. Wobkenberg, J. Smith, J. M. Ball, G. Adamopoulos, D. D. C. Bradley, and T. D. Anthopoulos, *Adv. Mater.*, **21**, 2226-2231 (2009)

[30] H. Ohta, M. Hirano, K. Nakahara, H. Maruta, T. Tanabe, M. Kamiya, T. Kamiya, and H. Hosono, *Appl. Phys. Lett.*, **83**, 1029-1031 (2003)

[31] D.-K. Hwang, S.-H. Kang, J.-H. Lim, E.-J. Yang, J.-Y. Oh, J.-H. Yang, and S.-J. Park, *Appl. Phys. Lett.*, **86**, 222101 (2005)

[32] J.-H. Lee, K.-H. Ko, and B.-O. Park, *J. Cryst. Growth*, **247**, 119-125 (2003)

[33] S. B. Zhang, S.-H. Wei, and A. Zunger, *Phys. Rev. B*, **63**, 075205 (2001)

[34] H. Schulz, and K.H. Thiemann, *Soild State Commun.*, **23**, 815-819 (1977)

[35] J. Goldberger, D. J. Sirbuly, M. Law, and P. Yang, *J. Phys. Chem. B*, **109**, 9-14 (2005)

[36] H. He, Cheng L. Hsin, J. Liu, L. J. Chen, and Z. L. Wang, *Adv. Mater.*, **19**, 781-784 (2007)

[37] M. A. Zimmler, T. Voss, C. Ronning, and F. Capasso, *Appl. Phys. Lett.*, **94**, 241120 (2009)

[38] S. Sepulveda-Guzman, B. Reeja-Jayan, E. D. L. Rosa, A. Torres-Castro, V. Gonzalez-Gonzales, and M. Jose-Yacaman, *Mater. Chem. Phys.*, **115**, 172-178 (2009)

[39] Y. Sun, J. H. Seo, C. J. Takacs, J. Seifer, and A. J. Heeger, *Adv. Mater.*, **23**, 1679-1683 (2011)

[40] F. Lu, W. Cai, and Y. Zhang, *Adv. Funct. Mater.*, **18**, 1047-1056 (2008)

[41] B. Liu and H. C. Zeng, *J. Am. Chem. Soc.*, **125**, 4430-4431 (2003)

[42] Y. He, *Mater. Chem. Phys.*, **92**, 609-612 (2005)

[43] G. Jimenez-Cadena, E. Comini, M. Ferroni, A. Vomiero, and G. Sberveglieri, *Mater. Chem. Phys.*, **124**, 694-698 (2010)

[44] S. Chu, G. Wang, W. Zhou, Y. Lin, L. Chernyak, J. Zhao, J. Kong, L. Li, J. Ren, and J. Liu, *Nat. Nanotechnol.*, **6**, 506-510 (2011)

[45] M. Fu, J. Zhou, Q. Xiao, B. Li, R. Zong, W. Chen, and J. Zhang, *Adv. Mater.*, **18**, 1001-1004 (2006)

[46] N. Izyumskaya, V. Avrutin, W. Schoch, A. El-Shaer, F. ReuB, Th. Gruber, and A. Waag, *J. Cryst. Growth*, **269**, 356-361 (2004)

[47] X.M. Fan, J.S. Lian, Z.X. Guo, and H.J. Lu, *Appl. Surf. Sci.*, **239**, 176-181 (2005)

[48] Z. Zhang, C. Shao, X. Li, L. Zhang, H. Xue, C. Wang, and Y. Liu, *J. Phys. Chem. C*, **114**, 7920-7925 (2010)

[49] B. T. Khuri-Yakub, J. G. Smits, and T. Barbee, *J. Appl. Phys.*, **52**, 4772 (1981)

[50] V. Sallet, C. Thiandoume, J.F. Rommeluere, A. Lusson, A. Riviere, J.P. Riviere, O. Gorochov, R. Triboulet, V. Munoz-Sanjose, *Mater. Lett.*, **53**, 126-131 (2002)

[51] K. F. Jensen and W. Kern, *Thin Film Processes II*, (Eds. J. L. Vossen and W. Kern, Academic Press, New York, 1991)

[52]Atkins P, Paula J de, *Atkins' physical chemistry, 8th edn.* (Oxford University Press, Oxford, 2006)

[53] L. P. Hunt, *J. Electrochem. Soc.*, **135**, 206-209 (1988)

[54] Hunt, L. P. "Silicon precursors: Their manufacture and properties." *Handbook of semiconductor silicon technology*, (Noyes, Park Ridge, NJ, 1990).

[55] S. Desmoulins-Krawiec, C. Aymonier, A. Loppinet-Serani, F. Weill, S. Gorsse, J. Etourneau, and F. Cansell, *J. Mater. Chem.*, **14**, 228-232 (2003)

Chapter 2

Synthesis of Transparent and Fluorescent ZnO Nanostructure on Transparent Conducting Oxide Electrode

2.1. Introduction

Presently, most of the energy generated worldwide is obtained from fossil fuels such as coal, petroleum and natural gas, making our energy dependency on fossil fuels very high. Coal and petroleum generate large amounts of air pollutants such as carbon monoxide, nitrogen dioxide, and carbon dioxide during their combustion process. Natural gas generates less air pollutants, but the main composition of natural gas is methane, which is not only toxic, but also a greenhouse gas with a warming potential higher that carbon dioxide. Moreover, the amount of fossil fuels is limited, and is taken to be an expendable energy source. In the past decades, research has focused on renewable energy by focusing on next generation energy sources and technologies that are clean, renewable, sustainable, and cost-effective. The most attractive candidates are energy sources that utilize natural phenomena such as solar light, solar heat, geothermal heat, wind power, and tidal energy. That is because its energy source is free and they have a high potential for harvesting and contributing to meeting future energy demands. Among these renewable energy sources, solar energy generation is considered as one of the most promising next generation energy sources due to its environment friendliness, cost-competitive power generation, and good power generation efficiency.

Since the photoelectric effect was first observed, researchers have focused on generating electricity by creating an electric potential within solar cell devices, allowing for the effective separation of charges (exciting electrons), by using sunlight. Power generation from solar cells has been developed for decades, and it is now used in many different fields. From rooftop solar panels, and portable solar cells, to solar panels for satellites with very high efficiency. Over the years many different kind of solar cells have been developed and commercialized. However, monocrystalline silicon solar cells have the inherent limitation that they need to be manufacture on a flat rigid substrate. Research on solar cells with light-weight, portability, flexibility, or improved aesthetics attempts to overcome some of the limitations of monocrystalline silicon solar cells. As a result, next generation solar cells are actively researched.

The first generation solar cells are represented by single junction silicon-based solar cells. Copper-indium-gallium-selenide (CIGS) solar cells, amorphous silicon (a-Si) solar cells, and cadmium telluride (CdTe) solar cells are classified as the second generation thin film solar cells. The third generation solar cells include the following: 1) single molecule or polymer on flexible substrates; 2) multilayer cells, so called tandem cells to increase efficiency; and, 3) organic-inorganic hybrid cells such as dye-sensitized solar cells (DSSCs) and perovskite solar cells (PSCs). Figure 2.1 [1] shows the efficiency and cost projections for each generation solar cells.

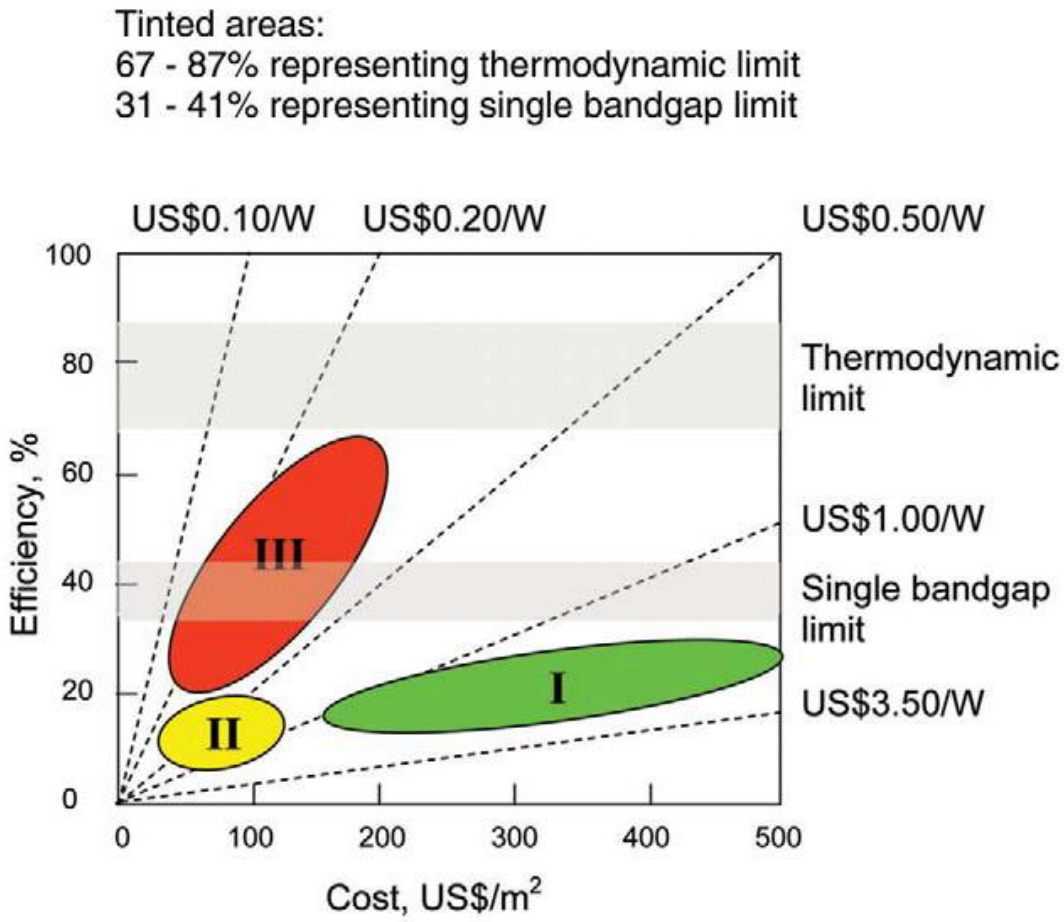

Figure 2.1. Efficiency and cost projections for first, second, and third generation photovoltaic technologies.

Perovskite cells, classified as one of the third generation solar cells, is an advanced type of dye-sensitized solar cell. DSSCs and PSCs are both a type of electrochemical cell, so their operating principle is very similar. In these type of devices, a sensitizer molecule is stimulated by absorbing sunlight, and generates excited electrons. The exciton is separated by the diffusion of excited electrons to the photoelectrode (driven by the internally generated electric potential).

For these solar cells, stacked titanium dioxide (TiO_2) nanoparticles are the most widely used material as the photoelectrode, due to its uniquely excellent photoelectrode performance. However, the stacked nanoparticles (forming about 10 μm layer) have a structural drawback, where the structure is vulnerable to physical stress such as bending and stretching, as shown in Figure 2.2 [2]. Researchers have attempted to overcome this structural drawback by using 1-dimensional structures instead of 0-dimensional TiO_2 nanoparticles. The synthesis, and application of 1-dimensional materials such as zinc oxide (as the photoelectrode) have been reported. A noticeable advantage of the PSCs and DSSCs is that they can be fabricated on an amorphous substrate. Therefore, glass or plastic substrate can be used to fabricate flexible or stretchable cells.

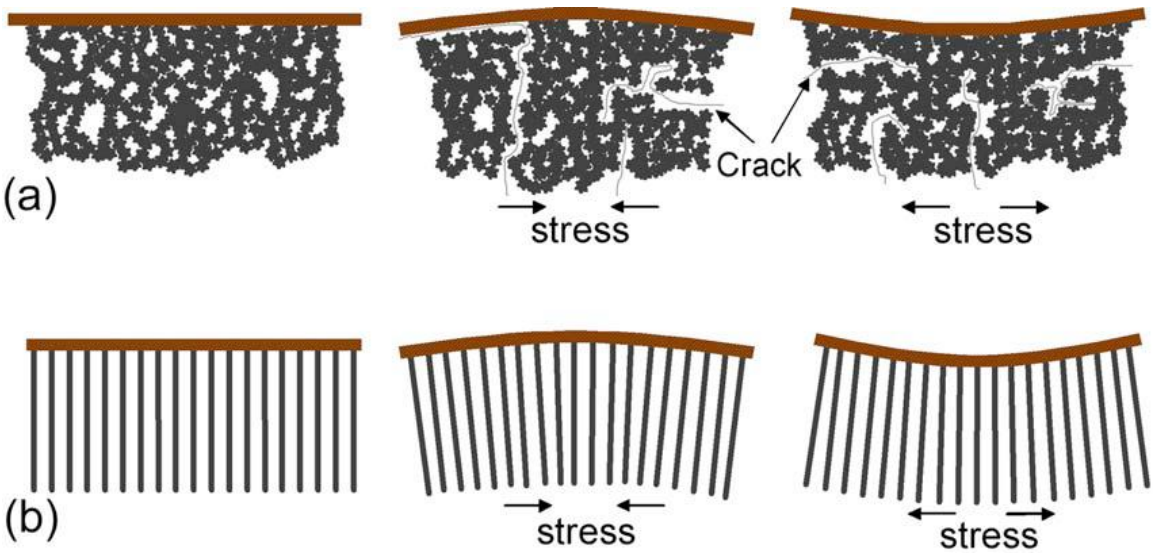

Figure 2.2. Effect of bending stress on (a) stacked nanoparticles; (b) arrayed nanowires;

For the photoelectrode application in solar cell devices, a characteristic the material should have is transparency. Since DSSCs and PSCs have the layered structure as shown in Figure 2.3 [3], the incident light should pass through the transparent electrode and

photoelectrode to reach the sensitizer. If the light is scattered in the photoelectrode layer, its photon-to-current conversion efficiency is significantly decreased. Therefore, the transparency of the photoelectrode is necessary to fabricate high efficiency solar cells.

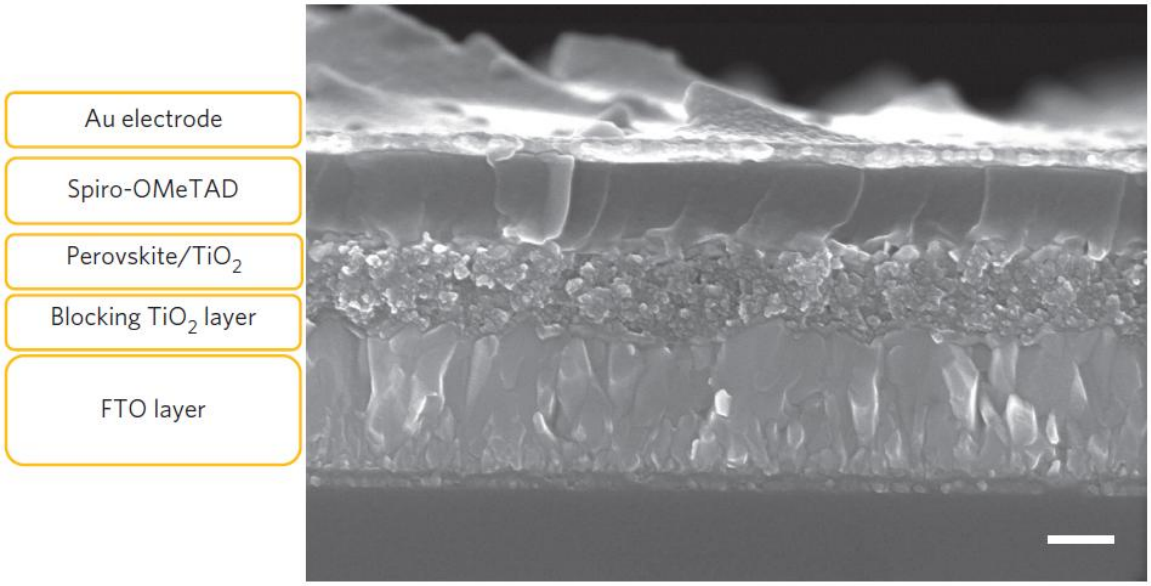

Figure 2.3. Representative cross-sectional SEM view of perovskite solar cell

One of the important characteristics of ZnO is that it can emit green fluorescence light. It absorbs ultraviolet A (UVA) by band edge absorption to generate an excited electron, and the electron emits a broad wavelength fluorescent light near 500 nm wavelength. The fluorescence emission can play a pivotal role when it is applied on photovoltaic cells. Unused UV light is converted to the visible light through the ZnO, and it can be used as a secondary light source.

In this chapter, the LPCVD synthesis, physical, and optical characteristics of 1-dimensional ZnO as a potential photoelectrode for PSCs and DSSCs are discussed. In addition to the structural improvements compared to a TiO_2 photoelectrode, the potential efficiency improvement by the fluorescent ZnO photoelectrode is suggested. Transparent

and fluorescent ZnO, to be used as a photoelectrode to improve overall efficiency of PSCs and DSSCs, was successfully synthesized through LPCVD process. The synthesized ZnO has the physical dimensions and morphology needed to minimize light scattering and improve the transparency of the photoelectrode. Additionally, under the appropriate reaction conditions, fluorescent and transparent ZnO substrates were synthesized by controlling oxygen vacancy impurities.

2.2. Experimental procedure

The synthesis of ZnO was done through LPCVD in this chapter. The reactor used for the experiment was a OTF-1200 three zone furnace from MTI Corporation. A quartz tube with 5 inches diameter was used. All precursors, gases are commercially available without additional purification steps. Zinc powder is used as the precursor, and fluorine-doped tin oxide (FTO) used as the substrate were purchased from Sigma-Aldrich. Nitrogen (99.999%) carrier gas and oxygen gas were purchased from Praxair and Airgas, respectively. The schematic drawing of tube furnace as the reactor is shown in Figure 2.4.

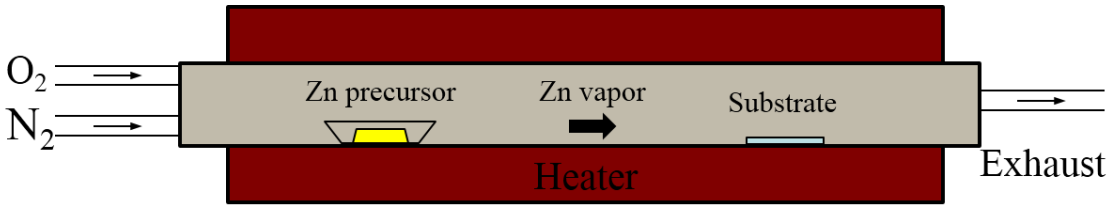

Figure 2.4. Schematic drawing of LPCVD system.

The left side (inlet) of the quartz tube is connected to the gas flow controller, and the right side (outlet) is connected to the exhaust through the mechanical pump. During synthesis, zinc powder is used as the precursor, and the reaction system is set-up as a single-temperature system (e.g. heated to a target temperature throughout the entire tube).

Nitrogen gas and oxygen gas are used as the carrier gas and oxidizer, respectively, and the substrate is FTO coated glass (a transparent conducting oxide suitable for high temperature processes).

About 0.2 g of Zn powder is placed in the quartz precursor boat, and the boat is placed in the tube furnace. A 2 x 2 cm^2 FTO substrate is placed at 1 cm away (downstream) from the precursor boat. The quartz tube in the furnace is connected to the gas flow system, which consists of the following connections: cylinder tank—flow controller—tube furnace—mechanical pump—exhaust. To maintain the gas composition inside of the furnace constant, the tube is purged for 30 minutes at room temperature and heated up to 550℃ with a mixture of nitrogen and oxygen gas. The reaction is carried out for 30 minutes and cooled down by natural convection.

The composition of the gas mixture is optimized to achieve the synthesis of ZnO with both, fluorescent and transparent characteristics. The range of the concentration of oxygen (v/v) is from 0.3% to 10% in nitrogen, while all other conditions are kept constant. Detailed synthesis parameters, conditions, and ranges are listed in Table 2.1.

Table 2.1. Controlled parameters, conditions, and ranges

Controlled parameters	**Conditions range**
Precursor temperature	550℃
Ramping/Reaction time	30 min / 30 min
Pressure	~ 10^{-3} torr
Carrier gas	Nitrogen (N_2)
Oxidizer	Oxygen (O_2)
Flow rate	N_2: 100 SCCM / O_2: 0.5 – 10 SCCM
Precursor-Substrate distance	1 cm downstream
Substrate orientation	Facing up

The as-synthesized ZnO product is characterized the by following techniques.

1) Electron microscopy: The as-synthesized nanostructured ZnO is observed by scanning electron microscope (SEM), and its physical dimensions and morphology are analyzed. The instrument for SEM characterization is Nova NanoSEM 450 SEM from FEI, and it was conducted under accelerating voltage of 20 kV for surface imaging and 5 kV for cross-sectional imaging in immersion mode with through the lens detector (TLD). The sample was prepared by mounted on the aluminum SEM pin holder fixed by carbon tape and grounded by silver paste.

2) X-ray diffraction (XRD) pattern analysis: Crystal structure and crystallinity of the as-synthesized ZnO is confirmed by XRD pattern analysis to support the results observed from SEM. The instrument for the XRD pattern analysis is Empyrean X-ray diffractometer from PANalytical. The XRD pattern was obtained under 45 kV and 40 mA operating condition. The sample was prepared by mounted on the XRD specimen holder with clay.

3) Fluorescence emission analysis: Under the irradiation of 365 nm wavelength UV lamp, the green fluorescence light emission is observed. UV-4NFW MiniMAX UV lamp purchased from Spectroline was used to observe fluorescence emission of synthesized ZnO.

2.3. Results and discussion

Optical characteristics of as-synthesized ZnO regarding light scattering and transparency can be observed by the naked eye. The ZnO synthesized under different oxygen concentration show significantly different optical characteristics.

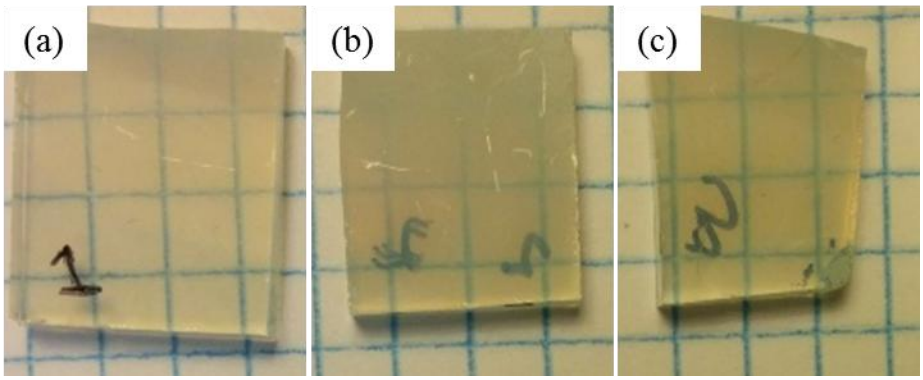

Figure 2.5. Synthesized ZnO under high oxygen ratio; (a) 10%; (b) 8%; (c) 6%.

The synthesized ZnO can be categorized into three different groups by its decreasing oxygen ratio. As shown in Figure 2.5, the synthesized ZnO under high oxygen

ratio (from 10% to 6%) was not formed uniformly on the entire substrate. Under the 10% oxygen ratio, the transparency of the edge closer to the precursor boat and the middle area of the substrate are different. Figure 2.6 shows the surface and cross-sectional SEM images of the ZnO synthesized under a 10% oxygen ratio. Figure 2.6 (a) and (b) are the surface and cross-sectional images taken from the edge area closest to the precursor boat, respectively. Figure 2.6 (c) and (d) are the surface and cross-sectional image taken at the middle area of the substrate, respectively. It is observed that the physical dimensions of ZnO are changed dramatically by the distance from the precursor. From the edge to the middle area, the average diameter of the 1-dimensional ZnO nanostructures decreases from 170 nm to 90 nm, and the average length decreases from 1.11 to 0.62 μm. From the cross-sectional SEM images, it can be observed that a ZnO seed layer is first formed, and from this layer the 1-dimensional ZnO nanostructures are grown. The thickness of the ZnO films is about 738 and 648 nm at the edge and the middle area, respectively. The problem of poor uniformity is lessened when the oxygen ratio is decreased to 8% and 6%, but it not completely eliminated.

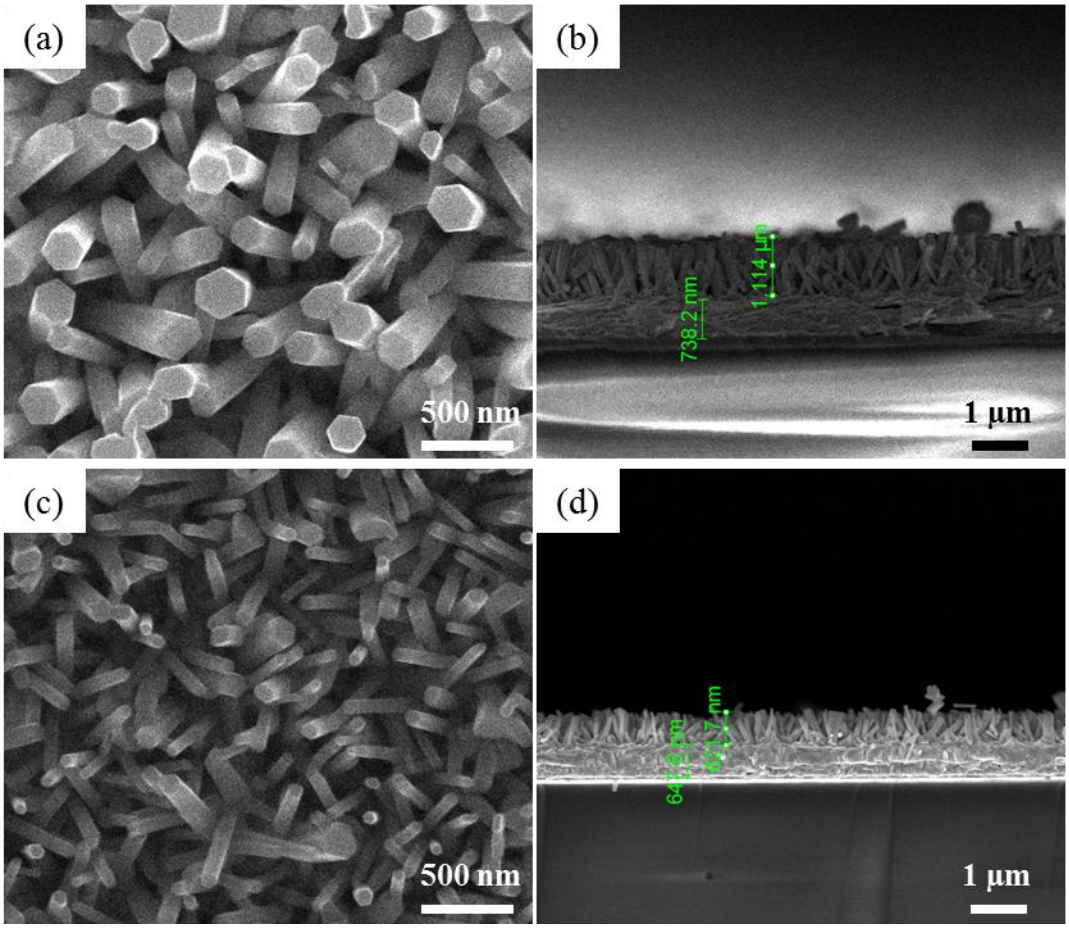

Figure 2.6. The surface and cross-sectional SEM images of ZnO under 10% oxygen ratio; (a) surface image at the edge area; (b) cross-sectional image at the edge area; (c) surface image at the middle area; (d) cross-sectional image at the middle area.

To characterize the fluorescence emission of the products, the as-synthesized material is exposed to the illumination of a 365 nm wavelength light from a UV lamp as shown in Figure 2.7, but none of the substrates shows fluorescence emission characteristics.

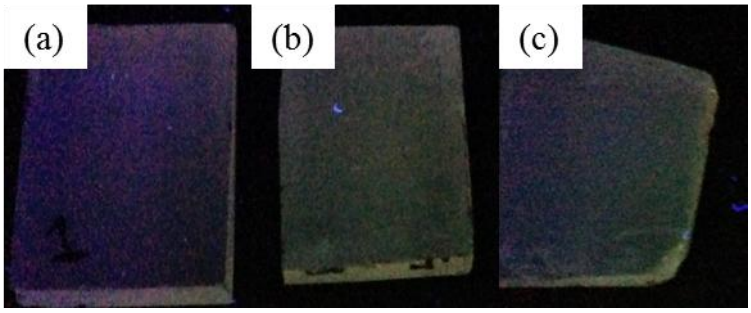

Figure 2.7. The ZnO under 365 nm illumination synthesized by oxygen ratio of; (a) 10%; (b) 8%; (c) 6%.

Based on the observations above, we can conclude that synthesis reaction of ZnO under high oxygen ratio (over 6%) is limited by the zinc concentration in the reaction kinetics. The expected chemical reaction equation is

$$\mathrm{Zn(g)} + {}^{1}/_{2}\, O_2 \rightarrow ZnO(s). \quad (2.1)$$

When there is excessive O_2 during the synthesis, the reaction rate can be approximated as

$$\mathrm{r} = k_1[Zn(g)], \quad (2.2)$$

where k_1 is the reaction rate constant and $[Zn(g)]$ is the zinc partial vapor pressure in the gas phase. The reaction limiting factor is the concentration of Zn vapor under excessive oxygen ratio, so the reaction rate dependency on the Zn concentration is very high. If it is assumed that the available supply of Zn vapor is in radial form from a point source, the local concentration of Zn can be expressed as

$$[\mathrm{Zn(g)}] \propto {}^{1}/_{d^2}, \quad (2.3)$$

where d is the distance from the source. Therefore, under the excessive oxygen environment, the synthesized product shows a gradational dependency, where the growth rate and amount of product decreases, as the distance increases. In addition, the absence of

fluorescence emission is due to the low concentration of oxygen vacancy point defects. Research on the relationship between the green fluorescence emission and oxygen vacancy in ZnO is further investigated by conducting synthesis under conditions that inhibit the generation of oxygen vacancies. The effects of annealing after synthesis is also investigated, and ZnO with low oxygen vacancy concentration is synthesized.

Under the medium concentrations of oxygen environment (from 4% to 1%), the product uniformity and the overall opaqueness of synthesized ZnO is increased as shown in Figure 2.8. Among them, the ZnO synthesized at 1% oxygen condition has a slight transparency unlike the other two (synthesized at 4% and 2%).

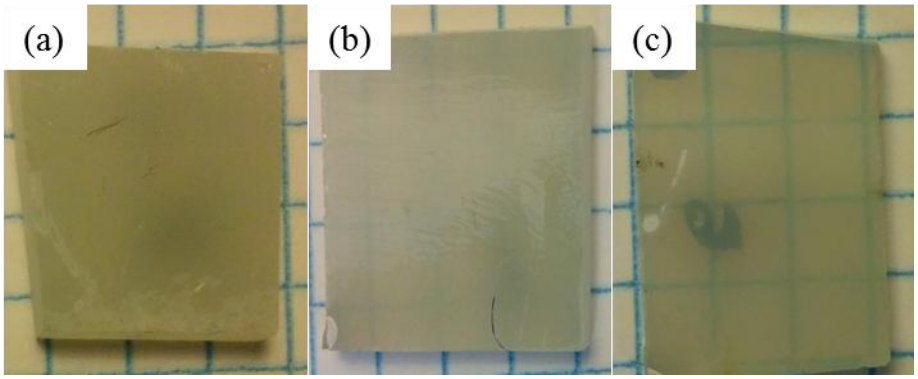

Figure 2.8. Synthesized ZnO under medium oxygen ratio; (a) 4%, (b) 2%, (c) 1%.

In the literature, many publications on the synthesis of ZnO under medium oxygen conditions have been reported [5, 6]. Under these conditions, oxygen ratio is no longer excessive in comparison to zinc, and the reaction proceeds under steady-state reaction equilibrium. The SEM images of these samples are shown in Figure 2.9.

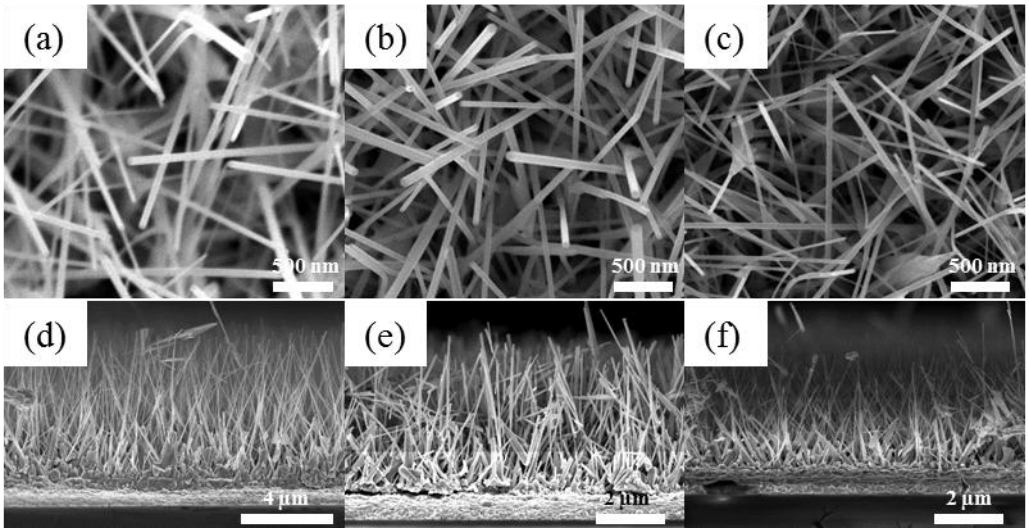

Figure 2.9. Synthesized ZnO under medium oxygen conditions; (a)~(c) are the surface SEM and (d)~(f) are the cross-sectional SEM. (a) and (d), (b) and (e), and (c) and (f) are synthesized under 4%, 2% and 1%, respectively.

The synthesized ZnO 1-dimensional structures have a trend of decreasing diameter and length as the oxygen concentration decreasing. Overall, the 1-dimensional ZnO is vertically aligned, and the morphology is not sensitive to the oxygen ratio during synthesis. From the medium oxygen ratio, fluorescent ZnO structures were synthesized. In Figure 2.10, the fluorescence emission under 365 nm illumination are shown. The ZnO synthesized under 4% oxygen ratio shows more fluorescence emission than the other two.

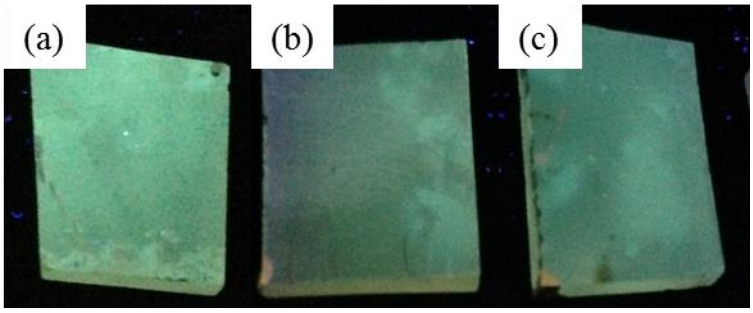

Figure 2.10. Fluorescence emission of synthesized ZnO under medium oxygen ratio; (a) 4%; (b) 2%; (c) 1%.

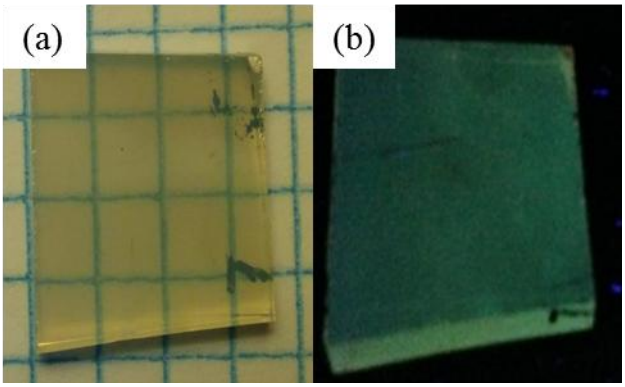

Figure 2.11. ZnO syntehsized under 0.5% oxygen ratio; (a) transparent ZnO; (b) fluorescence emission under 365 nm UV lamp

As the ratio of oxygen decreases, the transparency of synthesized ZnO increases and becomes almost transparent at 0.5% oxygen ratio. As shown in Figure 2.11 (a), the substrate is highly transparent, and the green fluorescence under 365 nm illumination is shown in Figure 2.11 (b). The morphology of synthesized ZnO was observed by SEM. The surface and cross-sectional SEM images are shown in Figure 2.12 (a) and (b), respectively. Similar to the ZnO synthesized under higher oxygen ratio, the ZnO synthesized under 0.5% oxygen ratio also has vertically-aligned nanowire structures. It has very high visible light transparency and fluorescence emission as well. Under the lowest oxygen ratio (0.5%), the high density of synthesized ZnO and their small physical dimensions, make this substrate

the most suitable product for the purpose of this research, which is to obtain a transparent and fluorescent ZnO for photovoltaic applications.

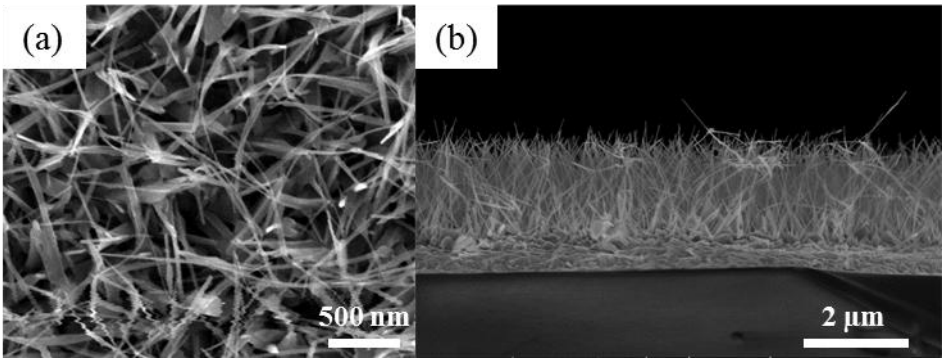

Figure 2.12. ZnO synthesized under 0.5% oxygen ratio; (a) surface SEM image; (b) cross-sectional SEM image.

The crystal structure of synthesized ZnO is characterized by XRD pattern analysis. The XRD results are shown in Figure 2.13. The three patterns are the XRD results for material synthesized under 10%, 4%, 0.5%, respectively.

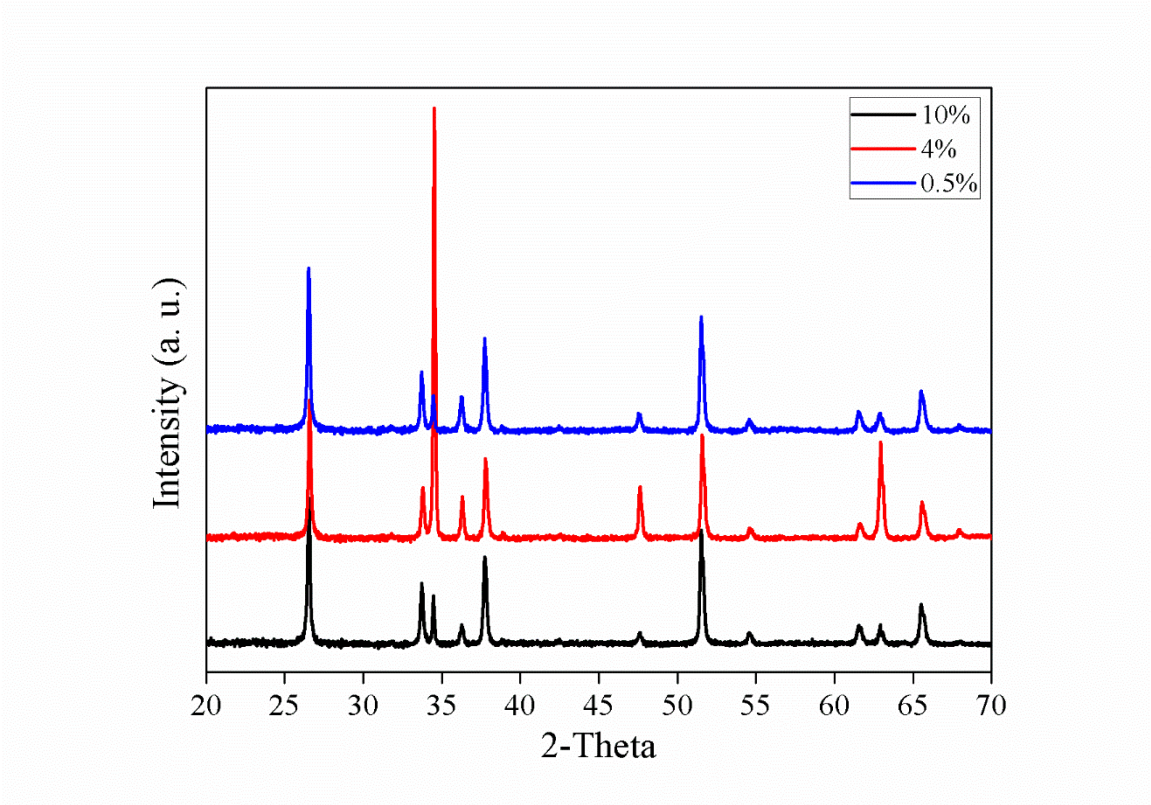

Figure 2.13. XRD pattern of synthesized ZnO

The XRD pattern peaks show that two different crystal structure exists in the sample. The peaks found at 26.52°, 33.71°, 37.74°, 51.50°, 54.63° and 61.53° are from the FTO substrate. The intensities of peaks at the mentioned positions were observed at relatively constant intensity. The peaks found at 34.47°, 36.29°, 47.60° and 62.90° are from ZnO and correspond to (002), (101), (102) and (103) lattice plane, respectively. The other peaks commonly found in wurtzite ZnO such as peaks at 32° and 58° corresponding to (100) and (110) lattice plane, respectively are missing due to the strong directional preference in crystal growth[]. Based on the XRD pattern analysis, the synthesized ZnO is hexagonal wurtzite crystal structure and the three samples have different crystallinity and directional preference. The noticeable difference is the peak at 34.47°, which is a characteristic peak

of wurtzite ZnO. It corresponds to the (002) lattice plane, which is a plane perpendicular to the c-axis. This peak from the ZnO synthesized under 4% oxygen ratio has remarkably high intensity, which means this product has the most distinct directional preference along c-axis. This is a character of 1-dimensional ZnO as observed in SEM results. The secondary dominant peak is observed at 62.90° from (103) lattice plane. It is known that the peak of (103) plane is prominently detected in thin-film form ZnO [7], and the slowest growth plane [8]. The peak intensity ratio of (103) is high in ZnO from 4% oxygen ratio due to the thickness of thin-film layer which is a seed layer for the 1-dimensional ZnO growth.

2.4. Conclusion

In this chapter, the goal of the experimental work is to achieve 1-dimensional ZnO with the characteristics of both fluorescence and transparency, because these two characteristics are attractive for photovoltaic applications. Under the appropriate temperature condition, the crystal growth rate was controlled via the reaction kinetics by adjusting the oxygen ratio. As result, uniform and well-aligned transparent ZnO was successfully synthesized under 0.5% (v/v) oxygen condition. Concurrently, the fluorescent ZnO was synthesized by controlling oxygen vacancy concentration. The ZnO synthesized under optimized CVD synthesis conditions with fluorescent and transparent properties has applicability for photovoltaic devices.

References

[1] G. Conibeer, *Mater. Today*, **10**, 42-50 (2007)

[2] C. Y. Jiang, X. W. Sun, K. W. Tan, G. Q. Lo, A. K. K. Kyaw, and D. L. Kwong, *Appl. Phys. Lett.*, **92**, 143101 (2008)

[3] F. Hao, C. C. Stoumpos, D. H. Cao, R. P. H. Chang, and M. G. Kanatzidis, *Nat. Photonics*, **8**, 489-494 (2014)

[4] T. Gao, and T. H. Wang, *Appl. Phys. A*, **80**, 1451-1454 (2005)

[5] P.-C. Chang, Z. Fan, D. Wang, W.-Y. Tseng, W.-A. Chiou, J. Hong, and J. G. Lu, *Chem. Mater.*, **16**, 5133-5137 (2004)

[6] N. Zhang, R. Yi, R. Shi, G. Gao, G. Chen, and X. Liu, *Mater. Lett.*, **63**, 496-499 (2009)

[7] Y. Wang, X. Li, G. Jiang, W. Liu, and C. Zhu, *J. Mater. Sci.*, **24**, 3764-3767 (2013)

[8] J. D Pedersen, H. J Esposito and K. S. The, *Nanoscale Res. Lett.*, **6**, 568 (2011)

Chapter 3.

LPCVD Synthesis of Vertically Aligned 1-Dimensional Photocatalytic ZnO by Preventing the Premature Oxidation of Zn Precursor

3.1. Introduction

Similar to titanium dioxide (TiO_2), ZnO is a well-known photocatalytic material. As shown in Figure 3.1, the ZnO acts as a catalyst under illumination to decompose the organic dye methylene blue [1]. The charge separation induced by the piezoelectricity of ZnO, further enhances the efficiency of methylene blue decomposition. It was reported that forming heterogeneous fibers of ZnO with TiO_2 improves photocatalytic activity, as shown in Figure 3.2 [2].

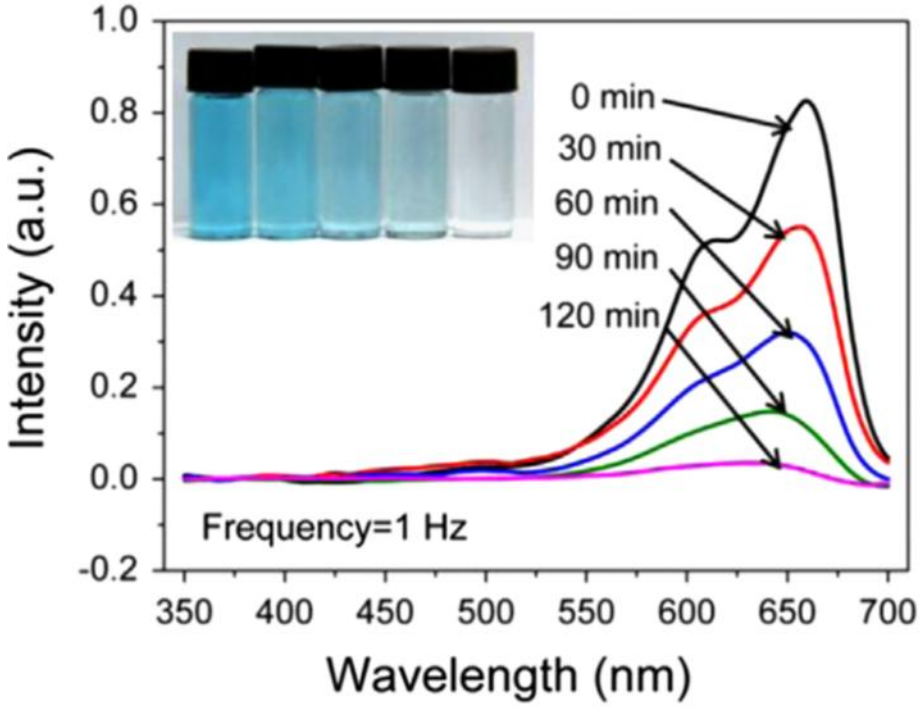

Figure 3.1. Photodegradation of methylene blue solution with ZnO photocatalyst.

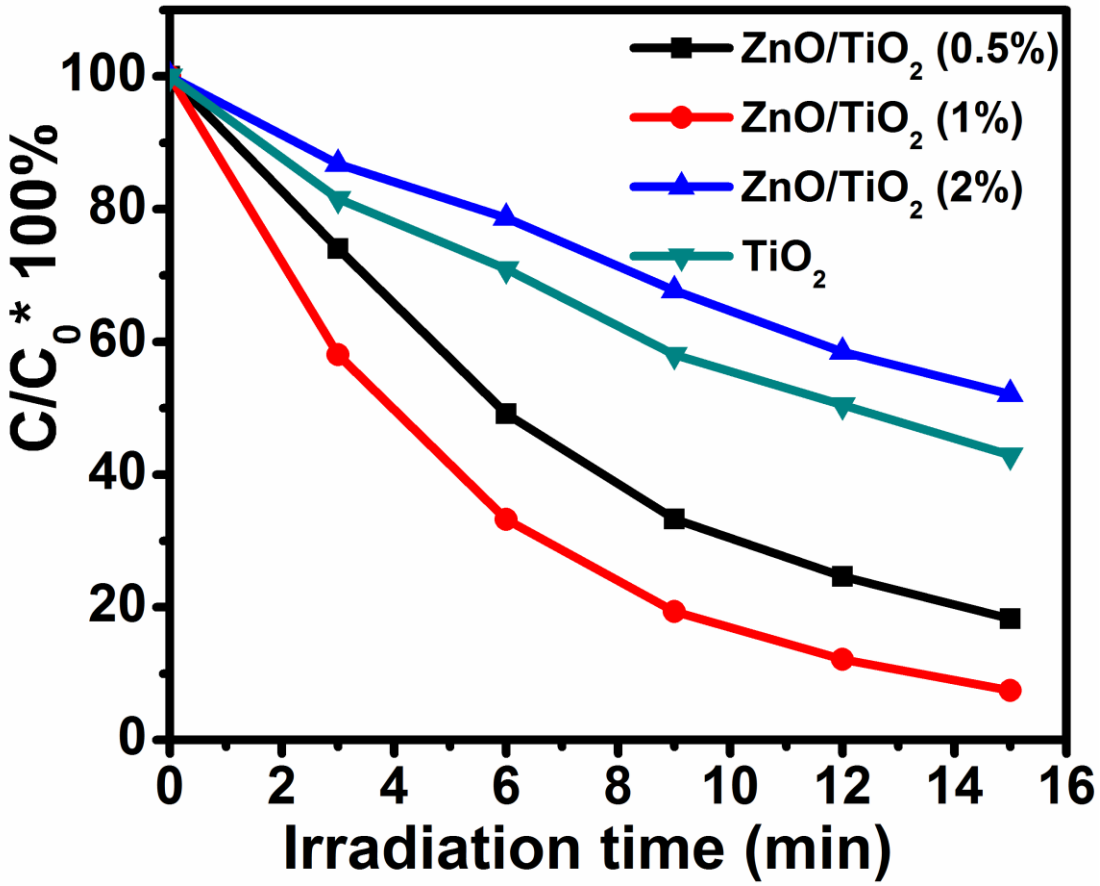

Figure 3.2. Photocatalytic performance of ZnO/TiO_2 hybrid nanofibers.

The photocatalytic characteristics of ZnO make possible not only the photodecomposition and purification by photocatalysis, but also its application as a photoelectrode for photovoltaic devices, such as in dye-sensitized solar cells (DSSCs). By performing morphological modifications to ZnO, improvements in photocatalytic activity and photovoltaic efficiency in DSSCs have been reported [3]. The dependence on morphology vs. photocatalytic and phototvoltaic properties were studied by comparing different structures. Three different structures, microsphere, yolk/shell, and hollow microsphere were compared in their photodecomposition properties on rhodamine B (Figure 3.3 (a),) and their photovoltaic efficiency in DSSCs (Figure 3.3 (b)). The hollow

sphere structured ZnO, with a dominant (101) plane, was synthesized by solvothermal reaction. This hollow microsphere structure showed the best performance for both applications, due to its large surface area and light scattering inside of the hollow sphere.

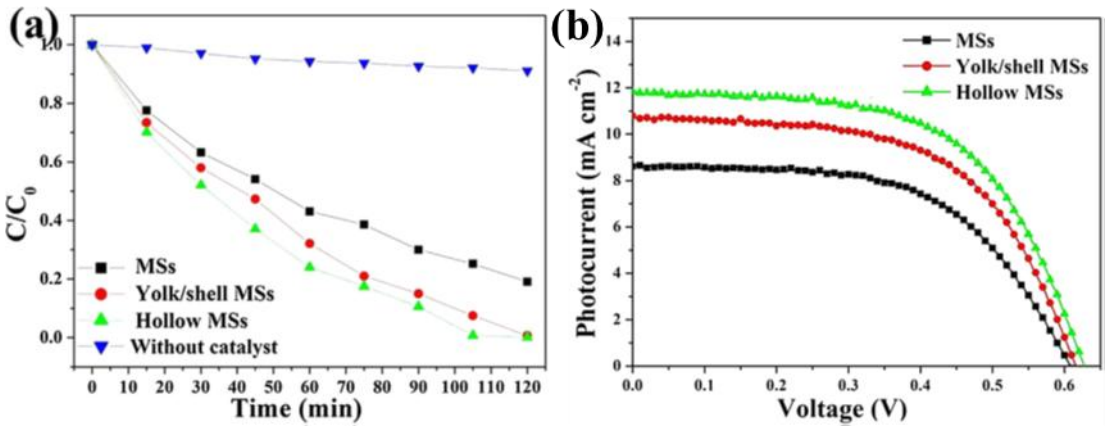

Figure 3.3. Morphology dependence of ZnO as (a) photocatalyst; (b) photoelectrode.

A DSSC is an artificial photosynthetic light harvesting device, which mimics the photosynthesis in plants [4]. Similar to chlorophyll, which is a light sensitizing pigment in plants that induces photosynthesis by a photocatalytic process under illumination, the sensitizer molecule and photoelectrode produce free electrons in DSSCs. In Figure 3.4, the process of DSSC operation and photosynthesis are illustrated [5]. Chlorophyll and xanthophyll are used as dye molecules in DSSCs, replacing the photosystem II and photosystem I, respectively.

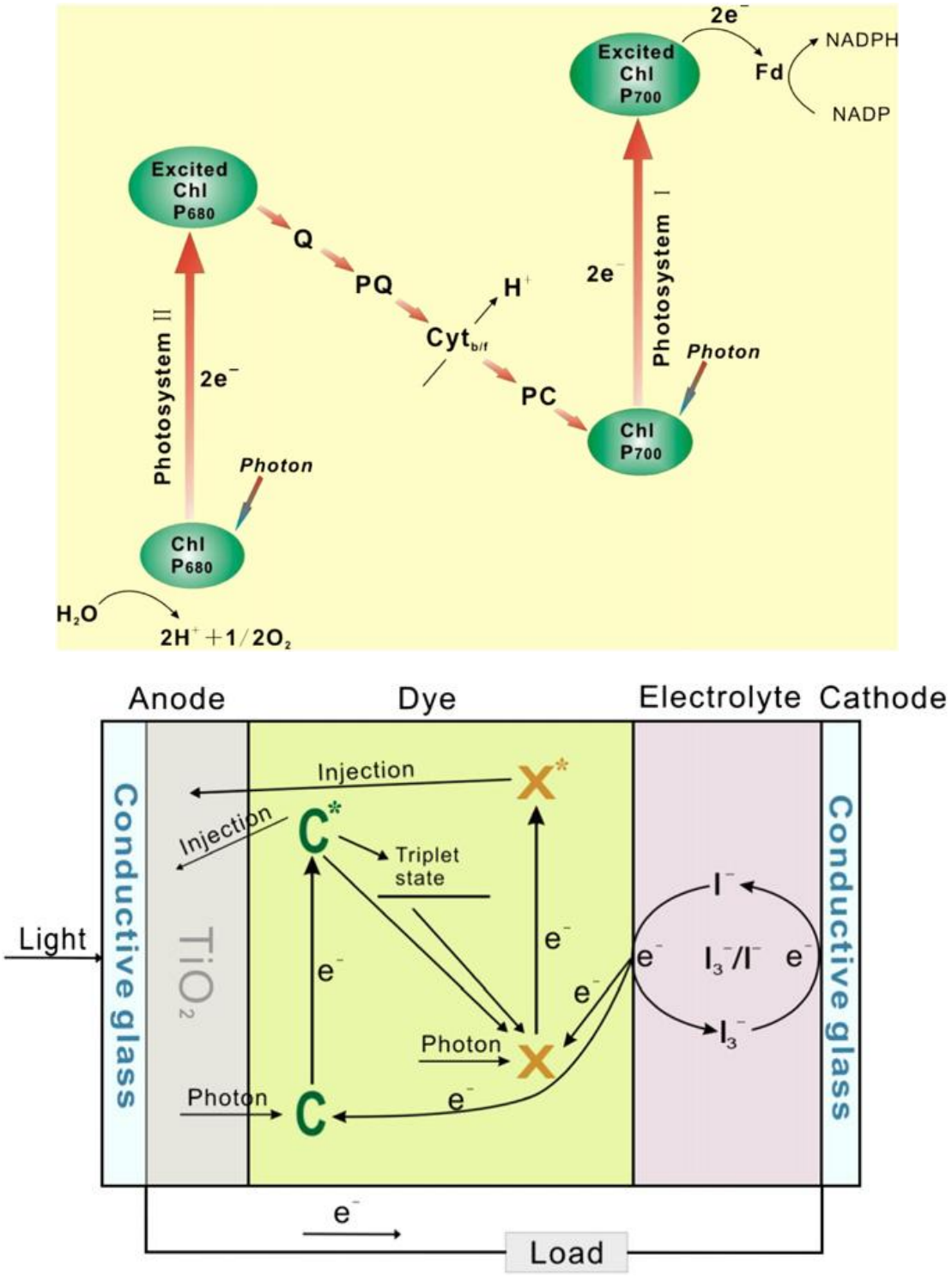

Figure 3.4. The analogous nature of photosynthesis process and DSSC operating process.

Diverse synthesis methods and techniques to synthesize ZnO have been reported in the literature. Research on synthesis of 0-dimensional quantum dots, 1-dimensional nanowires or nanorods, and 2-dimensional nanoribbons, or sheets have been investigated by many researchers. Template-assisted solution growth process is widely used due to its simple process and cost-effectiveness. However, this process has drawbacks that are inherent to wet processes such as contamination during rinsing. Methods using vapor phase reaction are favored to produce high quality and purity materials. Physical vapor deposition (PVD) techniques such as sputtering and evaporating have been used to synthesize ZnO. However, these processes also have disadvantages, mainly due to the requirements for a high vacuum environment, and the need for high purity precursors for obtaining a high quality product. In contrast, a CVD technique does not require high vacuum conditions, and the high purity of a product depends on the selectivity of the chemical reaction. The fact that the synthesis environment can be optimized depending on the experimental materials such as precursor or substrate, is one of the major advantages of CVD techniques.

ZnO synthesis from zinc powder through CVD process is illustrated as shown in Figure 3.5. A tubular reactor is placed in a tube furnace and the precursor and substrate are placed in the reactor. The reactor is heated up to the desired reaction temperature while the carrier gas (e.g. argon, nitrogen), and the oxidizing gas (i.e. oxygen gas) are flown through the reactor tube. The precursor vapor gasified by the heat is transferred to the substrate by the carrier gas, and it is adsorbed on the surface of the target substrate. The oxidation reaction with the oxygen gas, forms solid phase ZnO on the target substrate.

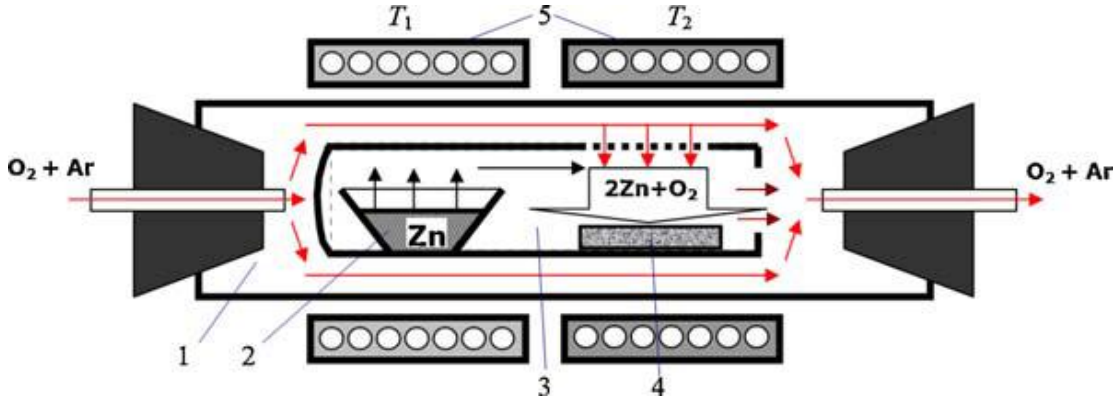

Figure 3.5. Schematic illustration of ZnO synthesis via CVD.

However, as the reaction proceeds, it is possible that the reaction is limited by the zinc reactant supply. The density of ZnO is known as 5.606 g/cm^3 [6], and the density of liquid zinc near melting point is known as 6.553 g/cm^3 [7]. Since oxygen gas is available near the precursor boat, it is possible that the oxidation of zinc takes place in the precursor boat before zinc is able to evaporate. Since the density of ZnO is lower than zinc, the ZnO floats on the liquefied zinc and it forms an oxide layer over time. Even though there was enough amount of zinc precursor at the initial stage of the reaction, the supply of zinc vapor is not maintained during synthesis, as the premature oxidation of Zn takes place at the precursor boat. Over time the supply of zinc vapor is gradually decreased and no more zinc vapor is produced after the oxide layer forms. The partial pressure of the reactant is a critical factor in the gas phase reaction, but it become uncontrollable due to the premature oxidation of the precursor as explained above.

In this chapter, the CVD synthesis of ZnO is demonstrated by preventing the premature oxidation of Zn by using a test tube-shaped precursor boat instead of using traditional bowl-shaped boat. As illustrated in Figure 3.6, in the test tube-shaped precursor

boat, a positive pressure is generated inside of the precursor boat by evaporation of the zinc precursor. The positive pressure inhibits the invasion of oxygen gas into the precursor boat, preventing the premature oxidation of zinc precursor. The flow of oxygen and zinc vapor are controlled fluid dynamically to synthesize high quality zinc oxide. Additionally, from the ease of vaporization due to the absence of oxygen near the precursor boat, a low-temperature synthesis process is successfully developed. The low-temperature process provides for the growth of the synthesized ZnO material onto a larger area.

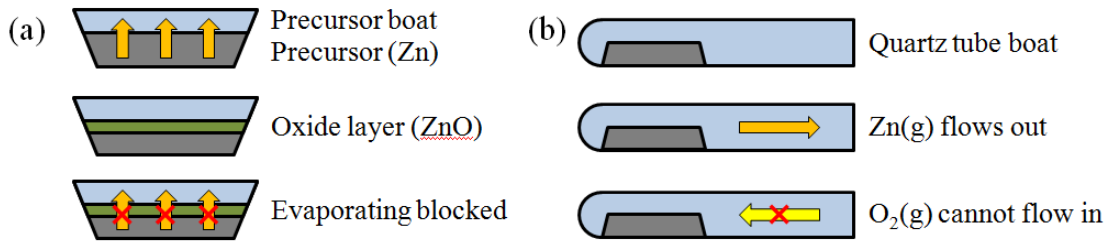

Figure 3.6. Schematic illustration of ZnO synthesis with; (a) bowl-shaped boat; (b) test tube-shaped boat.

3.2. Experimental procedure

The synthesis of ZnO was conducted in a three-zone tube furnace, OTF-1200, from MTI, under low vacuum condition generated by a mechanical pump. All the materials used for this experiment are commercially purchased and no additional purification or treatment is applied. A pre-cut FTO in 2 x 2 cm^2 glass substrate was cleaned by ultrasonication in detergent solution, acetone, and 2-propanol for 15 minutes each. 0.2 g of zinc powder was placed in a precursor boat, and loaded into the tube furnace. To compare the effect of precursor boat shape, both the bowl-shaped boat and test tube-shaped boat are used separately. The prepared FTO was placed 1 cm away from the precursor boat downstream

the tube furnace. The inlet and outlet of the tube is connected to gas flow controller and mechanical pump, respectively, and hermetically sealed. The inside of reactor was purged for 15 minutes with a mixture of 100 SCCM nitrogen, and 4 SCCM oxygen gas. The furnace was ramped to 470℃ over 30 minutes and the temperature was maintained for another 30 minutes for the reaction. The synthesis was completed by allowing cooling down of the furnace by natural convection.

DSSC devices are fabricated with the synthesized ZnO as the photoelectrode. A ruthenium complex compound, named as N719 (Figure 3.7) [8], is used as the light sensitizer. A thin platinum film is used as the counter electrode, and iodide/triiodide redox couple is used as the ionic charge carrier in the electrolyte. The N719 molecules were adsorbed on the surface of ZnO by soaking the FTO glass with synthesized ZnO into the N719 solution. To make the platinum thin film counter electrode, hexachloroplatinic acid hexahydrate ($H_2PtCl_6 \cdot 6H_2O$) is spin-coated on a cleaned FTO substrate. After sintering, the platinum thin film is formed by the reduction reaction of Pt(II) to Pt(0). To fabricate the DSSC device, the two electrodes were sandwiched and sealed with a surlyn hot melting film. After the sealing of the device, the fabrication of the DSSC devices was completed by the injection of the electrolyte solution. The structure of fabricated DSSC is illustrated in Figure 3.8.

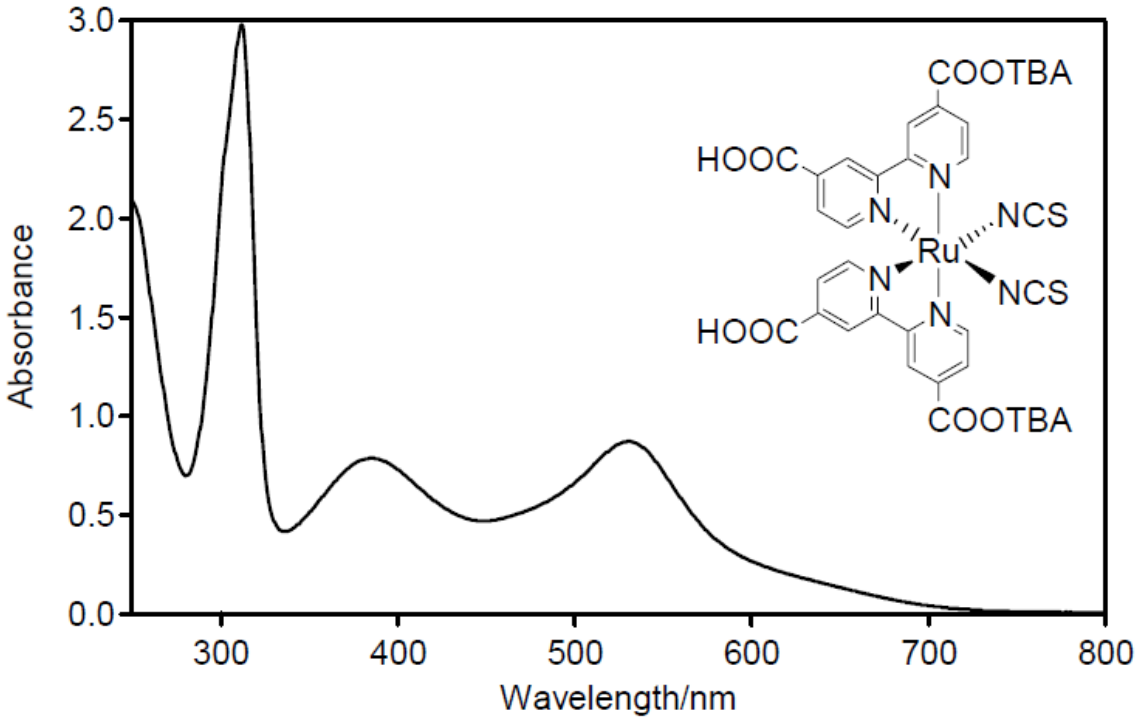

Figure 3.7. UV-vis spectrum and molecular structure (inset) of N719

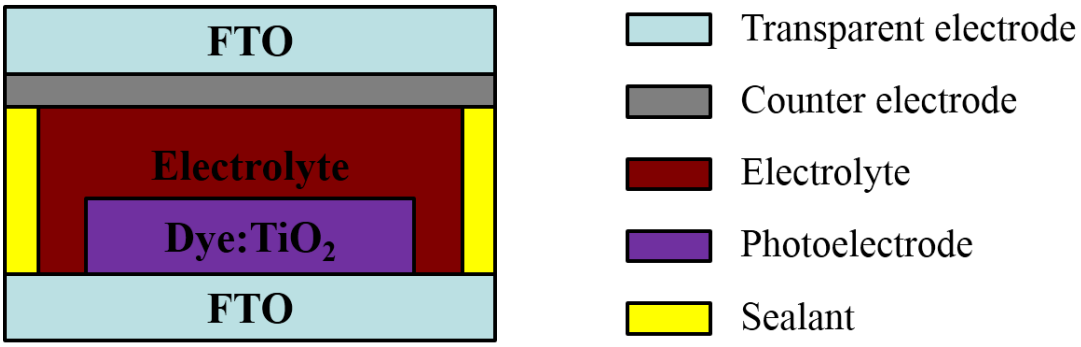

Figure 3.8. Structure of fabricated DSSC.

The synthesized ZnO is characterized by the following techniques. The morphology and physical dimensions are observed by scanning electron microscopy (SEM) with Nova NanoSEM 450 under 18 and 20 kV accelerating voltage for surface imaging and 5 kV for cross-sectional imaging with Everhart-Thornley detector (ETD) and TLD.

The sample for the SEM characterization was by mounted on the aluminum SEM pin holder fixed by carbon tape and grounded by silver paint. The crystal structure and crystallinity of synthesized ZnO was analyzed by X-ray pattern (XRD) analysis by Empyrean X-ray diffractometer from PANalytical under 45 kV and 40 mA condition. The sample preparation for the XRD analysis was done by mounted on the XRD specimen holder fixed with clay. The photovoltaic property of fabricated DSSCs is conducted with a solar simulator and Agilent 4155 semiconductor analyzer.

3.3. Results and discussion

The surface SEM image of FTO substrate is shown in Figure 3.9. FTO with about 50 nm to 500 nm size and pebble-like structure is used as the substrate. On the substrate, synthesized ZnO with traditional bowl-shaped boat is shown in Figure 3.10. Figure 3.10 (a) is an image observed near the edge closer to the precursor boat and (b), (c), and (d) are at about 0.5 cm away from each other, moving along the axis of gas flow. The image in Figure 3.11 (a) is taken near the edge, and (b) is taken at the center of the substrate.

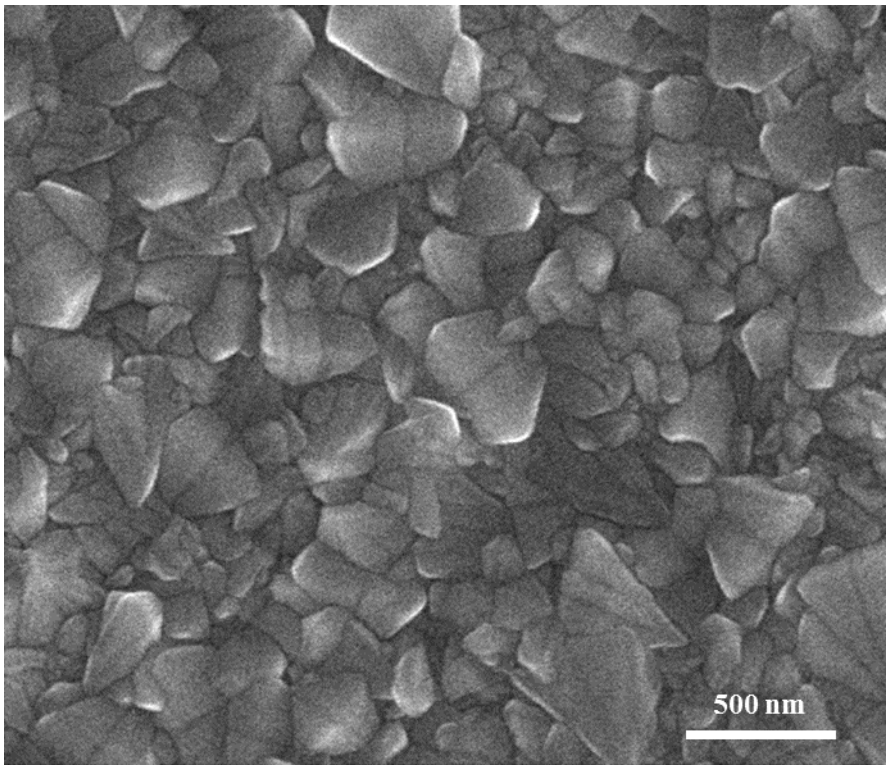

Figure 3.9. Surface SEM image of FTO substrate.

The results observed in Figure 3.10 and 3.11 show that the physical dimension of synthesized 1-dimensional ZnO decrease as the distance from precursor boat increase. The reason can be understood from the synthesis environment. The synthesis is conducted under the temperature of 470℃, and it is only about 50℃ above the melting temperature of zinc. This temperature is relatively low in comparison with the CVD synthesis temperature of ZnO from other research publications [9-11]. The supply of reactant is not sufficient due to the low temperature environment. The mixture of 100 SCCM nitrogen and 4 SCCM oxygen environment is not an oxygen excessive condition. However, supply of zinc vapor is slower, so the oxygen is relatively excessive in the low temperature synthesis system. Therefore, zinc near the substrate reacted with excessive oxygen and

consumed rapidly, and the gradation of zinc vapor partial pressure was generated. The diameter of 1-dimensional ZnO observed near edge was about 80 nm and decreases down to 24 nm as the distance from the boat increases. As shown in Figure 3.11 (a) and (b), the thickness of the formed ZnO film shows a huge difference from 940 nm near edge to 240 nm at center of the substrate.

It is also expected that the premature oxidation of zinc at the precursor boat happens due to the existence of oxygen gas near the precursor boat, and because it is a low-temperature and slow-rate reaction. The amount of synthesized ZnO (thickness of the film) is low because the supply of zinc vapor reactant is inhibited by the oxide formation at the precursor boat.

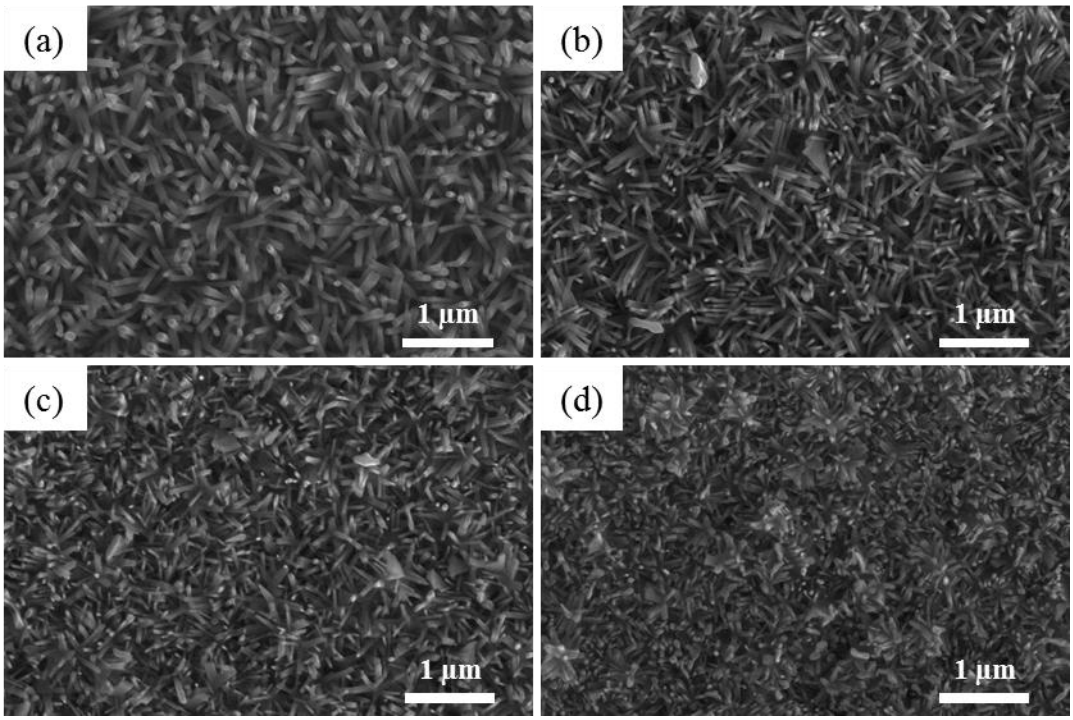

Figure 3.10. Surface SEM image of ZnO synthesized with traditional bowl-shaped boat; (a) near the edge close to the precursor boat; (b) 0.5, (c) 1.0, (d) 1.5 cm away from the edge.

Overall, the synthesized ZnO under 470℃ temperature with bowl-shaped boat does not have sufficient amount of product to be used as a photoelectrode for DSSCs.

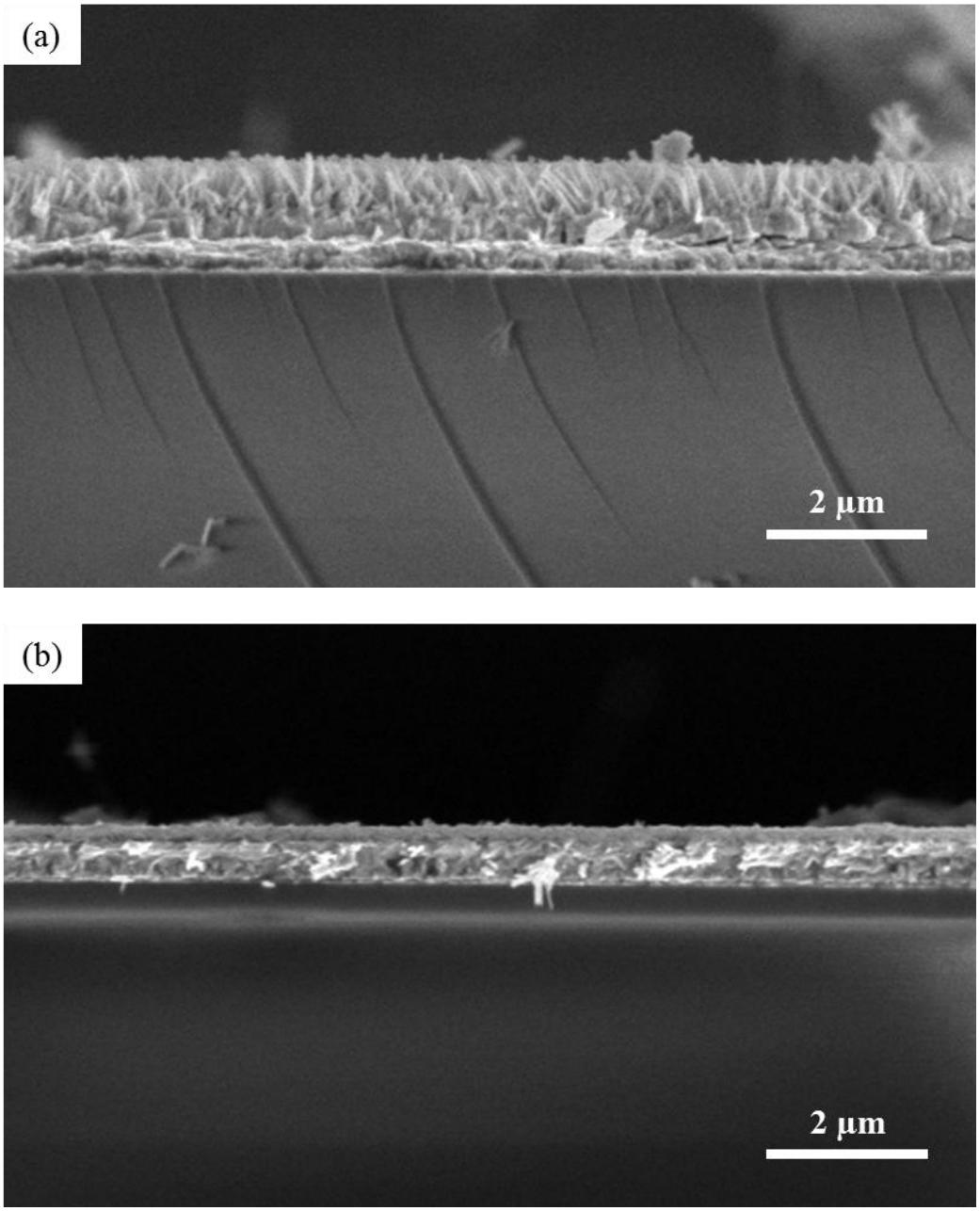

Figure 3.11. Cross-sectional SEM image of ZnO synthesized with traditional bowl-shaped boat; (a) near the edge to the precursor boat; (b) at center

The SEM images of synthesized ZnO with test tube-shaped precursor boat are shown in Figure 3.12 and 3.13. By using the test tube-shaped precursor boat, the ZnO was synthesized under synthesis conditions were the supply of zinc vapor reactant is maintained,

creating a stable environment. Although the uniformity of synthesized ZnO on the substrate is better, it is not perfect. The amount of synthesized ZnO is significantly higher in comparison to the synthesis with a bowl-shaped boat. Average diameter of 1-dimensional ZnO is about 440 nm near the edge and decreases over the length of the substrate down to 120 nm. The average length near the closest edge is about 3.6 μm, and 1.2μm at center.

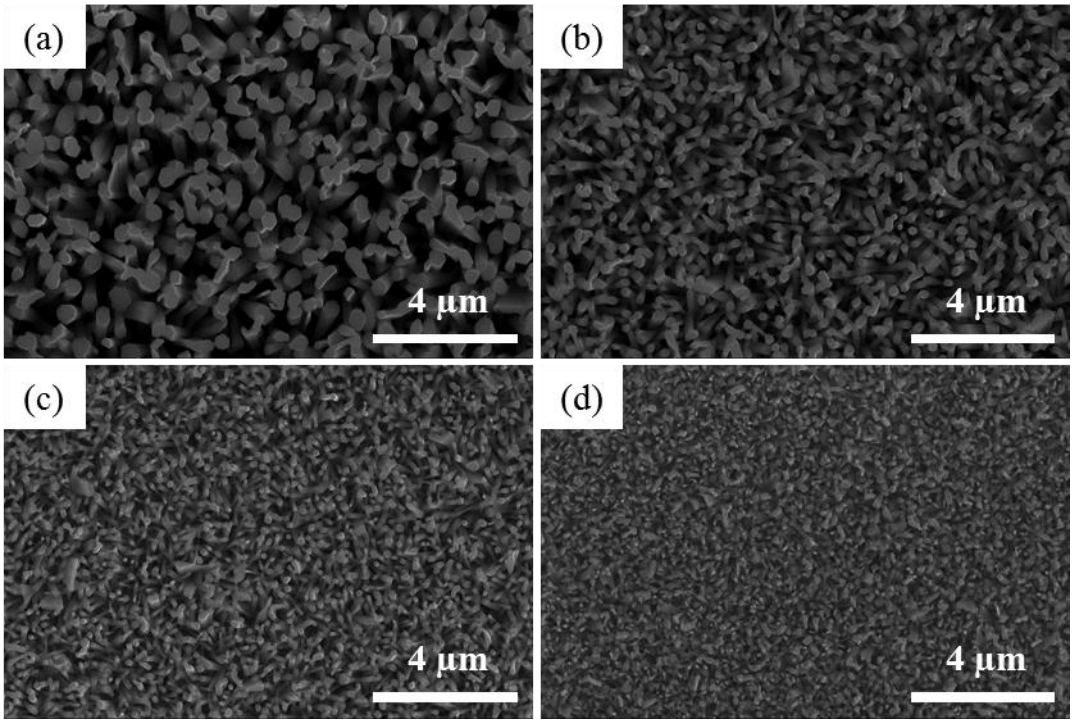

Figure 3.12. Surface SEM image of ZnO synthesized with test tube-shaped boat; (a) near the edge close to the precursor boat; (b) 0.5, (c) 1.0, (d) 1.5 cm away from the edge.

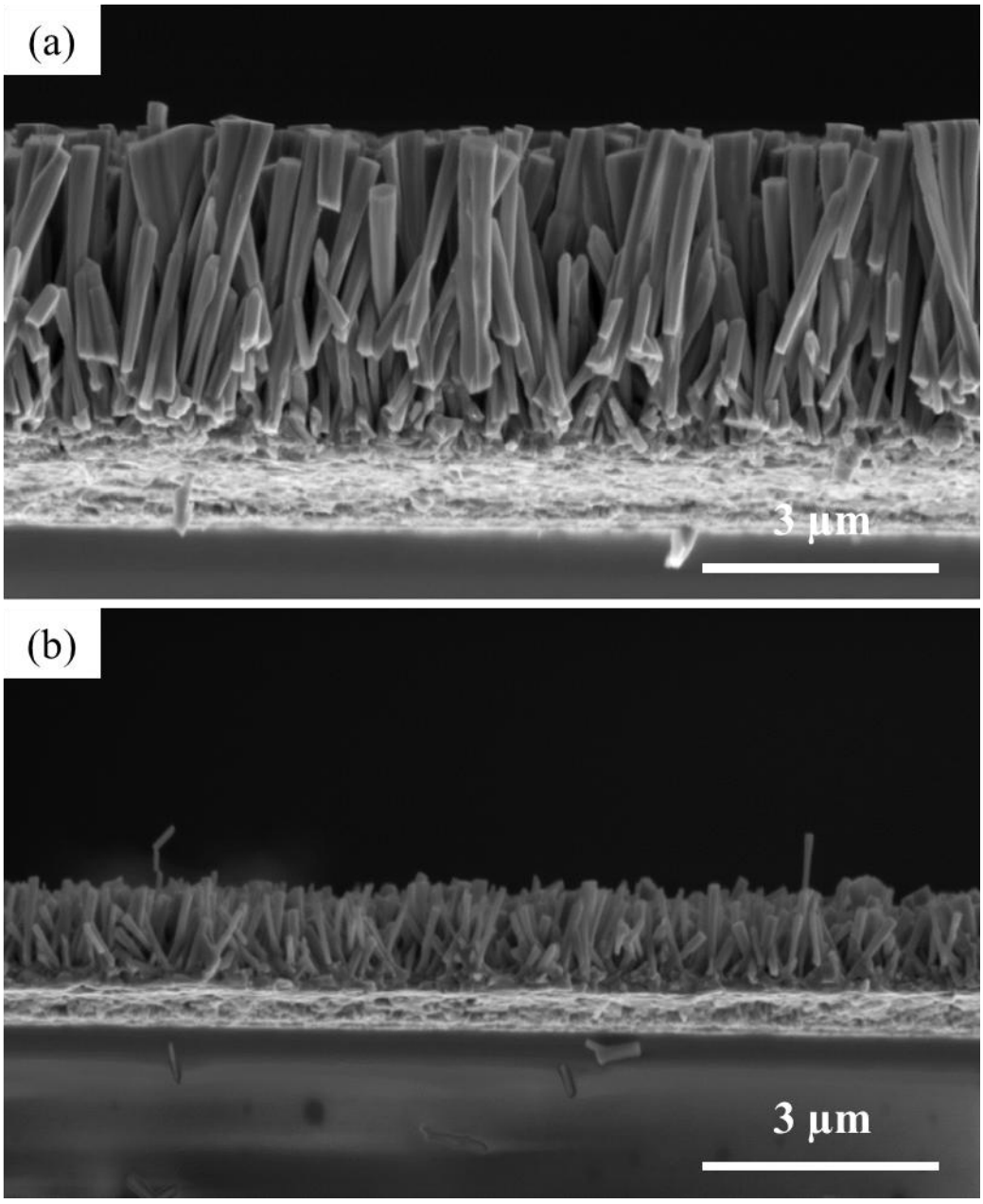

Figure 3.13. Cross-sectional SEM image of ZnO synthesized with test tube-shaped boat; (a) near the edge to the precursor boat; (b) at center

The crystal structure and crystallinity is characterized by XRD pattern analysis. The XRD results are shown in Figure 3.14. The peaks from ZnO among all the peaks are 34.47°, 36.29°, and 47.59°, and they correspond to (002), (101), and (102) lattice plane,

respectively. The other lattice planes in wurtzite ZnO do not show significant peak in the XRD analysis because the synthesized ZnO was highly ordered crystal grown along c-axis. The peaks from the substrate shows similar intensity on both samples but the peaks from ZnO shows higher intensity in the sample synthesized with test tube-shaped boat. Particularly, the peak found at 34.47° corresponding to (002) lattice plane shows a noticeable difference, so it is confirmed that the synthesis with the test tube-shaped boat strongly affects the 1-dimensional growth of ZnO.

The photovoltaic I-V characteristics of DSSCs using synthesized ZnO as aphotoelectrode are shown in Figure 3.15. The device using ZnO synthesized with bowl-shaped boat shows slightly higher open circuit voltage. However, the device with test tube boat ZnO has much higher current and fill factor, so the overall photovoltaic efficiency of the device with ZnO synthesized with test tube-shaped boat (0.060%) is higher than that with bowl-shaped boat (0.038%). The other characteristics are as listed in Table 3.1.

Table 3.1. Photovoltaic characteristics of DSSC with synthesized ZnO.

Precursor boat	**Bowl boat**	**Test tube boat**
V_{oc} (V)	0.60	0.57
J_{sc} (mA/cm^2)	0.19	0.29
Fill factor	0.33	0.36
Efficiency (%)	0.038	0.060

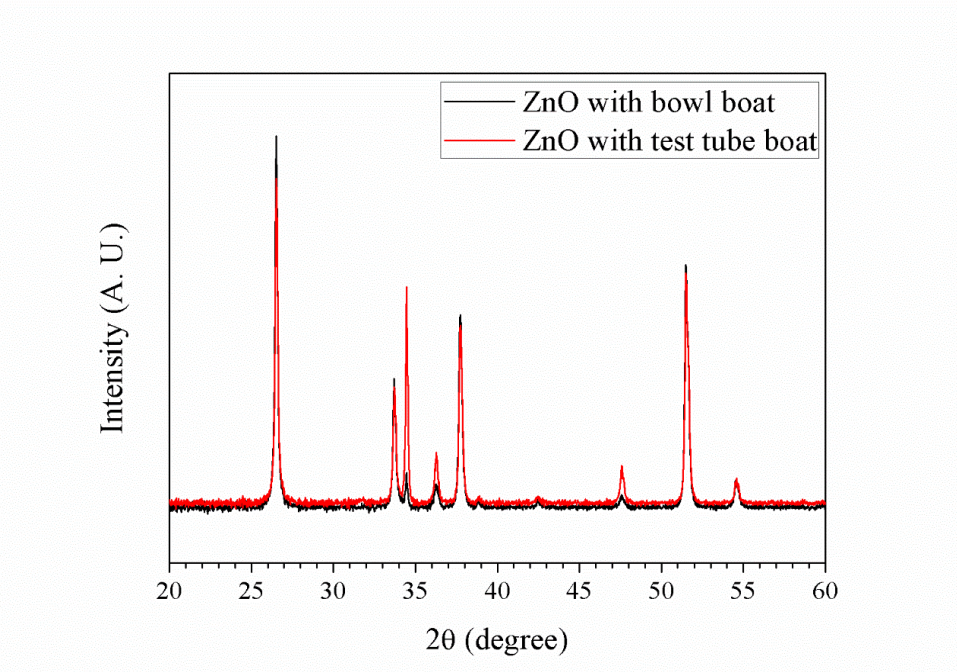

Figure 3.14. XRD pattern of synthesized ZnO with bowl and test tube-shaped boat.

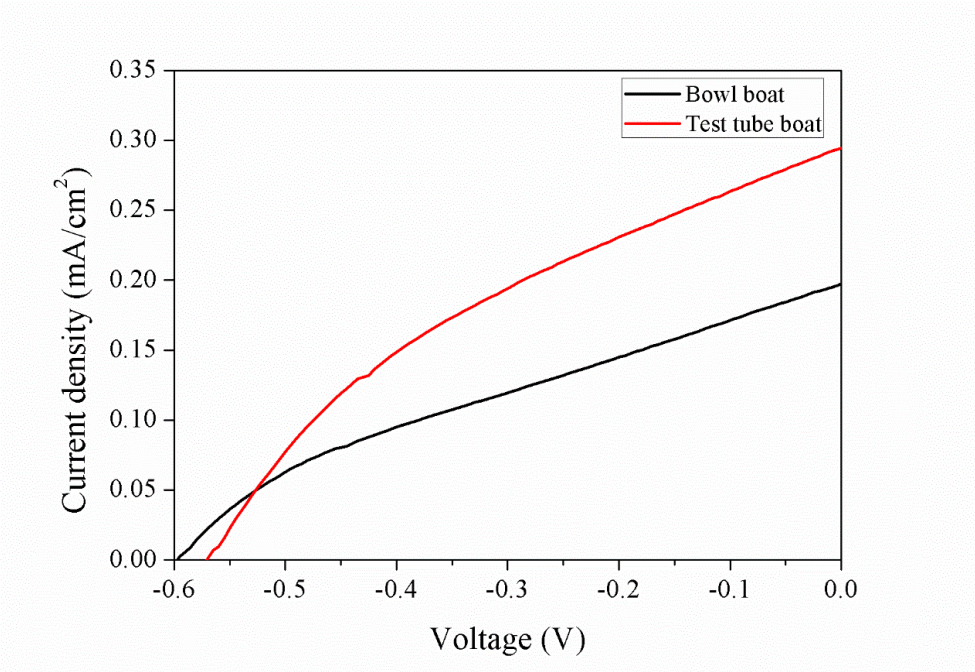

Figure 3.15. Photovoltaic characteristics of DSSCs using synthesized ZnO with bowl and test tube boat.

The improved current density in the photoelectrode using ZnO from the test tube-shaped boat is due to the larger surface area. The volume and quantity of the photoelectrode material in the two different devices is quite different, and correspondingly the number of adsorbed sensitizer molecules are very different as well. Therefore, the amount of absorbed light and the generated current are expected to be higher in the photoelectrode with larger surface area than the photoelectrode with a smaller surface area. In addition, the surface coverage on the FTO substrate is higher in the photoelectrode synthesized with the test tube-shaped boat, that the recombination at the interface of the FTO is reduced, improving the fill factor of these DSSC devices.

3.4. Conclusion

In conclusion, high quality ZnO is successfully synthesized under relatively low temperature environment using a test tube-shaped precursor boat to prevent premature oxidation of the precursor. Under the same temperature, in comparison to the ZnO synthesis using traditional bowl-shaped boat, the amount of product, crystallinity, and 1-dimensional growth preference for the ZnO synthesized using the test tube-shaped precursor boat, are significantly superior. Using a test tube-shaped precursor boat made the CVD synthesis of ZnO more controllable, and the low temperature process achieved by this method provides an opportunity for the synthesis of ZnO on stretchable or flexible devices which are sensitive to the processing temperature. The synthesized ZnO using a test tube-shaped precursor boat is successfully applied as the photoelectrode in DSSCs, and it shows higher photovoltaic efficiency than the ZnO synthesized with bowl-shaped boat.

References

[1] X. Xue, W. Zang, P. Deng, Q. Wang, L. Xing, Y. Zhang, Z. L. Wang, *Nano Energy*, **13**, 414-422 (2015)

[2] J.D. Chen, W.S. Liao, Y. Jiang, D.N. Yu, M.L. Zou, H. Zhu, M. Zhang, and M.L. Du, *Nanomater. Nanotechonl.*, **6**, 9 (2016)

[3] L. Wang, C. Ma, X. Ru, Z. Guo, D. Wu, S. Zhang, G. Yu, Y. Hu, and J. Wang, *J. Alloy. Compd.*, **647**, 57-62 (2015)

[4] X.-F. Wang, Y. Koyama, O. Kitao, Y. Wada, S.-I. Sasaki, H. Tamiaki, and H. Zhou, *Biosens. Bioelectron.*, **25**, 1970-1976 (2010)

[5] B.-Q. Liu, X.-P. Zhao, and W. Luo, *Dyes Pigments*, **76**, 327-331 (2008)

[6] J. Hu, and R. G. Gordon, *J. Appl. Phys.*, **72**, 5381-5392 (1992)

[7] M. J. Assael, I. J. Armyra, J. Brillo, S. V. Stankus, J. Wu, and W. A. Wakeham, *J. Phys. Chem. Ref. Data*, **41**, 033101 (2012)

[8] S.–S. Wang, H. Kawauchi, T. Kashima, H. Arakawa, *Coordin. Chem. Rev.*, **248**, 1381-1389 (2004)

[9] H. Wan, and H. E. Ruda, *J. Mater. Sci-Mater. El.*, **21**, 1014-1019 (201)

[10] Z. Zhang, H. Yuan, J. Zhou, D. Liu, S. Luo, Y. Miao, Y. Gao, J. Wang, L. Liu, L. Song, Y. Xiang, X. Zhao, W. Zhou, and S. Xie, *J. Phys. Chem. B*, **110**, 8566-8569 (2006)

[11] Y. Yan, L. Zhou, L. Yu, and Y. Zhang, *Appl. Phys. A*, **93**, 457-465 (2008)

Chapter 4.

Low-Temperature CVD Synthesis of Vertically Aligned ZnO with Gradated Morphologies and Physical Dimensions.

4.1. Introduction

Zinc oxide (ZnO) is known as a versatile material, and the synthesis, characterization, and fabrication of devices based on ZnO structures is a research topic that has attracted a lot of attention by researchers for decades. Like most of the II-VI semiconductors, ZnO has a hexagonal wurtzite crystal structure because it is stable at atmospheric pressure and room temperature. The wurtzite crystal structure in comparison to zinc blende, a polytype of wurtzite, crystal structure is shown in Figure 4.1[1]. In contrast to the zinc blende which is based on cubic closest packing (CCP) having a stack sequence of ABCABC, wurtzite structure is based on hexagonal closest packing (HCP) with stack sequence of ABAB. The anions construct the structure of HCP, and there are 12 tetrahedral site generated from the HCP structure. Half of the 12 tetrahedral sites are filled with 6 cations.

The lattice of wurtzite has an anisotropic nature because it has a c-axis parallel to z-axis and 2 axes on the x-y plane perpendicular to the c-axis, a_1 and a_2. Different surface activities induce the anisotropic crystal growth. In the thermodynamic equilibrium state, high surface energy facet has smaller surface area, and the low surface energy facet has larger surface area. In the case of wurtzite ZnO, due to the surface energy of the plane

perpendicular to the c-axis, so it is easier to grow in quasi 1-dimensional structure [2]. This trend can be adjusted by controlling the conditions of the kinetic reaction.

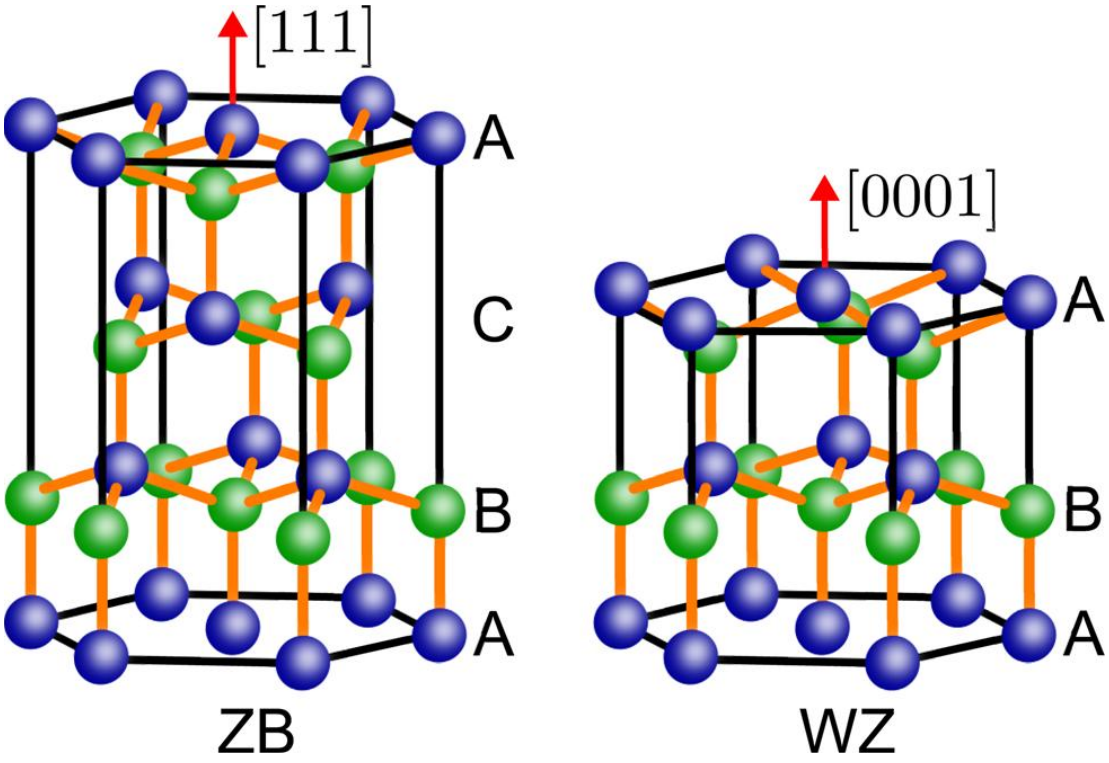

Figure 4.1. Zinc blende and wurtizite crystal structures and their stacking sequence.

ZnO is a semiconducting material with a wide bandgap of 3.37 eV and the band structure as shown in Figure 4.2 [3]. The valence band (VB) and conduction band (CB) form a bandgap without momentum change at the gamma point, so it has direct bandgap characteristics. The II-VI group semiconductor compounds having wurtzite crystal structure such as CdS, CdSe, ZnS, and ZnO tend to have direct bandgap characteristics, it makes the materials prime candidate for optoelectronic devices including blue and ultraviolet (UV) light-emitting diodes (LED) and lasers.

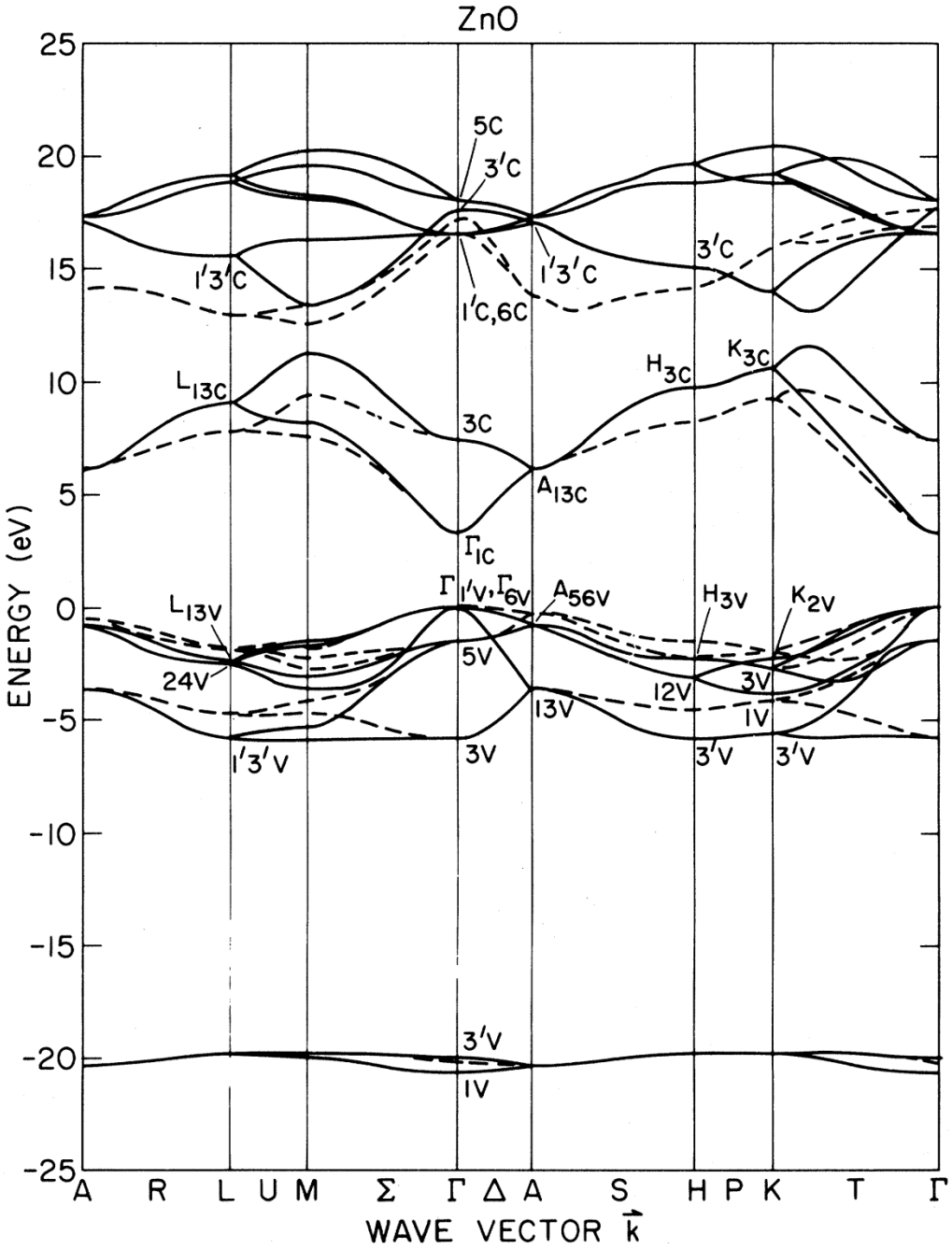

Figure 4.2. Band structure of ZnO

Silicon (Si), a representative indirect bandgap semiconductor, is widely used for photovoltaic devices but the interaction between light and the material is not fast nor

efficient. In the indirect bandgap materials, the electron transition between VB and CB is accompanied by a momentum change such as phonon vibration. Therefore, light absorption and emission of the material is slower than the direct bandgap materials. The silicon photovoltaic device is fabricated with a thickness of hundreds of μm because of those reasons. In contrast, advantages of direct bandgap materials are that the light absorption and emission is fast, interacting with light at a higher efficiency even in the thin film form. Therefore, semiconducting materials with a direct bandgap are used for thin-film photovoltaic devices.

Most wurtzite materials have naturally n-type semiconducting characteristics. ZnO also has n-type semiconductor behavior without the external treatment such as doping, and is known that the p-type doping is difficult. A mechanism called self-compensation is known as a reason of resistivity to the p-type doping [4]. The acceptor-like behavior is achieved by p-type doping but it is spontaneously compensated by generated donor defects such as vacancies or interstitials. The formation energies of n-type and p-type point defects are listed in Table 4.1 [5]. Oxygen vacancy (V_o) and zinc interstitial (Zn_i) are thermodynamically stable due to having negative formation energy, they exist in the natural ZnO to improve its stability. Therefore, the n-type characteristics are generated autonomously.

Table 4.1. Defect formation energy (in eV) of ZnO

Defect	n_a	q	ΔE_{LDA}	$\Delta E_{\mathrm{LDA\text{-}corr}}$
		Donorlike defects		
V_{O}	−1	+2	−0.5	−3.0
		+1	0.8	1.5
		0	1.5	2.4
Zn_i	−1	+2	−0.2	−2.3
		+1	1.5	2.1
		0	3.4	6.2
$\mathrm{Zn_O}$	−2	+2	0.2	0.4
		+1	2.0	5.2
		0	4.1	9.6
		Acceptorlike defects		
V_{Zn}	+1	0	5.8	10.6
		−1	5.7	10.1
		−2	5.8	10.1
O_i	+1	0	6.2	9.7
		−1	6.4	10.4
		−2	7.4	12.1

By the naturally generated defects, ZnO can have illuminative characteristics. Various form of defects such as V_o [6], O_{Zn} [7], and donor-acceptor pairs are explained as reasons of luminescence in the literature, but it is still controversial and on debate. Diverse transitions are proposed to be the reasons of assorted colored emission generated by ZnO depending on the wavelength or energy level. The calculated defect's level in ZnO film is as shown in Figure 4.3 [8].

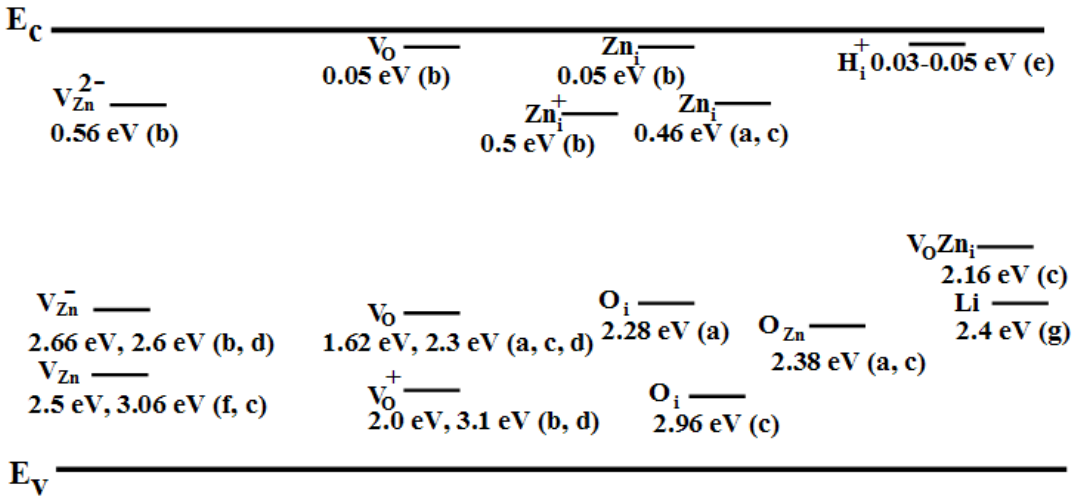

Figure 4.3. Calculated defect's levels in ZnO film

The origins of diverse colored emission that can be generated by ZnO are suggested as various electron transition states and they are listed in Table 4.2 [9, 10].

Table 4.2. Proposed transition in ZnO depending on the emission color

Emission color	Proposed transition
Orange	CB to O_i [9]
Yellow	Zn_i to O_i [10]
Green	CB to V_o [9]
Blue	Zn_i to V_{Zn} [9]
Purple	Zn_i to VB [9]

Besides the interaction between ZnO crystal and light, the interaction with phonons is also important. A phonon is a quasiparticle in the form of a vibration, which affects the

heat conductance, specific heat capacity, and electrical conductivity in solid matter. Wurtzite crystal has 4 atoms in a unit cell, so 9 vibrational modes are possible (Γ_{opt} = A_1+2B_1+E_1+2E_2) [11]. The schematic illustration is shown in Figure 4.4.

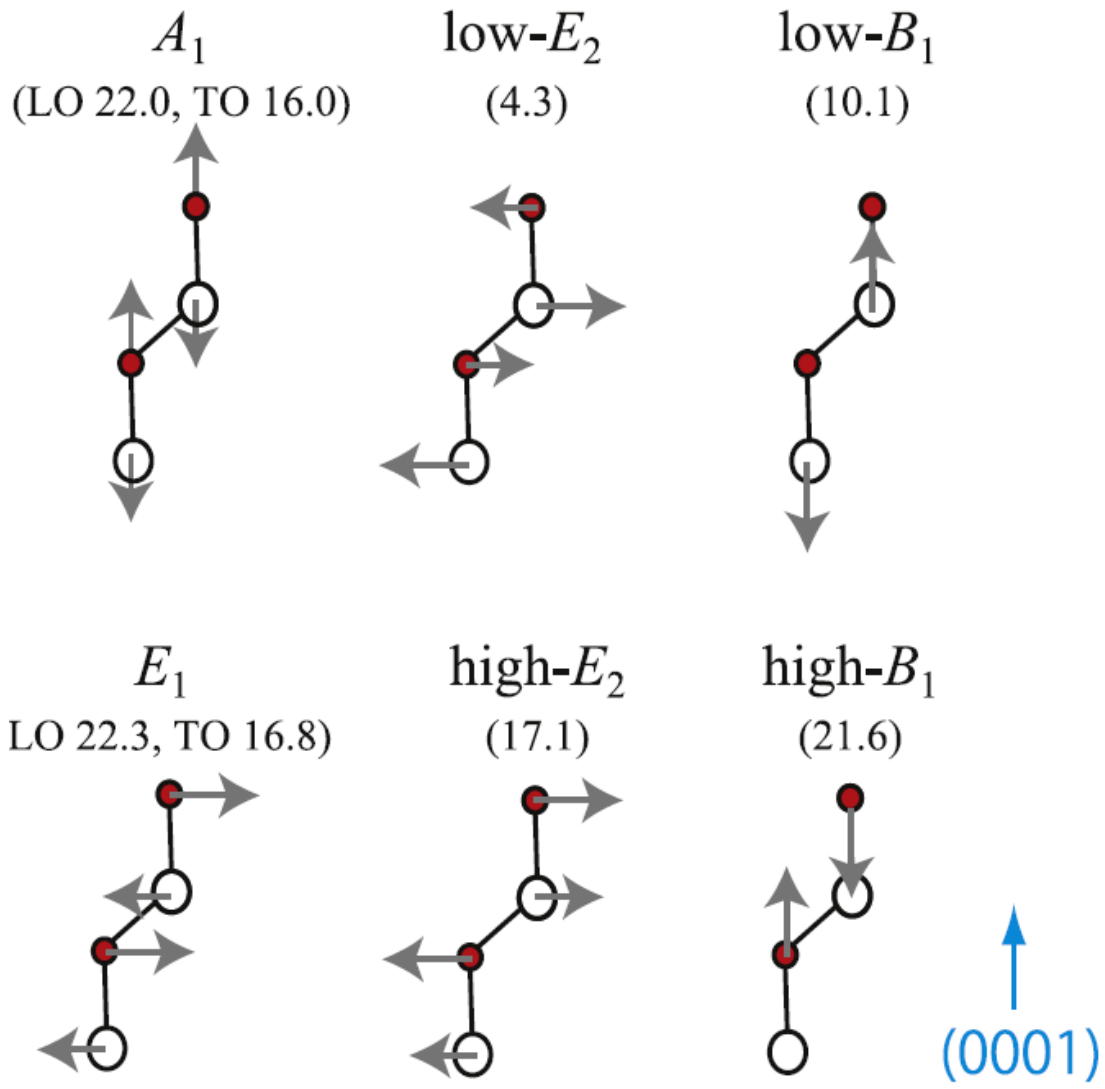

Figure 4.4. Atomic displacement in wurtzite crystal of the gamma-point phonon.

Each vibration mode can be detected by Raman spectroscopy or infrared (IR) spectroscopy. The typical Raman spectrum of wurtzite ZnO is as shown in Figure 4.5 [12].

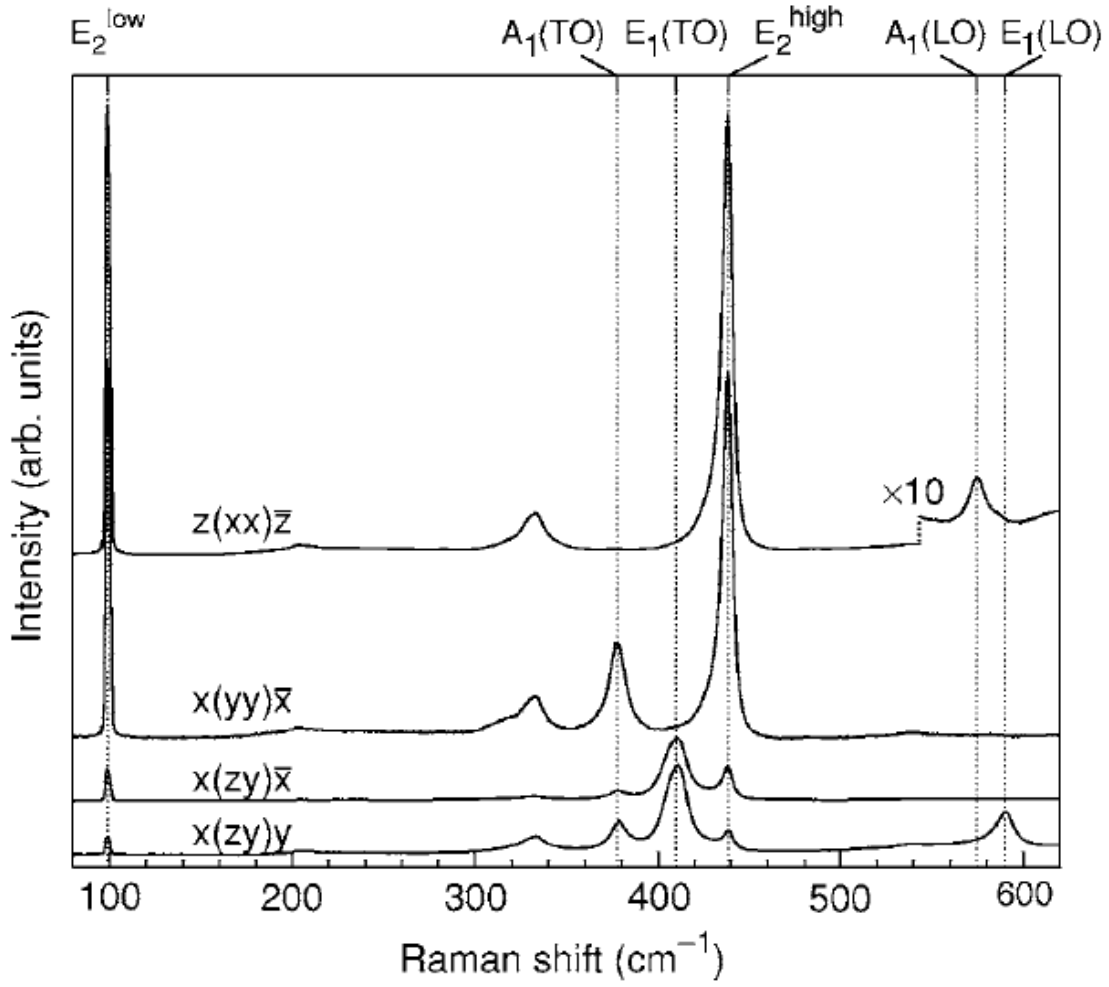

Figure 4.5. Raman spectra of ZnO

By Raman spectroscopy, properties of ZnO crystal can be characterized by analyzing the effects on the crystal structure and vibrational characteristics. Lattice dynamics can be researched by Raman spectroscopy.

In this chapter, the physical and optical characteristics of ZnO synthesized under low-temperature environment by LPCVD are discussed. The prevention of premature oxidation of Zn precursor technique was introduced in Chapter 3 to improve the reaction environment by controlling reaction kinetics and fluid dynamics. ZnO is synthesized under

lower temperature, and its structural and optical characteristics are analyzed by scanning electron microscopy (SEM), X-ray diffraction (XRD) analysis, Raman spectroscopy, and fluorescence spectroscopy.

4.2. Experimental procedure

The synthesis of ZnO was conducted in a 5 inches diameter quartz tube placed horizontally in a three-zone tube furnace, OTF-1200 from MTI. The zinc (Zn) powder and fluorine-doped tin oxide (FTO) are used as precursor and substrate, respectively. A 2 x 2 cm^2 sized FTO glass was cleaned by sonicating in detergent solution, acetone, 2-propanol for 15 minutes each. About 0.2 g Zn powder was put in a test-tube shaped precursor boat and placed in the tube furnace. The cleaned FTO substrate is placed at 1 cm away from the precursor boat (downstream). Nitrogen (the carrier gas), and oxygen (the oxidizer) are connected to the inlet of the quartz tube, and the outlet of the quartz tube is connected to a mechanical pump. The mass flow of nitrogen and oxygen is set 100 standard cubic centimeter square (SCCM) and 4 SCCM, respectively. After purging the quartz tube with the mixture of gas for 15 minutes, the furnace is heated to 450℃. The temperature is maintained for 60 minutes for the reaction to take place. The reaction is completed by cooling down the CVD furnace by natural convection.

The physical dimensions and morphology of synthesized ZnO was observed by scanning electron microscopy (SEM) with Nova NanoSEM 450 under the accelerating voltage of 5 kV with ETD. The sample for SEM characterization was prepared by mounted on the aluminum SEM pin holder fixed by carbon tape and grounded by silver paint. The

crystal structure and crystallinity is analyzed by X-ray diffraction (XRD) pattern analysis with Empyrean X-ray diffractometer under 45 kV and 40 mA operating condition. The sample for the XRD analysis was prepared by mounted on the XRD specimen holder fixed with clay. The phonon vibration was observed by Raman spectroscopy with Horiba LabRAM integrated with AIST-NT scanning probe microscope (SPM). The green fluorescence emission was characterized by Horiba Fluorolog FL3-22 spectrophotometer in solution state.

4.3. Results and discussion

Figure 4.6 shows the photograph of the synthesized ZnO on the FTO substrate. During synthesis the top end of the substrate is oriented toward the precursor boat. From the location of the precursor boat, a radial gradation pattern is formed and can be easily observed by the naked eye. This result shows that the synthesis of ZnO material is strongly dependent on the distance from the precursor boat.

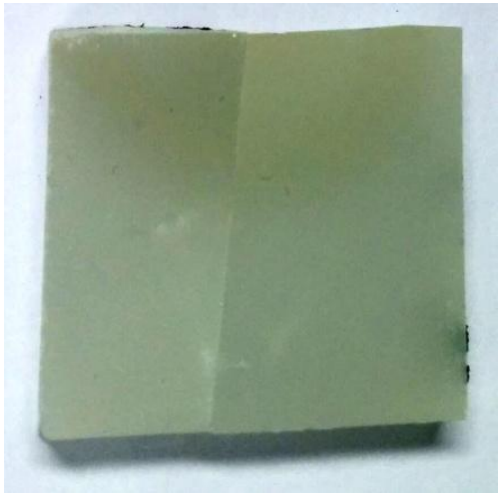

Figure 4.6. Photo of synthesized ZnO on FTO glass.

Since the test tube-shaped precursor boat was used, the Zn vapor reactant was supplied steadily even under the low temperature environment. The reaction temperature of 450℃ is about 30℃ higher than melting point of Zn, and the evaporation rate cannot be expected to be high under low vacuum conditions. Therefore, the partial pressure generated by Zn vapor is expected to be significantly low in comparison to the partial pressure of oxygen. The Zn vapor reactant is rapidly oxidized by the excessive oxygen gas to form ZnO, and it is expected that the partial pressure of Zn vapor will decreased drastically as the distance away from the precursor boat increases. From the edge closest to the precursor boat, SEM images are taken in 2 mm increments. The SEM images taken in the closer area (~4 mm) are shown in Figure 4.7. In this region, the morphology of ZnO is observed as a mixture of needles form and irregular rod form. The result observed in the cross-sectional image shows the ZnO forms a vertically aligned structure. The synthesized ZnO material in this region has a thin film layer (about 2~3 μm) at the bottom of ZnO layer. The thickness of the ZnO layer was measured as 8 um including FTO, ZnO film, and 1-dimensional ZnO.

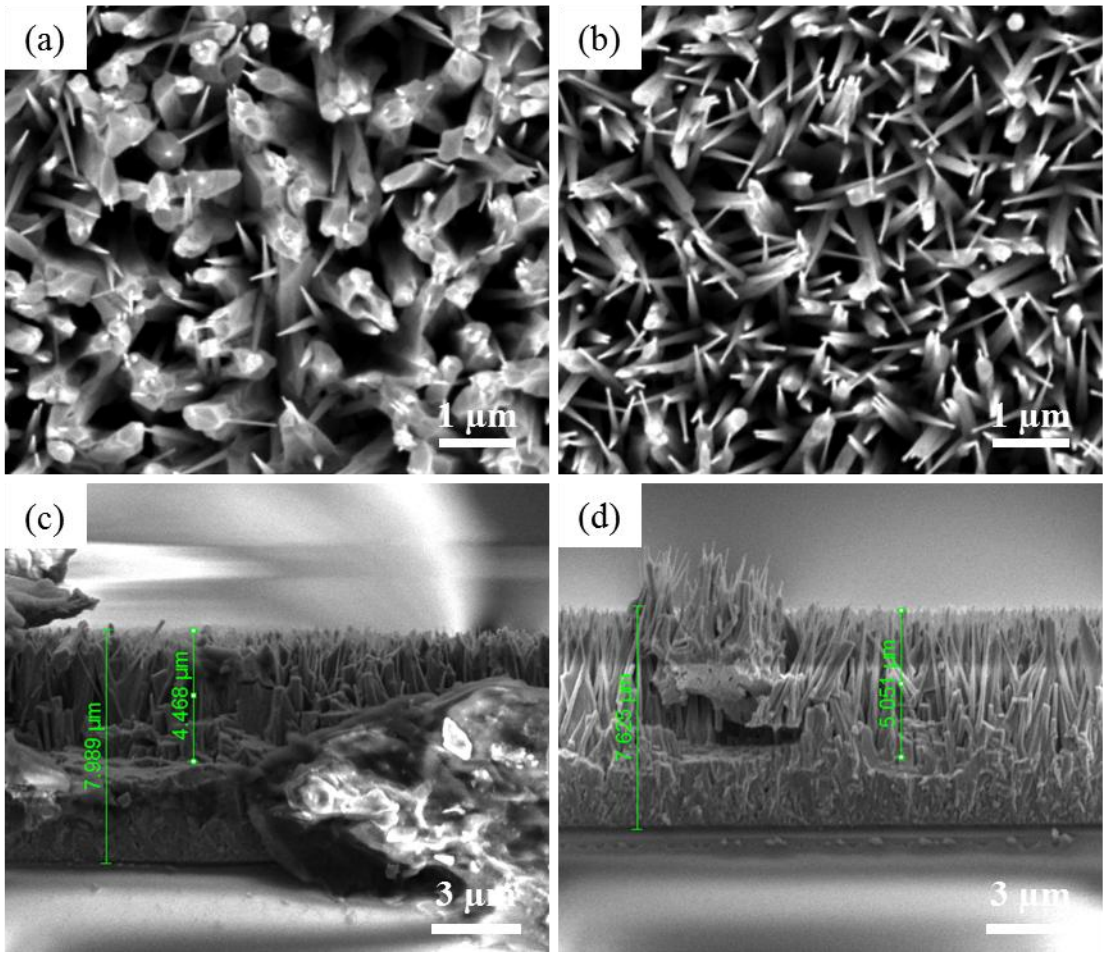

Figure 4.7. Synthesized ZnO at area closest (2~4 mm) to the precursor boat; (a) surface image at 2 mm from edge; (b) surface image at 4 mm from edge; (c) cross-sectional image at 2 mm from edge; (d) cross-sectional image at 4 mm from edge.

The surface and cross-sectional SEM images of ZnO synthesized in the middle region (6~8 mm) are shown in Figure 4.8. The ZnO observed in the surface images have significantly better regularity in comparison to the closer area, and the thin film layer at the bottom is thinner. Two different positions in this region have noticeable differences. ZnO with three times a larger diameter is synthesized at a 2 mm distance. Because the length of the synthesized ZnO is the longest in this region, it is expected that the ratio of Zn and oxygen reactant is close to ideal condition. This region is near the interface of the

semicircular pattern in the photo. It is assumed that the ratio of Zn and oxygen is inversed at this point. The synthesized ZnO in farthest location is shown in Figure 4.9.

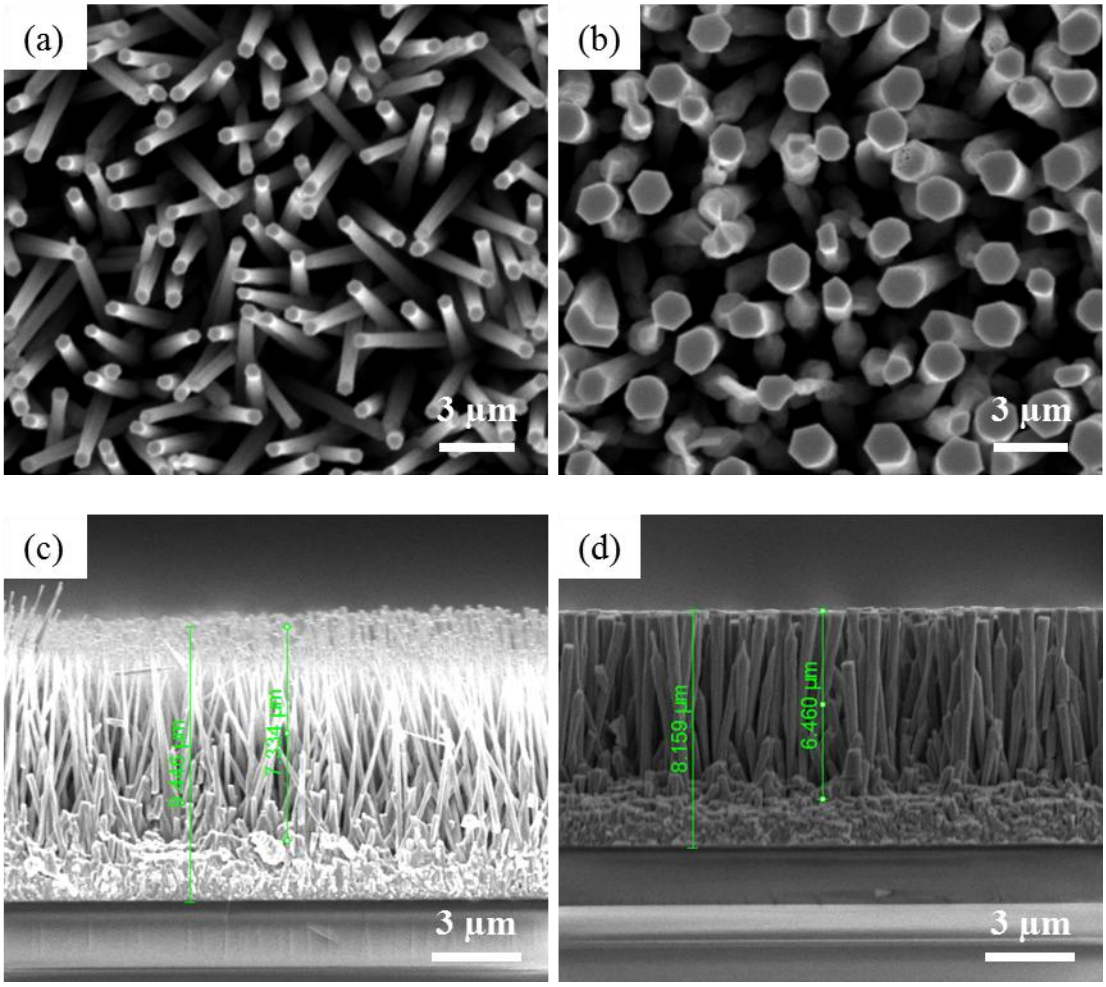

Figure 4.8. Synthesized ZnO at middle distance area (6~8 mm); (a) surface image at 6 mm from edge; (b) surface image at 8 mm from edge; (c) cross-sectional image at 6 mm from edge; (d) cross-sectional image at 8 mm from edge.

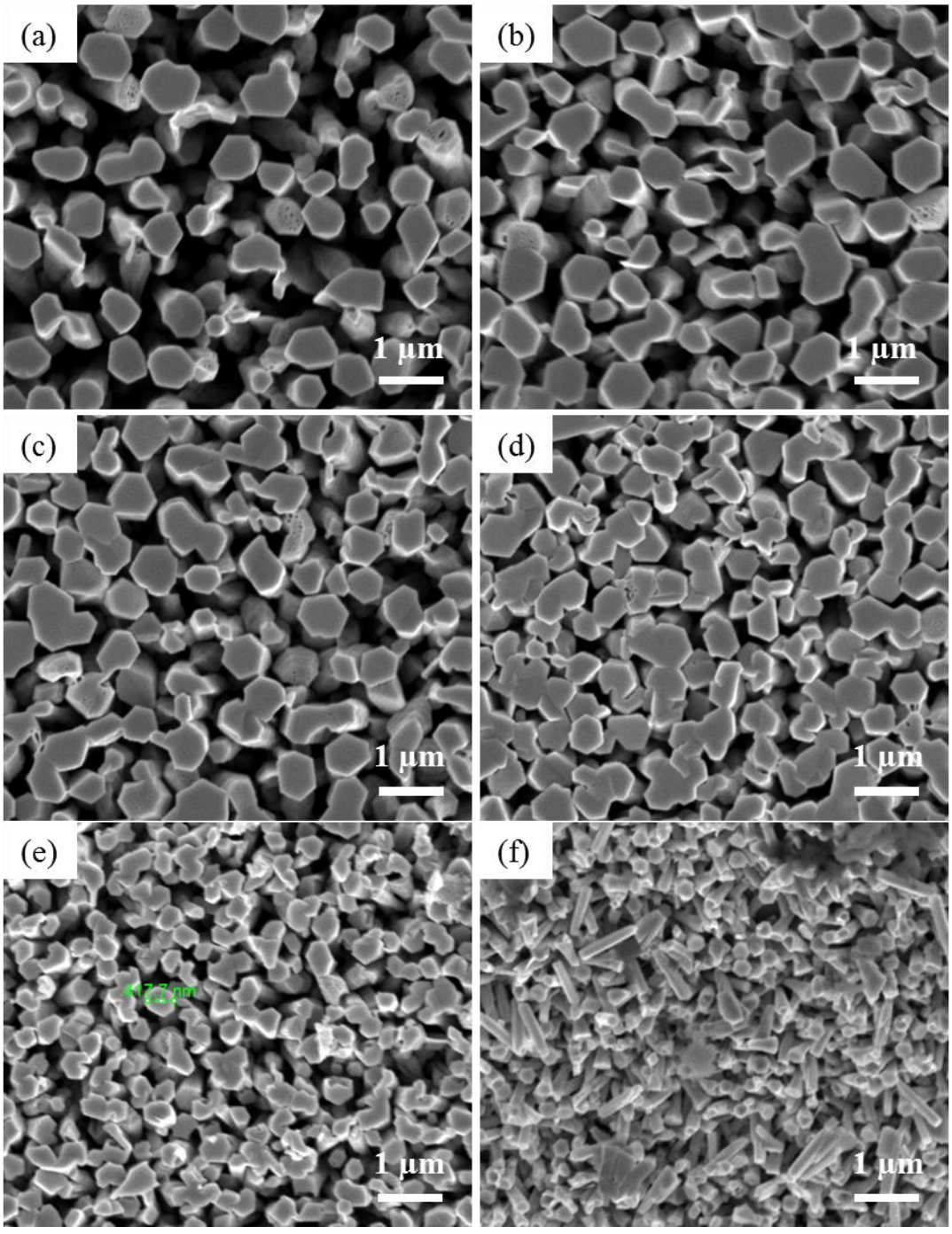

Figure 4.9. Synthesized ZnO at far distance area (10~20mm); (a) 10 mm; (b) 12 mm; (c) 14 mm; (d) 16 mm; (e) 18 mm; (f) 20 mm from edge.

The ZnO synthesized in the farthest area has 1-dimensional structures, but their aspect ratio are very low and in the form of irregular hexagonal pillar. This result shows that the directional preferred growth and thermodynamic stability under low temperature and low Zn partial vapor pressure have a competitive relationship. As the distance increases, the growth of ZnO crystal is not preferred along the c-axis anymore. Rather it grows in a way to increase the diameter of hexagonal pillar and the filling factor of ZnO layer is significantly decreased. The thickness of ZnO (including FTO) layer with respect to increasing distance away from the precursor boat is shown in Figure 4.10.

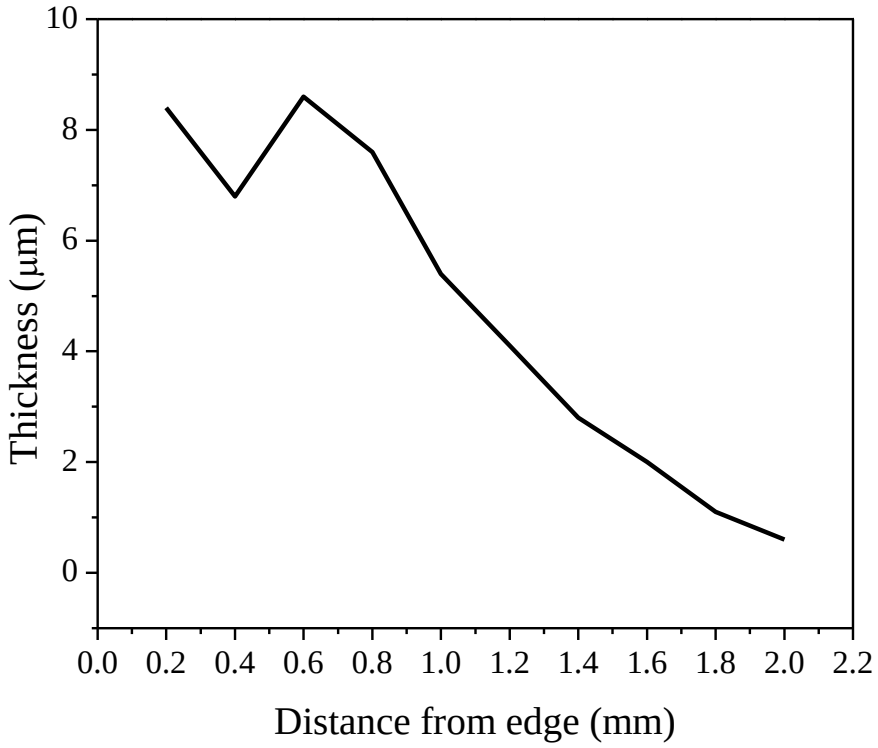

Figure 4.10. Thickness of ZnO layer depending on the distance.

The XRD pattern analysis is shown in Figure 4.11. The y-axis is displayed in log scale to see the details of all peaks. The peaks found at 2θ are 31.09, 34.50, 36.29, 47.61, and 62.92 which correspond to (100), (002), (101), (102), and (103) lattice plane, respectively. The results show that the synthesized ZnO has a hexagonal wurtzite structure with high crystallinity. There is a dominant peak at 34.50° corresponding to (002) lattice plane, which indicates that the synthesized ZnO has a strong preferential crystal growth normal to the (002) plane, that is along c-axis. The other peaks from (100), (101), (102), and (103) lattice plane show relatively low intensity.

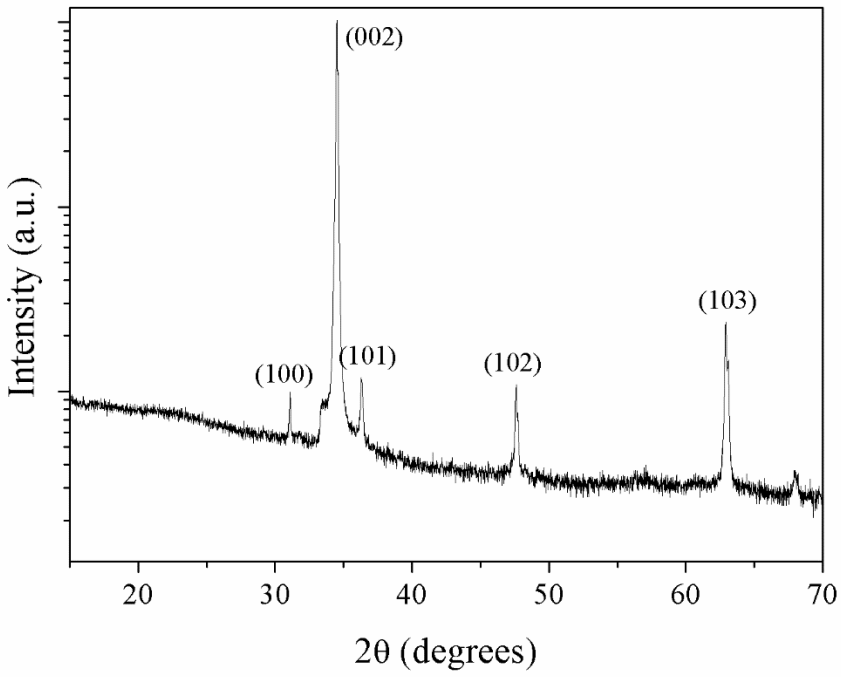

Figure 4.11. XRD result of synthesized ZnO.

Raman spectroscopy, shows the existence of oxygen vacancies by the detection of a peak at 580 cm^{-1}. The slight peak intensity at 580 cm^{-1}, at the substrate position of 4 mm

was found while the other substrate positions (8 mm, 12 mm) do not show any peaks at the point. In the literature [13], it has been shown that the peak at 580 cm^{-1} is observed when there are oxygen vacancies in the ZnO crystals. The Raman spectroscopy results support the assumption that the closer area is in a Zn excessive environment during the reaction, and Zn vapor decreases as the distance from the precursor boat increases.

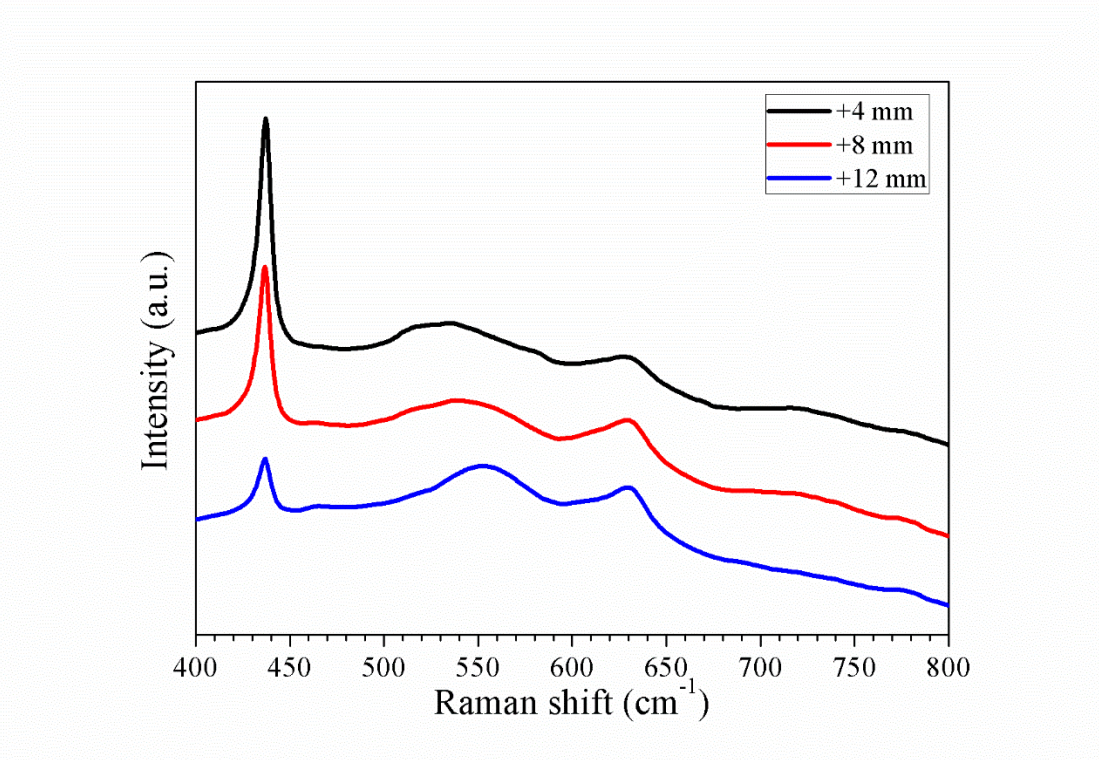

Figure 4.12. Raman spectra measured at different position of the substrate.

The fluorescence emission of the synthesized ZnO was observed by a fluorometer as shown in Figure 4.13. The synthesized ZnO absorbs light at 366 nm and emits fluorescence at 498 nm wavelength. The absorption wavelength at 366 nm is converted to 3.38 eV, which means the absorption is a band-edge absorption because the energy level

is similar to the bandgap energy of wurtzite ZnO. The origin of green emission at 498 nm or 2.49 eV is due to the transition from deep donor level by oxygen vacancies to VB [14].

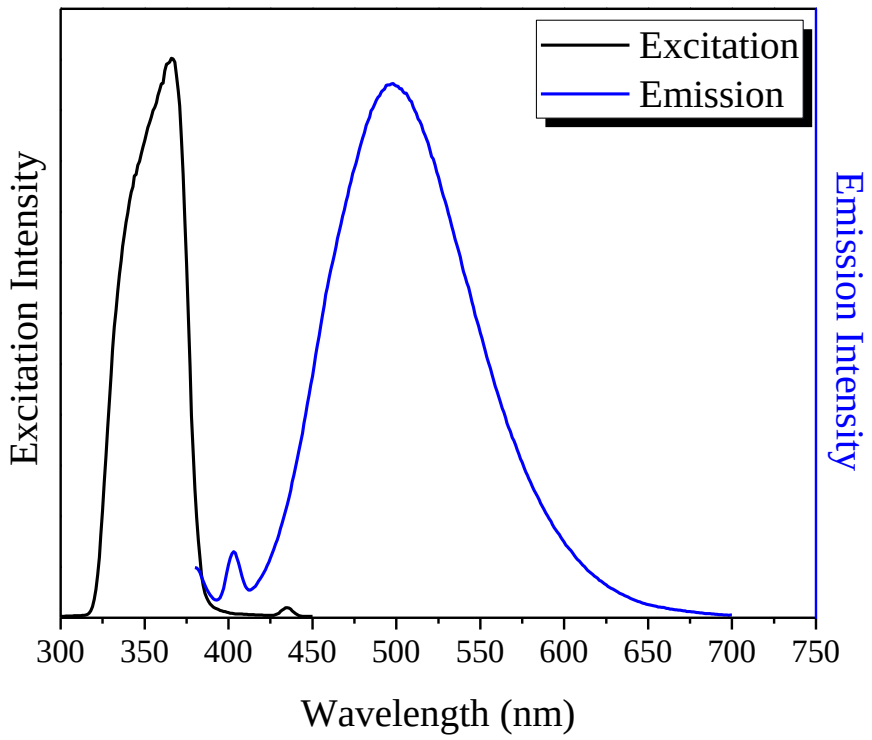

Figure 4.13. Fluorescence emission and excitation spectra of synthesized ZnO.

4.4. Conclusion

In this chapter, the low-temperature synthesis of ZnO is conducted through LPCVD method by preventing the premature oxidation of precursor. The product has a gradational morphology and physical dimensions that change as the distance away for the precursor boat increases. The XRD results show that the synthesized ZnO has a preferred directional crystal growth along the c-axis, which drives the formation of 1-dimensional structures. The synthesized ZnO emits green fluorescence light following band-edge absorption.

References

[1] P. E. Faria Junior, and G. M. Sipahi, *J. Appl. Phys.*, **112**, 103716 (2012)

[2] J. Zhan, H. Dong, S. Sun, X. Ren, J. Liu, Z. Chen, C. Lienau, and L. Zhang, *Adv. Optical Mater.*, **4**, 126-134 (2016)

[3] A. Kobayashi, O. F. Sankey, and J. D. Dow, *Phys. Rev. B*, **28**, 946-956 (1983)

[4] C. H. Park, S. B. Zhang, and S.-H. Wei, *Phys. Rev. B*, **66**, 073202 (2002)

[5] S. B. Zhang, S.-H. Wei, and A. Zunger, *Phys. Rev. B*, **63**, 075205 (2001)

[6] H. S. Kang, J. S. Kang, J. W. Kim, and S. Y. Lee, *J. Appl. Phys.*, **95**, 1246-1250 (2004)

[7] B. Lin, Z. Fu, and Y. Jia, *Appl. Phys. Lett.*, **79**, 943-945 (2001)

[8] M. Willander, O. Nur, J. R. Sadaf, M. I. Qadir, S. Zaman, A. Zainelabdin, N. Bano, and I. Hussain, *Materials*, **3**, 2643-2667 (2010)

[9] C. H. Ahn, Y. Y. Kim, D. C. Kim, S. K. Mohanta, and H. K. Cho, *J. Appl. Phys.*, **105**, 013502 (2009)

[10] X. L. Xu, G. G. Siu, C. L. Fu, and H. C. Ong, *Appl. Phys. Lett.*, **78**, 2285-2287 (2001)

[11] K. Ishioka, K. Kato, N. Ohashi, H. Haneda, M. Kitajima, and H. Petek, *J. Phys.: Condens. Matter*, **25**, 205404 (2013)

[12] R. Cuscó, E. Alarcón-Lladó, J. Ibáñez, L. Artús, J. Jiménez, B. Wang, and M. J. Callahan, *Phys. Rev. B*, **75**, 165202 (2007)

[13] X.Q. Wei, B.Y. Man, M. Liu, C.S. Xue, H.Z. Zhuang, and C. Yang, *Physica B*, **338**, 145-152 (2007)

[14] F. Lieter, H. Alves, D. Pfisterer, N.G. Romanov, D.M. Hofmann, and B.K. Meyer, *Physica B*, **340-342**, 201-204 (2003)

Chapter 5.

Template-Free Self-Catalyzed Ultra-Thin ZnO Nanowire Crystal Growth.

5.1. Introduction

Quasi-1-dimensional nanowires such as carbon nanowires, silicon nanowires, zinc oxide (ZnO) nanowires show significantly different characteristics from the bulk state due to quantum confinement effect and extremely high surface-to-volume ratio. As the dimension of the material from the 3-dimensional bulk material to 0-dimensional quantum dots, the movement and behavior of the charge carriers is spatially constrained. The behavior of the charge carriers is controlled by quantum effects. By the quantum confinement effect, the energy state in the low-dimensioned material loses continuity and is discrete. To date, many parts of quantum behavior are still in need for further exploration. The schematic illustration of quantum confined density of states is shown in Figure 5.1 [1]. Semiconducting nanowires are used for a variety of electrical devices such as transistors, sensors, solar cells, and light-emitting diodes due to their unique electrical and optical characteristics. Besides quantum effects, it has been reported that semiconducting nanowires are used for applications that require large surface area such as gas sensors and solar cells due to their high surface-to-volume ratio. Nanowires in general have tremendous advantages for device miniaturization, and so are actively researched by the research community.

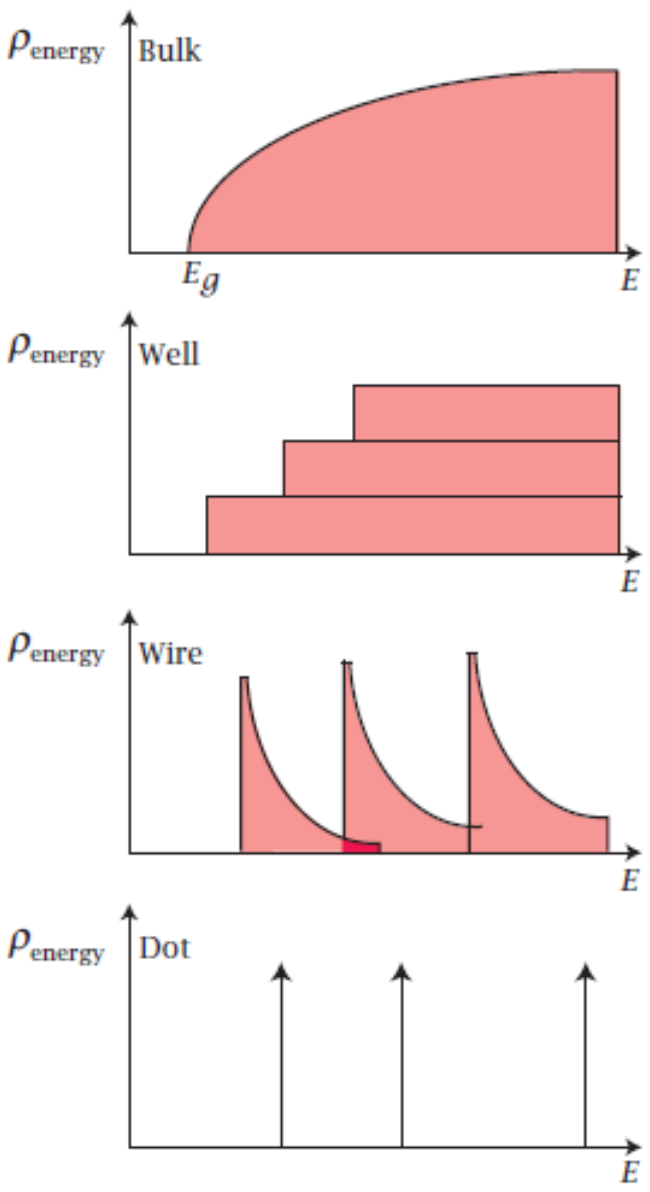

Figure 5.1. Density of states depending on the dimensions.

ZnO is a multifunctional semiconducting metal oxide material with 3.3 eV direct bandgap. Wurtzite crystal structure is stable under room temperature and atmospheric pressure, therefore most of the ZnO is in form of wurtzite crystal structure as shown in Figure 5.2 [2]. The wurtzite crystal structure has two lattice parameters, a and c, and a

hexagonal unit cell. Its ratio of $^{c}/_{a}$ is $^{8}/_{3}$ = 1.633a in the ideal case, and cations and anions form 4-coordination bonding to each other, forming tetrahedron sublattices. In reality and deviating for the ideal case, the location of the atoms in ZnO are slightly dislocated from the ideal arrangement by changing $^{c}/_{a}$ ratio and the location of inner atoms.

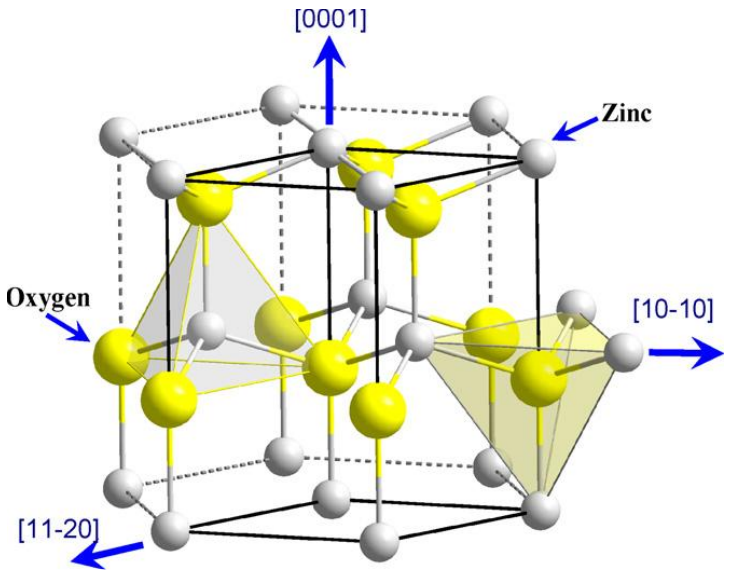

Figure 5.2. Crystal structure of wurtzite ZnO.

The wurtzite ZnO has a character of anisotropic crystal growth, so it can have 1-dimensional structure easily. Research on diverse devices using 1-dimensional ZnO have been widely reported and include transistors [3], light sensors [4], gas sensors [5], photoelectrodes [6], nanocantilevers [7], and nanolasers [8].

Another widely used II-VI group semiconducting material having the wurtzite crystal structure like ZnO is gallium nitride (GaN). GaN has a wide bandgap of 3.5 eV. It can easily interact with high energy light, it is widely used for blue light emission applications [9]. The physical, structural, and optical property of ZnO and GaN are similar,

so they are used as each other's counterpart, for heteroepitaxial growth (Figure 5.3 (a), [10]), or to form a hybrid structure and solid solution (Figure 5.3 (b), [11]). One advantage of ZnO vs. GaN is its cost-effectiveness due to the ease of 1-dimensional crystal growth, so it is widely researched as a potential substitute for GaN. A significant difference between ZnO and GaN is that the exciton binding energy of ZnO is high (59 meV), while GaN has a lower exciton binding energy (28 meV). The exciton binding energy of ZnO is about 2.4 times higher than the thermal energy in room temperature, $k_bT = 25\ meV$, so the near-band-edge excitonic emission on ZnO is possible.

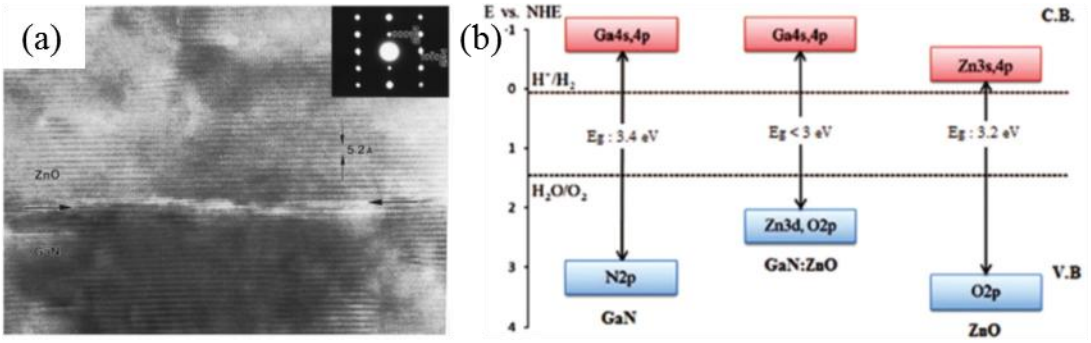

Figure 5.3. Hybrid of ZnO and GaN; (a) TEM image of heteroepitaxial growth; (b) band diagram of solid solution.

An exciton is a bounded state of an electron and a hole forced by Coulomb interaction, which acts like a quasiparticle. It affects the properties of optoelectronic devices such as photovoltaic cells and light emitting diodes. The electron-hole interaction is defined by the exciton binding energy, and this value can vary from a few meV to 100 meV, depending on the material. Even though two different materials may have a similar structure, their exciton binding energy can be quite different. Even though the crystal structure, lattice parameters, bandgap, end effective mass of GaN and ZnO are similar, they show significantly different exciton binding energies. Due to higher ionic characteristics

of ZnO, it could be expected by the simple tight-bonding model that ZnO has a lower exciton binding energy than GaN, but this is not the case. A relationship between exciton binding energy and exciton Bohr radius is described by the hydrogenic model as shown in Figure 5.4 [12].

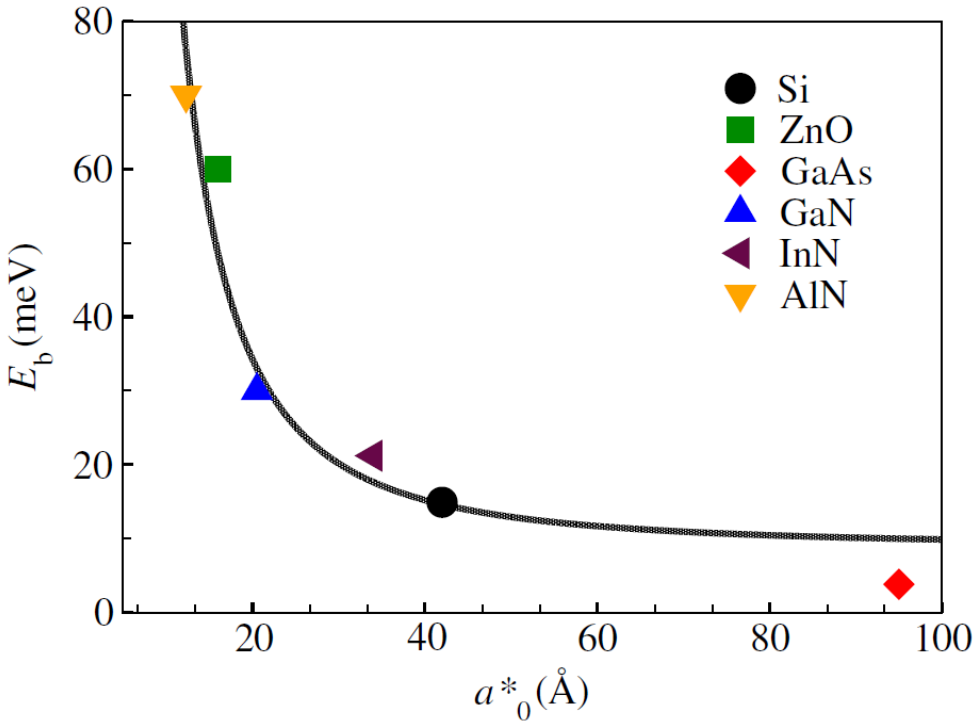

Figure 5.4. Calculated exciton binding energy (E_b) versus exciton Bohr radius.

During the crystal growth of ZnO, the surface atom is a factor to be seriously considered. 1-dimensional crystal growth of ZnO occurs along the c-axis, it is affected by the polarity of the (0001) surface depending on whether the terminal atom is Zn or oxygen. The crystal structure model of ZnO and crystal plane along c-axis is shown in Figure 5.5 (a) [13] and (b) [14], respectively.

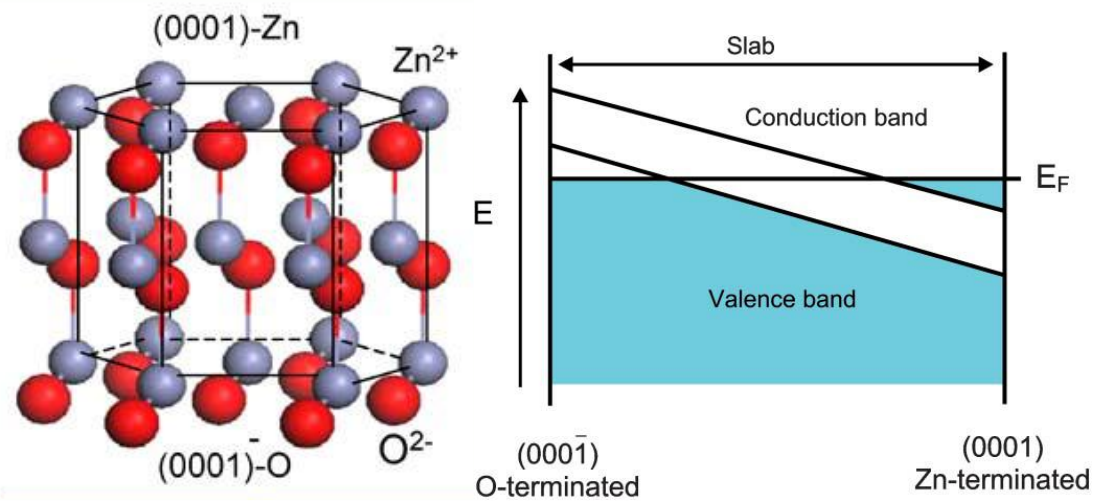

Figure 5.5. Crystal structure of wurtzite ZnO with different terminated (0001) plane.

Self-catalysis is a catalysis reaction without the need for an additional catalyst. In chemical vapor deposition (CVD), self-catalysis uses its product as the catalyst, so it is considered as vapor-liquid-solid (VLS) reaction. VLS reaction takes place after the migration of reactant to the preferred site after the adsorption of gas phase reactant. Therefore, the thermodynamic stability of the intermediate state of adsorbed reactant is a very important factor in the reaction. Diverse VLS synthesis to grow the 1-dimensional ZnO crystal have been reported [15,16].

In the VLS reaction with catalysts, the reason why surface atom species are important is illustrated in Figure 5.6[17]. When the ZnO nanowire are grown under the presence of a tin catalyst, the morphology of the product changes depending on the charges at the surface. The droplet of the reactant is formed in a more spherical shape to reduce the interfacial area due to Coulomb repulsion. Even the use of neutral tin as the catalyst, can have positively charged effect because the metal atoms tend to lose their electrons [18]. The surface charge plays a pivotal role in the self-catalysis as well.

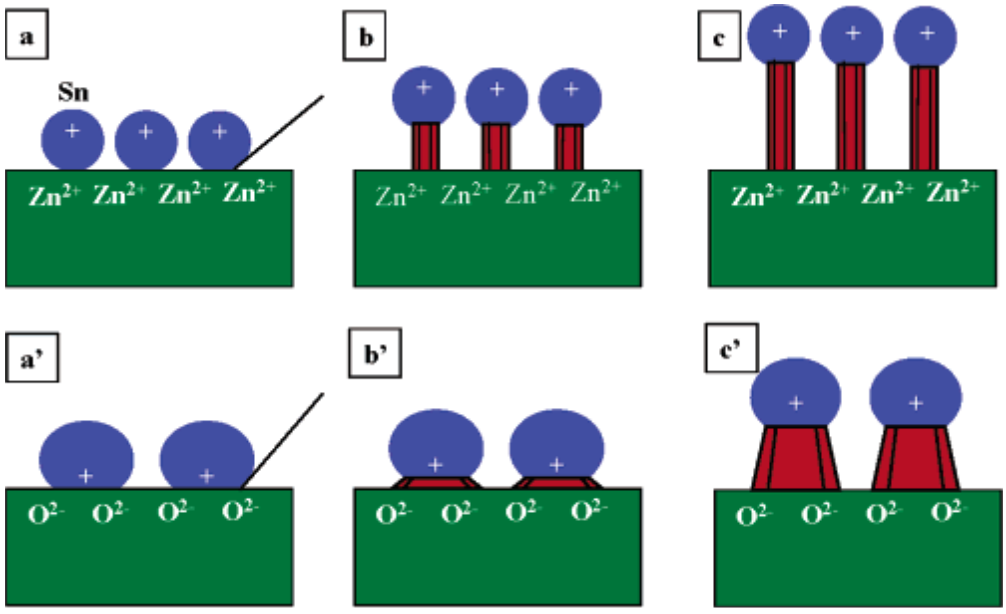

Figure 5.6. Effect of terminal atoms on the VLS crystal growth of ZnO nanowires.

In this chapter, the synthesis of ultrathin ZnO nanowire by self-catalysis is demonstrated. By using the preventing premature oxidation method, a hexagonal cone structured crystal is grown under the low-temperature LPCVD technique. A growth model is proposed to explain the growth of ultrathin ZnO nanowires from the tip of the hexagonal cone. The mechanism is supported by x-ray diffraction (XRD) pattern analysis and scanning electron microscopy (SEM).

5.2. Experimental procedure

The synthesis of ZnO was conducted by LPCVD technique. The reactor was a tube furnace, OTF-1200 from MTI, with 5 inches tube diameter. All the materials for the synthesis including nitrogen gas, oxygen gas, Zn powder, and FTO glass substrate are commercially purchased and no additional purification was performed.

The hexagonal ZO cone was grown under 450˚C environment. About 0.2 g Zn powder as precursor in a bowl-shaped precursor boat was placed in the tube furnace. A gas mixture composed of 100 SCCM nitrogen and 4 SCCM oxygen was introduced into the tube furnace. The furnace was heated up to 450 ˚C for 30 minutes and maintained at this temperature for 2 hours for the reaction. The crystal growth of ultrathin nanowire was conducted in the same condition but higher temperature, 500 ˚C, and the test-tube shaped boat was used. The experimental conditions are listed in Table 5.1. The synthesized ZnO was characterized by Nova NanoSEM 450 under 5 and 10 kV accelerating voltage with ETD and TLD.

Table 5.1. The ZnO synthesis parameters and conditions.

Parameter	Sample 1	Sample 2	Sample 3
Temperature (˚C)	450	450	500
Ramping time (min)	30	30	30
Reaction time (min)	30	120	30
Carrier gas	100 SCCM N_2	100 SCCM N_2	100 SCCM N_2
Oxidizer	4 SCCM O_2	4 SCCM O_2	4 SCCM O_2
Pressure	Low vacuum	Low vacuum	Low vacuum
Precursor	Zn powder	Zn powder	Zn powder
Precursor boat	-	-	Test tube

5.3. Results and discussion

In Figure 5.7, the SEM images taken in different locations within the reaction substrate are displayed. Figure 5.7 (a) are taken near the edge closest to the precursor, and

(b), (c), (d), and (e) are 4 mm away from each other. It is expected that the Zn concentration is decreasing from the closer edge (a) to farthest edge (e). It is observed that the ZnO was grown in hexagonal cone structure in Figure 5.7 (a). This is the result of the thermodynamically preferred reaction mechanism because the product tends to reduce its surface-to-volume ratio to stabilize the structure. This is a reasonable assumption due to the low temperature condition which hinders the kinetically preferred growth. The incomplete growth of the hexagonal cone was found in Figure 5.7 (b), (c) and (d). In Figure 5.7 (e), only the seed particles were found due to the low concentration of Zn. Since the concentration of Zn reactant is lower than at the closest area, the reaction rate was decreased but the reaction proceeded slowly.

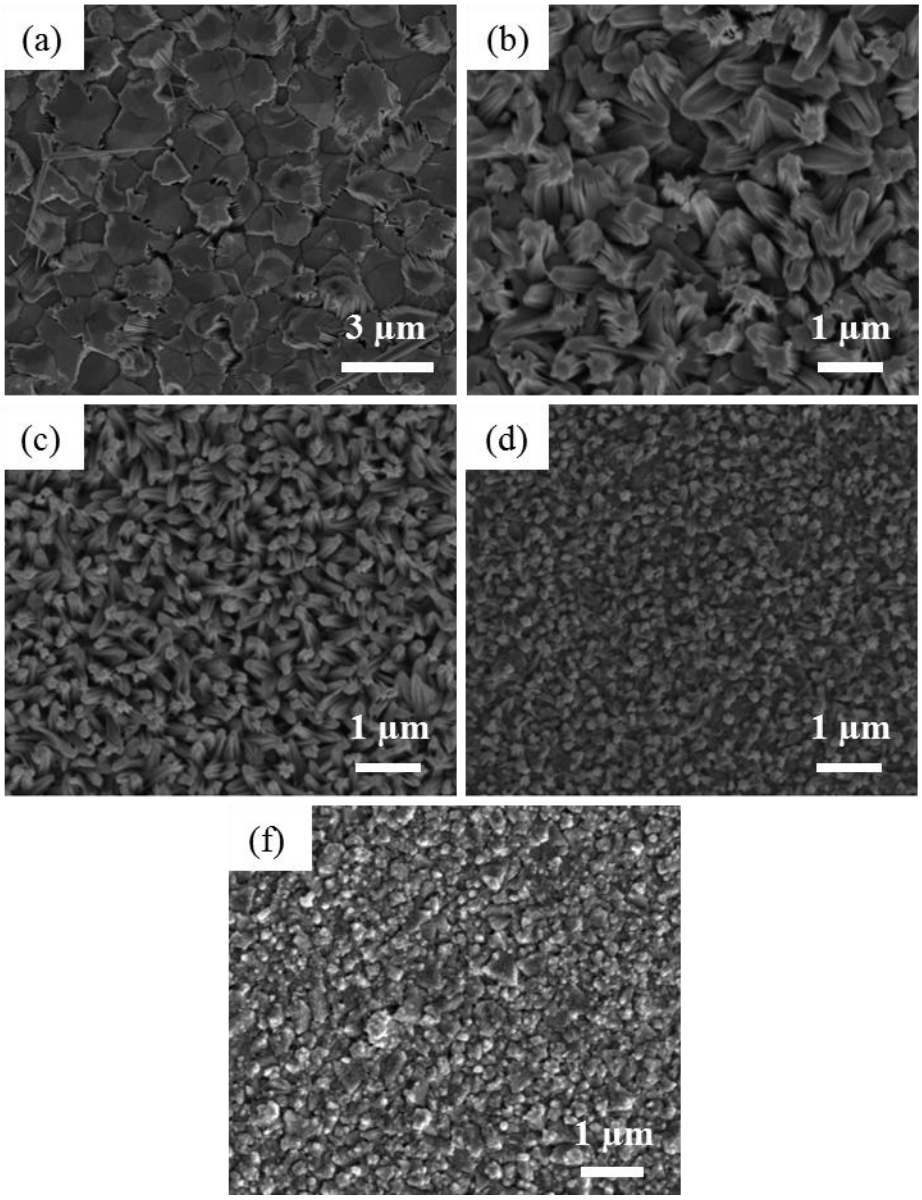

Figure 5.7. SEM images of synthesized ZnO hexagonal cones for 30 minutes at; (a) edge close to the precursor; (b) 4 mm away from the edge; (c) 8 mm away from the edge; (d) 12 mm away from the edge; (e) 16 mm away from the edge.

When enough time is allowed for the reaction, the hexagonal cone is grown as shown in Figure 5.8. In the same manner, Figure 5.8 (a) and (e) are observed at the closest edge and furthest edge, respectively. The hexagonal cones with a pointed tip are observed

in Figure 5.8 (a), but the growth was still proceeding to form the hexagonal cone structure in Figure 5.8 (b). This is the result of vertical growth, horizontal growth in 6 ways, and the filling of voids occurring simultaneously. It should be pointed out that the analogy in Figure 5.8 (e) and 5.7 (b) is originated from the tendency of thermodynamically preferred reactions. That is because the concentration of reactant affects the reaction rate but not the product in the thermodynamically preferred reaction.

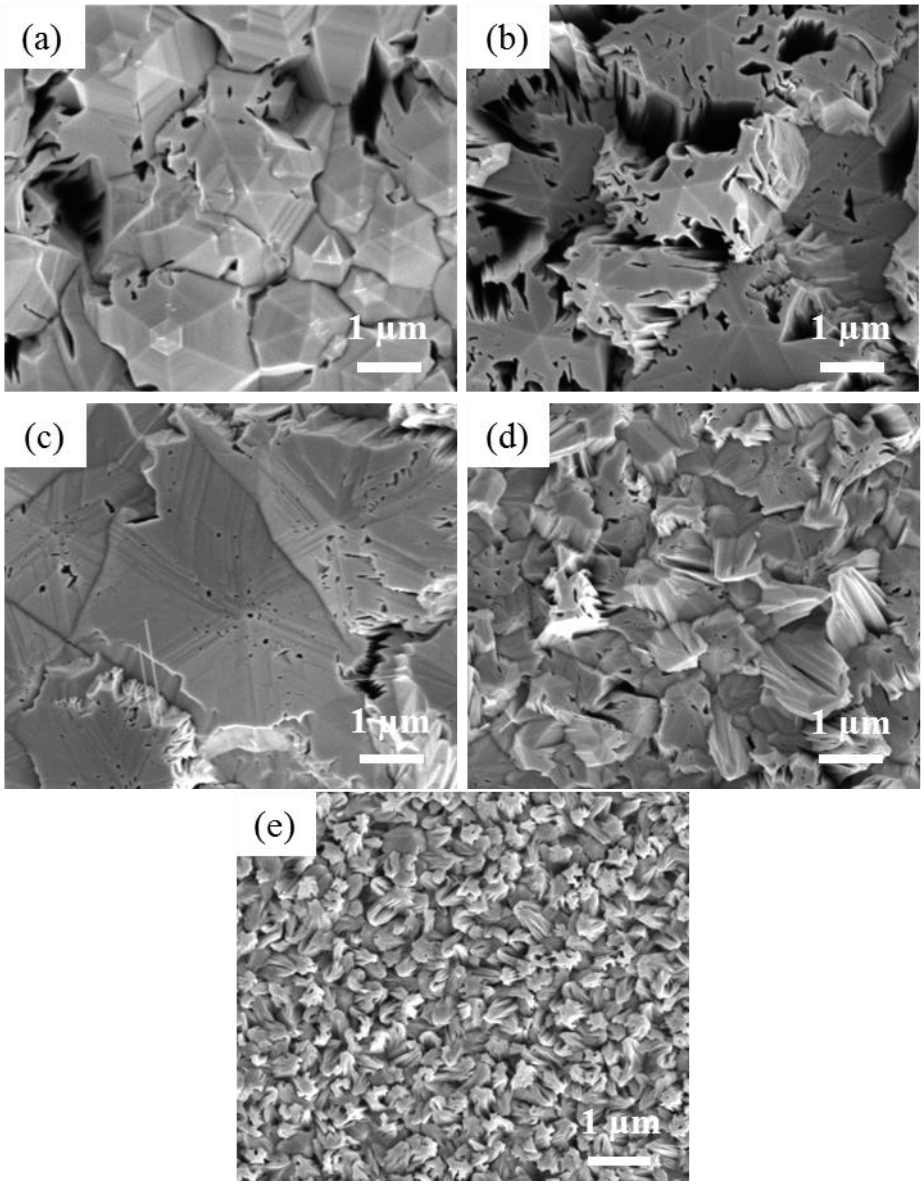

Figure 5.8. SEM images of synthesized ZnO hexagonal cones for 120 minutes at; (a) edge closest to the precursor; (b) 4 mm away from the edge; (c) 8 mm away from the edge; (d) 12 mm away from the edge; (e) 16 mm away from the edge.

To accomplish the growth of ultrathin nanowires, higher temperature and a test tube-shaped precursor boat were required. Stable and continuous supply of Zn reactant and a faster reaction rate could be obtained by these two conditions. Optimized balanced of the

Zn precursor concentration was achieved by adjusting the distance of reaction site from the precursor.

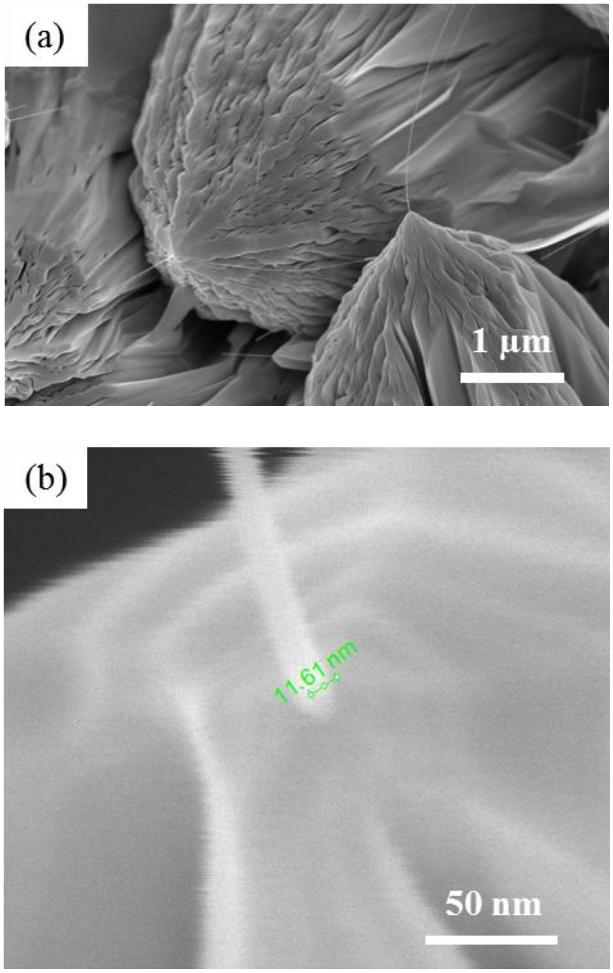

Figure 5.9. SEM images of self-catalyzed ZnO in magnification of; (a) 25,000; (b) 650,000

As shown in Figure 5.9 (a), the ultrathin nanowire was grown from the tip of the hexagonal ZnO cone structured. To measure the diameter of the nanowire, the SEM was observed at 650,000 magnification as shown in Figure 5.9 (b). The SEM image was not too clear to distinguish sharply the border of the nanowire but it could be approximated at about 10 nm.

The reaction mechanism model is suggested as illustrated in Figure 5.10. It is assumed that the tip of the hexagonal cone is terminated by Zn atom, so that the ZnO nanowire was grown in constant diameter due to the Coulomb repulsive force between the Zn atom and Zn droplet. The synthesized ZnO ultrathin nanowire can be used for applications such as quantum laser and solar cells due to the quantum confinement effects due to the extremely small diameter.

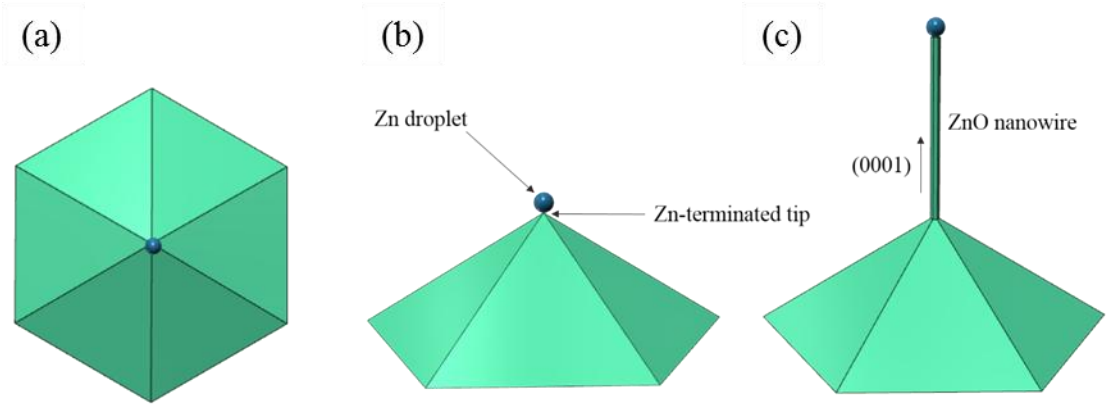

Figure 5.10. Suggested reaction mechanism model; (a) top view of hexagonal cone; (b) Zn droplet placed on the Zn-terminated tip of hexagonal cone; (c) ZnO ultrathin nanowire grown vertically from the tip.

5.4. Conclusion

In conclusion, a novel technique to grow ultrathin ZnO nanowire with diameter of about 10 nm in LPCVD is successfully demonstrated. From the positively charged point of hexagonal cone structure, the ultrathin nanowire was grown by VLS mechanism. Due to its extremely small diameter, potential applications of the synthesized ultrathin nanowire can be the quantum laser cavity and nanoscaled electrical devices.

References

[1] M. Kuno, *Introductory Nanoscience: Physical and chemical concepts*, (Garland Science, Taylor & Francis Group, LLC, 2012)

[2] Y.Q. Fu, J.K. Luo, X.Y. Du, A.J. Flewitt, Y. Li, G.H. Markx, A.J. Walton, and W.I. Milne, *Sensor. Actuat. B-Chem.*, **143**, 606-619 (2010)

[3] Y. W. Heo, L. C. Tien, Y. Kwon, D. P. Norton, S. J. Pearton, B. S. Kang and F. Ren, *Appl. Phys. Lett.*, **85**, 2274-2276 (2004)

[4] S. Bai, W. Wu, Y, Qin, N Cui, D. J. Bayerl, and X. Wang, *Adv. Funct. Mater.*, **21**, 4464-4469 (2011)

[5] Q. H. Li, Y. X. Liang, Q. Wan, and T. H. Wang, *Appl. Phys. Lett.*, **85**, 6389-6391 (2004)

[6] H. M. Chen, C. K. Chen, Y.-C. Chang, C.-W. Tsai, R.-S. Liu, S.-F. Hu, W.-S. Chang, and K.-H. Chen, *Angew. Chem.*, **122**, 6102-6105 (2010)

[7] K. Yum, Z. Wang, A. P. Suryavanshi, and M.-F. Yu, *J. Appl. Phys.*, **96**, 3933-3938 (2004)

[8] M. H. Huang, S. Mao, H. Feick, H. Yan, Y. Wu, H. Kind, E. Weber, R. Russo, P. Yang, *Science*, **292**, 1897-1899 (2001)

[9] Z. P. Wei, Y. M. Lu, D. Z. Shen, Z. Z. Zhang, B. Yao, B. H. Li, J. Y. Zhang, D. X. Zhao, X. W. Fan, and Z. K. Tang, *Appl. Phys. Lett.*, **90**, 042113 (2007)

[10] R. D. Vispute, V. Talyansky, S. Choopun, R. P. Sharma, T. Venkatesan, M. He, X. Tang, J. B. Halpern, M. G. Spencer, Y. X. Li, L. G. Salamanca-Riba, A. A. Iliadis, and K. A. Jones, *Appl. Phys. Lett.*, **73**, 348-350 (1998)

[11] M. Ahmed, and G. Xinxin, *Inorg. Chem. Front.*, **3**, 578-590 (2016)

[12] M. Dvorak, S.-H. Wei, and Z. Wu, *Phys. Rev. Lett.*, **110**, 016402 (2013)

[12] M. Dvorak, S.-H. Wei, and Z. Wu, *Phys. Rev. Lett.*, **110**, 016402 (2013)

[13] Z. L. Wang, *Appl. Phys. A*, **88**, 7-15 (2007)

[14] F. Claeyssens, C. L. Freeman, N. L. Allan, Y. Sun, M. N. R. Ashfold, and J. H. Harding, *J. Mater. Chem.*, **15**, 139-148 (2005)

[15] S. Y. Li, P. Lin, C. Y. Lee, and T. Y. Tseng, *J. Appl. Phys.*, **95**, 3711-3716 (2004)

[16] M. H. Huang, Y. Wu, H. Feick, N. Tran, E. Weber, and P. Yang, *Adv. Mater.*, **13**, 113-116 (2001)

[17] P. X. Gao, and Z. L. Wang, *J. Phys. Chem. B*, **108**, 7534-7537 (2004)

[18] Parish, R. V. *The Metallic Elements*, (Longman Inc., New York, 1977)